Hydrodynamical N-body simulations of galactic coronae in Milky Way-like galaxies

Tesi di Laurea Magistrale

Presentata da:
Filippo Barbani

Relatore:
Dr. Federico Marinacci
Correlatore:
Dr. Raffaele Pascale

Ai miei genitori

Contents

Abstract

Star-forming galaxies like the Milky Way are surrounded by a hot gaseous halo at the virial temperature, the so-called hot corona, that plays a fundamental role in their evolution. On the one hand, this coronal gas is a potential reservoir of fresh, low-metallicity gas that can replenish the disc with new material to sustain the star formation activity over a Hubble time. On the other hand, galactic fountain flows driven by supernova feedback inject high-metallicity gas from the disc to the halo region, causing the cold fountain gas to interact with the hot coronal gas. This interaction has been shown to have a direct impact on efficiency of the cooling and accretion of coronal gas onto the disc with major implications for galaxy evolution. This Thesis project is focused on the study of the gas circulation between the disc and the gaseous halo of star-forming galaxies like the Milky Way. To analyze this circulation and its implications on the properties of the corona and of the disc, we used high-resolution hydrodynamical N-body simulations of a Milky Way-type galaxy with the inclusion of an observationally-motivated hot corona. As a first step, we created suitable galaxy models representative of the Milky Way with a hot gaseous halo in hydrostatic equilibrium. After checking the dynamical equilibrium of such configurations with adiabatic simulations, we evolved the initial conditions thus generated with the *SMUGGLE* model, an explicit ISM and stellar feedback model which is part of the moving-mesh code AREPO. We focused on the interaction between the material ejected from the disc and the galactic corona, analyzing the differences that emerge changing the mass of the latter and studying inflows and outflows of gas and their temperature and metallicity distributions. We have found that gas accreted from the corona is the primary fuel for the star formation, helping in maintaining a constant level of cold gas mass in the disc of the galaxy. The accretion of coronal gas is promoted by its mixing with the galactic fountains. At the disc-corona interface, the corona and the gaseous outflows from the disc mix efficiently, forming regions of gas at intermediate temperatures and metallicities that enhance the cooling of the corona. This mixed gas is then accreted onto the disc diluting its metallicity. The simulations carried out in this Thesis work will enable a step forward toward a realistic modelling of the formation and evolution of Milky Way-type galaxies.

Sommario

Le galassie come la Via Lattea sono circondate da un alone caldo di gas alla temperatura viriale, detto corona, che ha un ruolo cruciale nella loro evoluzione. Da un lato, la corona è una potenziale riserva di gas a bassa metallicità che può rifornire il disco di nuovo materiale in modo da sostenere la formazione stellare per un tempo di Hubble. Dall'altro, le esplosioni di supernova nel disco galattico iniettano parte del gas ad alta metallicità del mezzo interstellare nell'alone, causando l'interazione tra il gas freddo del disco e il gas caldo coronale. È stato dimostrato come questa interazione abbia un impatto diretto sull'efficienza del raffreddamento e sull'accrescimento del gas coronale sul disco, con profonde implicazioni per l'evoluzione generale delle galassie. Questo progetto di tesi si focalizza sullo studio della circolazione del gas tra il disco e l'alone in galassie simili alla Via Lattea. Per analizzare questo fenomeno e le sue implicazioni sulle proprietà della corona e del disco abbiamo utilizzato simulazioni idrodinamiche a N corpi che includono una corona calda attorno alla galassia centrale. Nella prima fase abbiamo creato un modello di galassia che rappresenta la Via Lattea con un alone di gas caldo in equilibrio idrostatico. Dopo aver controllato, tramite simulazioni adiabatiche, la stabilità dinamica di questa configurazione iniziale abbiamo fatto evolvere le condizioni iniziali così generate con il modello *SMUGGLE*, un modello esplicito per il mezzo interstellare e il feedback stellare che è parte del codice a griglia mobile AREPO. Ci siamo concentrati sull'interazione tra il materiale espulso dal disco e la corona galattica, analizzando le differenze che emergono al variare della massa di quest'ultima, studiando le distribuzioni di temperatura e metallicità e i moti di inflow e outflow del gas. Quello che è emerso è che la corona è la principale riserva di materiale per la formazione stellare nel disco. L'accrescimento di gas coronale è promosso dal mescolamento con il gas espulso dal disco dal feedback stellare. In effetti, all'interfaccia tra il disco e la corona, il gas coronale e quello espulso dal disco si mescolano efficientemente formando regioni con gas a temperatura e metallicità intermedie che facilitano il raffreddamento della corona. Questo gas è in seguito accresciuto sul disco diluendone la metallicità. Le simulazioni effettuate in questo lavoro di tesi permetteranno di compiere un passo avanti nella modellizzazione numerica accurata della formazione ed evoluzione delle galassie simili alla Via Lattea.

Introduction 1

The Λ Cold Dark Matter (ΛCDM) model is the most accepted cosmological framework that describes the evolution of our Universe. In the ΛCDM scenario the mass-energy budget of our Universe is composed by dark energy ($\sim 70\%$), matter ($\sim 30\%$) and radiation (that has a negligible contribute to this budget at redshift zero). The matter component is further divided in cold dark matter, $\sim 85\%$ of the matter total content, and baryons (i.e. ordinary matter) making up the remaining $\sim 15\%$. Thanks to their nature, the cold dark matter particles trigger the gravitational collapse at small masses ($\sim 10^4 - 10^5 \ M_\odot$). For this reason, the evolution of the structures in the Universe is hierarchical, meaning that less massive structure are formed earlier and the more massive ones are the result of subsequent mergers. The dark matter density fluctuations grow in time driven by the gravitational interactions, forming the potential wells in which the baryons can cool down and collapse, creating the first generations of stars and, subsequently, the first galaxies.

Galaxies have been classified for the first time by Hubble (1926), with a classification that is still widely used nowadays. In Figure 1.1 we show a schematic representation of the so-called *Hubble tuning fork* diagram.
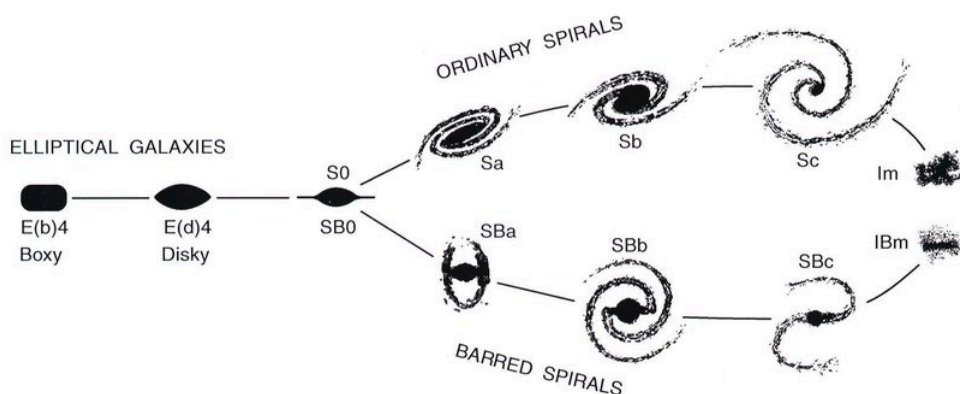

Figure 1.1: Schematic representation of the Hubble tuning fork. From left to right we see elliptical galaxies (Eb or Ed), lenticular galaxy (S0 or SB0), spiral galaxies (S or SB) and irregular galaxies (Im or IBm). Figure taken from Kormendy and Bender (1996).

In general, galaxies can be divided in two broad categories:

(i) **Early-type galaxies**, that include elliptical and lenticular galaxies. Elliptical galaxies are the most massive galaxies ($\sim 10^{10} - 10^{13}$ M$_\odot$[1]; Cimatti, Fraternali and Nipoti 2019) in the present-day Universe. They have in general a population of very old stars (age $\gg 1$ Gyr; De Jong and Davies 1997) and no star formation, for this reason they are also called *quiescent* or *passive* galaxies. The gas in these galaxies is for the most part ($\sim 10^9 - 10^{11}$ M$_\odot$) hot ($T \sim 10^7$ K) and at high-metallicity[2] ($Z > 0.5 \ Z_\odot$); in some cases, traces of dust, neutral and cold gas and star formation are found, probably due to past interactions with gas-rich galaxies (e.g. Morganti et al. 2006). Lenticular galaxies are halfway between elliptical and spiral galaxies, having the same properties of the former, but presenting also a disc with little or no star formation. They are interpreted as spiral galaxies which have lost the reservoir of gas, quenching their star formation (e.g. Spitzer Jr and Baade, 1951).

(ii) **Late-type galaxies** include spiral and irregular galaxies. These objects are also called *star-forming galaxies* because they present an ongoing, non-negligible level of star formation. Spiral galaxies have a more complex structure than elliptical galaxies, they are in general gas-rich galaxies, presenting a complex and multi-phase interstellar medium (ISM), with cold, warm and hot gas coexisting in the same environment. Irregular galaxies have in general smaller masses and an irregular shape without the presence of a disc.

In recent years, thanks to the advent of large field surveys (e.g. the Sloan Digital Sky Survey, York et al. 2000) which made possible the observation of millions of galaxies, also a bimodality (e.g. Baldry et al. 2006) in galaxy colors as a function of stellar mass has emerged. In Figure 1.2 we show a $u - r$ color[3]-stellar mass diagram taken from Schawinski et al. (2014): in the top left panel all the galaxies of the sample are present, and we can note the presence of two regions of interest: the so-called *red sequence*, a clear correlation between the colour and the mass of the galaxy towards redder colours, and the so-called *blue cloud*, a distribution centrally peaked in the bluer region of the diagram. Isolating only a type of galaxy shows

---

[1]In galaxy clusters, the elliptical galaxies at the center of the cluster can be even more massive than 10^{13} M$_\odot$.

[2]The metallicity quantifies the abundance of metals, i.e. elements heavier than helium, in the gas.

[3]The filter u is sensitive to the ultraviolet light, i.e. to the lights of young and massive stars present in the case of an active star formation. The filter r is more sensible to the red light of old stars.
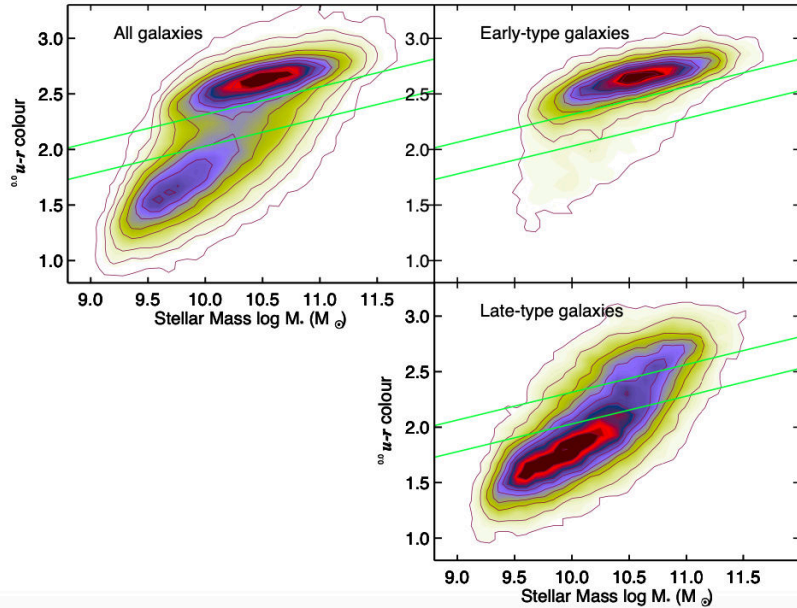
Figure 1.2: $u - r$ color-stellar mass diagram of a sample of galaxies taken from the Sloan Digital Sky Survey. The left panel shows all the galaxies in the sample, the top right panel only the early-type galaxies, while the bottom right only the late-type galaxies. Figure taken from Schawinski et al. (2014).

that early-type galaxies (top right panel) populate almost only the red sequence, they are in fact dominated by old stellar populations, whereas late-type galaxies (bottom right panel) mostly reside in the blue cloud, feature explained by their ongoing star formation. The panels in Figure 1.1 shows the existence of two distinct populations of galaxies with different physical properties and evolution. It has been suggested that galaxies tend to evolve from the blue cloud to the red sequence but not vice versa (Peng et al., 2010), this type of evolutionary track is described later in this Chapter in Section 1.1.3. In this Thesis work we focus on star-forming galaxies and in particular on the gas present in their surrounding environment, on its connection with the disc of such galaxies and on the importance of this interaction for the formation of new stars.

1.1 Galaxy interactions with their surrounding environment

Galaxies are not isolated systems, in fact they interact with their surrounding environment in various ways. For instance, they can interact with other galaxies through high-speed encounters (Moore et al., 1996), mergers (Conselice et al., 2003) or, in

more dense environments, ram pressure stripping (Abadi et al., 1999) and cannibalism (Hausman and Ostriker, 1978). These interactions between galaxies and their environment are extremely important because have a direct influence in the way galaxies evolve. For the investigation carried out in this work, we concentrate on the interactions only with the external medium, without considering possible interactions with other galaxies. The interaction between galaxies and their environment is mediated by **outflows** and **inflows** of gas (left-hand panel in Figure 1.3). Star-forming galaxies can eject gas outflows from the disc through stellar feedback, a set of processes that release energy and momentum in the ISM, changing its thermal and dynamical state; these processes include stellar winds, stellar radiation and supernovae explosions. In particular, multiple supernovae explosions can produce superbubbles (Mac Low and McCray, 1988), giant bubbles filled with hot gas that can exceed the height of the disc, ejecting material out of it. If this material has a velocity that is smaller than the escape velocity from the galaxy, it will fall back onto the disc (generally at a different location) giving rise to a gas circulation and creating the so-called galactic fountains.
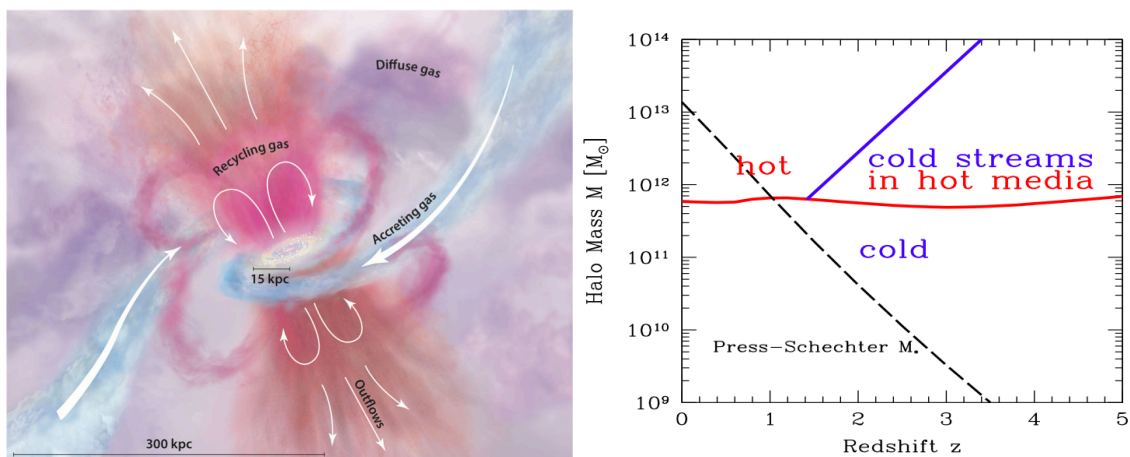

Figure 1.3: *Left*: Schematic representation of the interaction between the disc of a spiral galaxy and the external environment. The gas can be expelled from the galaxy through outflows, in particular galactic fountains, or enter through inflows from the intergalactic medium (IGM) or from the hot coronal gas present around the disc. Figure taken from Tumlinson et al. (2017). *Right*: Critical halo mass as a function of the redshift. The red line separates a pure cold accretion mode from a hot/hot and cold accretion mode (separated from the blue line). Figure taken from Dekel et al. (2013).

Gas can also be accreted from the surrounding medium and this occurs generally in two distinct ways. In the **hot accretion mode** the gas falling into the potential

well of the dark matter halo is shock heated to its virial temperature when it reaches the center (Rees and Ostriker, 1977; White and Rees, 1978; Silk, 1977), while in the **cold accretion mode** the gas can reach the center of the halo still in a cold form (Kereš et al., 2005) because the post-shock cooling time becomes shorter then the dynamical time and the gas is not heated efficiently. This dual nature of gas accretion has been investigated with numerical simulations over the past years (e.g. Birnboim and Dekel 2003). In Figure 1.3 (right-hand panel) we show a diagram (Dekel et al., 2013) that explains both these phenomena, based on analytic spherically-symmetric calculations.

In practice, the panel shows the presence of a critical halo mass ($M_{cr} \sim 10^{12}$ $M_\odot$) under which the halo cannot efficiently shock heat the gas that falls in it, allowing cold gas to penetrate and accrete onto the disc of the galaxy. Below this critical mass, this occurs independently of redshift. On the other hand, halos with $M_h > M_{cr}$ are effective at shock heating the gas, in this case for redshifts $z < 2$ the hot accretion mode is dominant. For $z > 2$ the gas is still heated to the virial temperature, but the accretion occurs predominantly through gas filaments from the intergalactic medium that can reach the galaxy without being disrupted thanks to their high density (Ocvirk et al., 2008). Therefore, galaxies change the predominant mode of accretion over time: high redshift star-forming galaxies will have a mass $M_h < M_{cr}$ and will be accreting gas predominantly via the cold mode. However, galaxies tend to increase their mass over time and some will eventually exceed the critical mass, accreting gas at the virial temperature and forming a gas reservoir (the so-called hot corona) around them. A Milky Way-like galaxy ($M_h \sim 10^{12}$ $M_\odot$) typically reaches M_{cr} at $z \sim 1 - 2$ (Kereš et al., 2009), therefore it will form a hot gaseous halo at around that time, but more massive galaxies tend to form the corona at higher redshifts.

1.1.1 Indirect evidence of gas accretion

Gas accretion is difficult to observe, in fact observations cannot accurately distinguish between inflows, outflows or other types of motion. However, in the past years many indirect pieces of evidence of gas accretion and of the presence of gas around star-forming galaxies have been found (see Almeida et al. 2014, Fraternali 2013 and Fraternali 2017 for detailed reviews). Such pieces of indirect evidence of gas accretion can be summarized by the following points.

- *Depletion time*: galaxies like the Milky-Way have formed stars with an almost constant star formation rate for about their entire life (Twarog, 1980; Cignoni et al.,

2006), however the gas present inside these galaxies is not sufficient to sustain star formation rate levels of ~ 1 M$_\odot$ yr^{-1} for more than ~ 1 Gyr. Therefore, inflows of gas are necessary to prevent the quenching of star formation.

- *Missing baryon problem*: another indirect evidence of the necessity of low density gas around galaxies is the so-called missing baryon problem. The mean baryon density, measured in the low-redshift Universe (Fukugita et al., 1998; Nicastro et al., 2005), accounts only for a small fraction of the baryon density obtained from cosmological observations, e.g. the Planck Collaboration (Aghanim et al., 2020) obtained from the angular spectrum of the CMB a baryon density $\Omega_b h^2 = 0.0224 \pm 0.0001$. What have been observed is that $\sim 10\%$ of the baryons resides in stars, interstellar medium and intracluster medium. The rest of the baryons is thought to reside in the cold and hot intergalactic medium inside cosmic filaments ($\sim 50\%$; Penton et al. 2004; Nicastro et al. 2018) and surrounding galaxies ($\sim 40\%$). Moreover, baryons inside galaxies in the form of cool gas and stars are much less than expected (e.g. Papastergis et al. 2012), with baryon fraction that are much smaller than the universal one ($f_b \sim 0.16$). For these reasons we expect hot gas difficult to observe to reside around galaxies, accounting for a fraction of these missing baryons.

- *G-dwarf problem*: the necessity of gas accretion comes also from the G-dwarf problem (Van den Bergh, 1962), that is a deficit of metal-poor stars in the solar neighbourhood: $\sim 20\%$ of the stars have a metallicity $< 1/4$ solar, with respect to the 40% expected in the case of a closed-box evolution (i.e. evolution of the galaxy in isolation with no interaction with its environment). This suggests the presence of an evolutionary track for star-forming galaxies very different from total isolation. The preferred solution to this problem is to require a continuous accretion of low metallicity gas (~ 0.1 $Z_\odot$, Tosi 1988) that fuels star formation (Chiappini et al., 2001). The G-dwarf problem is also present in galaxies other than the Milky Way (Worthey et al., 1996), confirming the fundamental nature of the metal-poor accretion phenomena. Also, the abundance of observed deuterium in the local ISM becomes consistent with the one expected from the cosmological nucleosynthesis only if we account for this accretion of low-metallicity gas (Steigman, 2007).

- *Mass-metallicity relation*: a universal scaling law of galaxies is the mass-metallicity relation (Skillman et al., 1989; Tremonti et al., 2004), for which more massive galaxies have a higher metallicity. This happens because massive galaxies have a deeper potential well in which gas can more efficiently accrete, and form stars more effectively and for a longer time with respect to lower mass galaxies. Moreover, the large mass can help the retention of gas: the gas ejected from winds and SNe will

hardly escape from the galaxy, preventing the quenching of the star formation. It has been shown that the wide scatter present in the relation, for which galaxies with the same mass can have different metallicities, is associated with the SFR of the galaxy (Mannucci et al., 2010; Lara-López et al., 2010): higher present SFR gives a lower metallicity. This can be explained if the formation of stars is sustained by metal-poor gas inflows, which decrease the metallicity of the ISM and increases the SFR.
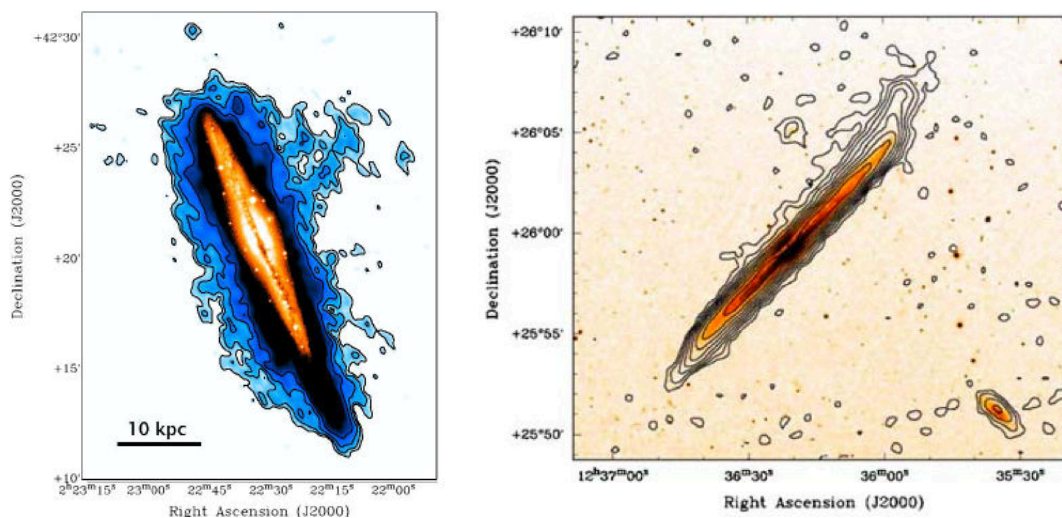
1.1.2 Observations of extraplanar gas

Figure 1.4: *Left*: H I map (blue) of NGC 891 superimposed on an optical image (orange), the cold gas extends up to ~ 8 kpc above and below the disc. Figure taken from Oosterloo et al. (2007). *Right*: H I map of NGC 4565 superimposed on the optical image. Figure taken from Sancisi et al. (2008).

We now focus on the observations of the gas that surrounds the disc of the galaxy, also known as the circumgalactic medium (CGM). For its fundamental nature in supplying the galaxy with fresh gas eligible for star formation, extraplanar gas, i.e. gas present outside the disc of the galaxy, around star-forming galaxies has been widely observed in the last years. Cold ($T < 10^4$ K) neutral gas can be tracked observing the neutral hydrogen H I with the 21 cm line. The Milky Way (Lockman, 2002) and nearby spiral galaxies (Fraternali et al., 2002; Matthews and Wood, 2003; Zschaechner et al., 2015), like NGC 891 (Oosterloo et al., 2007) or NGC 4565 (Sancisi

et al., 2008) (Figure 1.4), show the presence of neutral gas that extends for few kpc over the plane of the disc. In our Galaxy the existence of clouds of gas surrounding the disc has been known for a long time, these are the so-called High Velocity Clouds (HVCs).

HVCs can have an external (i.e. accreted from the environment) or internal (i.e. coming from galactic fountains ejected from the disc; Fraternali et al. 2015) origin. Putman et al. (2012) estimated a mass of cold gas around the Milky Way, traced by HVCs (excluding the contribution from the Large Magellanic stream), of 2.6×10^7 M$_\odot$. The inflow rate of the HVCs is $\sim 0.1 - 0.2$ M$_\odot$ yr^{-1}, too small to sustain the star formation (SFR $\sim 1 - 2$ M$_\odot$ yr^{-1}), therefore they cannot be powering star formation in the Galaxy. Furthermore, ionized gas ($10^4 < T < 10^6$ K) is also observed around the discs of spiral galaxies: this is usually done observing absorption lines in distant background bright sources like quasars around the Milky Way (Richter et al., 2013) and around other galaxies (Werk et al., 2014). Lehner and Howk (2011) found a mass $\sim 10^8$ M$_\odot$ and an hypothetical inflow rate of $\sim 0.8 - 1.4$ M$_\odot$ yr^{-1} that could be able to fuel the star formation in our galaxy.

Observations of galactic coronae

As already mentioned, in halos more massive than $\sim 10^{12}$ M$_\odot$ we expect the formation of a corona of hot gas around the galaxy, in this component must reside a significant fraction of the gas mass associated to a star-forming galaxy. These massive halos have a virial temperature higher than 0.1 keV and therefore the hot gas is expected to thermally emit X-ray photons through bremsstrahlung emission. In the past years many observations have been attempted to find and study the properties of these hot coronae around spiral galaxies, but due to their temperature range and the low-densities a large fraction of the thermal emission falls under the Galactic absorption threshold (0.2-0.3 keV) making this component very faint and highly contaminated by the X-ray background. For these reasons, these observations have been unsuccessful for years (Li et al., 2008; Rasmussen et al., 2009; Li et al., 2011; Bogdán et al., 2015).

Observations around four massive ($\sim 10^{13}$ M$_\odot$) spiral galaxies (i.e. NGC 1961, UGC 12591, NGC 266 and NGC 6753; taken with *Chandra*, *XMM-Newton* and *ROSAT*), finally succeded in finding a visible X-ray emission of the corona. In NGC 1961 Anderson and Bregman (2011) estimated a total hot gas mass of $1 - 3 \times 10^{11}$ M$_\odot$ assuming a metallicity of 0.5 Z$_\odot$, but a precise measurement of the metallicity is extremely important to constraint the real mass of the corona. In UGC 12591 Dai

et al. (2012) detected an emission within 80 kpc finding an upper limit of 4.5×10^{11} $M_\odot$ for the corona mass and a temperature $\sim 7.42 \times 10^6$ K. In NGC 266 Bogdán et al. (2013) found a mass very similar to NGC 1961 and UGC 12591, these galaxies have a very similar virial mass, suggesting similar physical properties in the coronae of these massive spiral galaxies.
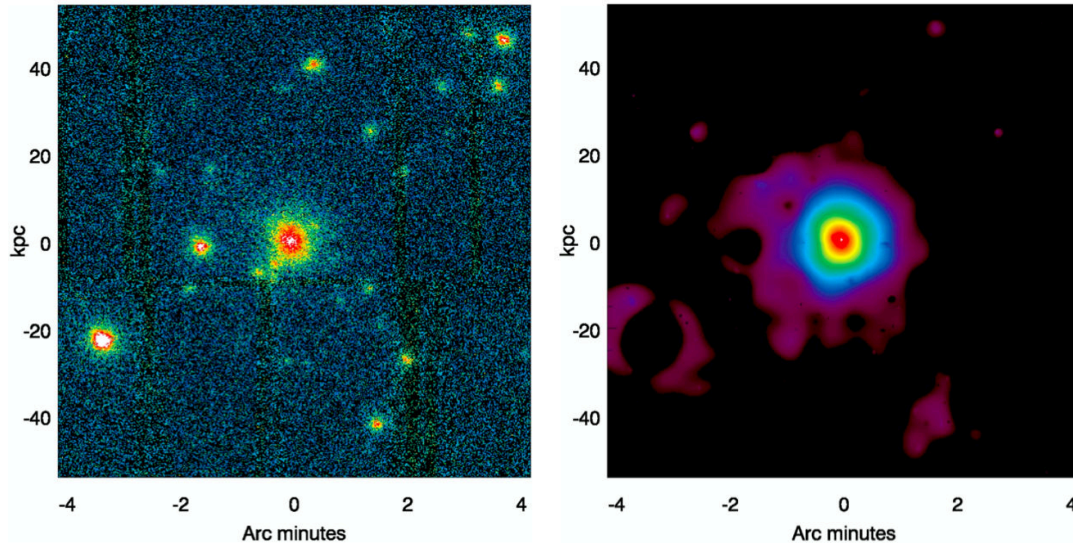

Figure 1.5: *Left*: *XMM-Newton* image of NGC 6753 in the 0.3-2.5 keV band. The image was created combining the datas from the three instruments of the telescope: the PN and the two MOS cameras. We can note the presence of the corona and of many point-like X-ray sources (active galactic nuclei (AGN) or X-ray binaries). *Right*: Same image but de-noised. This shows the X-ray diffuse emission of the galaxy up to ~ 25 kpc from the center of the galaxy. Figures taken from Bogdán et al. (2017).

Bogdán et al. (2017) observed NGC 6753 with deeper observations, finding a temperature that decreases from $\sim 8.12 \times 10^6$ K in the center to $\sim 4.64 \times 10^6$ K at 50 kpc. They also found a uniform metallicity ~ 0.1 $Z_\odot$, which is about one order of magnitude smaller than the one observed in elliptical galaxies, suggesting a formation through an accretion of gas rather than an internal origin. This observation is shown in Figure 1.5, where is apparent the presence of a symmetric diffuse X-ray emission around the galaxy.

Despite the physical properties that make very difficult its direct detection, many attempts to determine the density of the Milky Way corona have been carried out. A possible approach to estimate the density of the corona is to investigate the process of ram-pressure stripping of dwarf spheroidal galaxies inside the Milky Way halo (Grcevich and Putman, 2009; Gatto et al., 2013; Salem et al., 2015; Marty-

nenko, 2021). These dwarf galaxies have very small masses of gas that have been hypothetically stripped away along their trajectories inside the Milky Way corona. Combining simulations of satellites orbiting around the Milky Way (including the presence of ram-pressure) with observations, an estimate of the coronal density can be found without assumptions on the gas metallicity. Also, observations of the dispersion measure of pulsars can be used (Anderson and Bregman, 2010): the dispersion measure yields the electron density integrated along the line-of-sight between the observer and the pulsar and it can be found measuring the delay in the periodic pulsar emission observed at two different frequencies. Furthermore, another observational approach used to find the coronal density lies in observations of absorption lines (mainly OVII and OVIII lines) at zero redshift in the spectra of distant objects (Yao et al., 2012; Gupta et al., 2012; Miller and Bregman, 2013; Kaaret et al., 2020). However, in this case it is necessary to make an assumption on the gas metallicity (that is still uncertain) and this gives less robust results. Results from ram-pressure stripping and from X-ray spectra have a wide discrepancy, Troitsky (2017) found that this can be reduced assuming a metallicity profile, with a large decrease of Z in the outer parts of the corona. The typical values for the Milky Way corona found by these observations, as order of magnitude, are: an electron number density $\langle n_e \rangle \sim 10^{-5}$ cm^{-3} (averaged over a distance of 250 kpc radius), an average temperature of $T \sim 10^6$ K and metallicities $Z \sim 0.1 - 0.7$ Z$_\odot$.

1.1.3 Cooling of the corona: theoretical and numerical results

We have understood that both theory (e.g. White and Rees 1978; Fukugita and Peebles 2006) and (direct and indirect) observations go in the direction of the presence of a hot metal-poor gas reservoir, the galactic corona, around galaxies. Galactic coronae in elliptical and spiral galaxies are expected to have very different physical properties. The early-type galaxy coronae have a metallicity that is very close to $Z_\odot$ (Ji et al., 2009), suggesting a large contribution from material ejected from evolved stars via stellar feedback (Ciotti and Ostriker, 1997). These galaxies do not have or have only small amount of cold gas and star formation, suggesting an inefficiency in the cooling of the corona: cooling can happen in the center of the galaxy where the densities are the highest, but the generated cold gas is accreted onto the super-massive black hole, fueling AGN feedback, that re-heats the corona. In spiral galaxies a totally different scenario emerges, with a low-metallicity corona and comparatively large cooling times (of a few Gyr near the disc). Here, we expect the presence of an efficient mechanism that cools the corona and accretes it onto
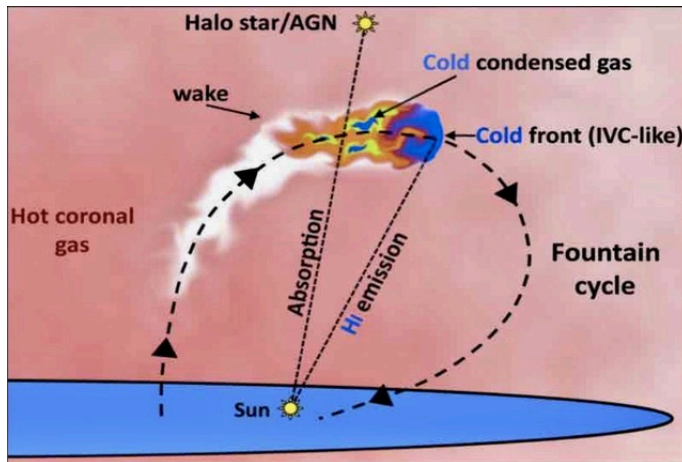
Figure 1.6: Cartoon sketch of a galactic fountain. The cold gas is ejected from the disc and travels through the hot corona generating a wake in which the coronal gas can condensate. Figure taken from Fraternali (2013).

the disc of the galaxy. The mechanism that cools the coronal gas must be efficient in spiral galaxies and not in early type galaxies since the cooling seems to happen only in the presence of a cold disc of gas. A possible mechanism that could be triggered is represented by the interaction between the cold high-metallicity gas ejected from the disc and the metal-poor hot corona. As mentioned, star-forming galaxies can eject gas in the form of galactic fountains or galactic winds (Oppenheimer et al., 2010); if this gas efficiently mixes with the corona it can decrease its cooling time forming an intermediate temperature and metallicity gas. As the cloud of gas ejected from the disc travels through the hot corona there is the development of a Kelvin-Helmoltz instability[4], that helps the mixing of the gas, and the formation of a wake of gas behind it. In the wake some of the coronal gas can condensate thanks to its reduced cooling time, increasing the mass of the cold gas that then rains down on the disc, supplying it with fresh fuel for star formation (see Figure 1.6). This phenomena has been studied with very high resolution (on parsec-scale) simulations of the interface region between the corona and the cold gas clouds (Marinacci et al., 2010, 2011). In this way the nature of the interaction is captured but not inserted in a realistic galaxy model. It has been found that a higher temperature of the corona reduces the ability of its condensation onto the galactic fountains, meaning that more massive galaxies (that have a higher virial temperature) will be less efficient in accreting gas from the external environment, bringing to a quenching of the star formation (Armillotta et al., 2016). Therefore, reaching high galaxy masses ($\sim 10^{13}$ $M_\odot$)

---

[4]The Kelvin-Helmoltz instability is a hydrodynamical instability that occurs when two different fluids are in relative shearing motion.

blocks the gas inflows that sustain the formation of new stars, this could be one of the channel with which star-forming galaxies evolve, passing from the blue cloud to the red sequence (Figure 1.2).

Besides the high-resolution pc-scale simulations just described, other types of simulations have been performed in the last years, such as zoom-in simulations, in which also the cosmological framework is captured still being able to reach good resolutions in the regions where the galaxies reside (e.g. Hafen et al. 2019; Anglés-Alcázar et al. 2017; Suresh et al. 2015; Grand et al. 2019). For instance, Suresh et al. (2015) studied the effects of the galactic feedback implementation on the CGM, finding that different CGM behaviours can emerge from different choices of the stellar feedback implementation. Hence, developing a realistic stellar feedback model is fundamental to capture the essence of the physical interaction between the disc and the corona.

1.2 This Thesis

This Master Thesis project is focused on the study of the gas circulation between the disc and the corona of star-forming galaxies like the Milky Way. To analyze this circulation and its implications on the properties of the corona and of the gas that is subsequently accreted onto the disc, we made use of high-resolution ($\sim 10^4$ $M_\odot$) hydrodynamical N-body simulations of a Milky Way-like galaxy, with the inclusion of an observationally-motivated hot corona around the galaxy. After sampling the galaxy initial conditions, the simulations were evolved with the *SMUGGLE* model, an explicit ISM and stellar feedback model that is part of the moving-mesh code AREPO. So far, the *SMUGGLE* model has been tested on isolated galaxies in the absence of a hot corona, which was a missing ingredient in the previous generation of hydrodynamical N-body simulations. The calculations that we will carry out in this Thesis work will be the first that include such an important component for galactic evolution in this framework. This will enable us to make an important step forward towards a more physically faithful modelling of the evolution of star-forming galaxies. The Thesis is organised as follows:

- In **Chapter 2** we describe the numerical methods used in this Thesis work. In particular, first we describe in general the numerical methods more used in astrophysics for solving the equations of hydrodynamics and gravity, we then describe in more detail the moving-mesh code AREPO and the *SMUGGLE* model.

- In **Chapter 3** we describe the initial conditions for the isolated Milky Way-type galaxy. First, we describe the assignment of the structural and kinematics properties of the different galaxy components. After that, we illustrate the numerical implementation of the initial conditions. Finally, we test them creating plots of the main quantities and comparing them with the analytic expectations and the observations.

- In **Chapter 4** we present the results obtained from the simulations. In particular, in Section 4.1 we show the results of the performed adiabatic simulations, i.e. simulations with only the presence of hydrodynamics and gravity. This has been done to test the equilibrium of the different components of the galaxy in the initial conditions. In Section 4.2 we show the results obtained from the simulations carried out using the *SMUGGLE* model. We studied the connection between the star formation and the outflows and inflows of gas (Subsection 4.2.1) and the disc-corona interface (Subsection 4.2.2), focusing on the differences that emerge changing the mass of the corona.

- In **Chapter 5** we summarize the main results obtained in this Thesis work and we describe its future perspectives.

Numerical methods

2

The majority of astrophysical phenomena are non-linear and it is usually not possible to determine an analytical solution to the equations that describe their evolution. Therefore,to model and understand the different processes that govern fluid and N-body dynamics, the use of numerical simulations is necessary. We therefore describe the numerical methods used to solve the equations of hydrodynamics (Section 2.1) and the Poisson equation (Section 2.2) in modern astrophysical simulations (see Vogelsberger et al. 2020 for a more detailed review on the methods used in particular for galaxy formation simulations) and in particular the one used in this work. In Section 2.3 we describe the code AREPO, used to perform the simulations analysed in this Thesis. Finally, in Section 2.4 we describe the *SMUGGLE* model, an explicit ISM and stellar feedback model, that has been used in this work.

2.1 Numerical methods for hydrodynamics

Baryons represent $\sim 5\%$ of the matter-energy budget of the Universe, and can be divided into stars ($\sim 7\%$) and gas ($\sim 93\%$). Despite the small contribution to the total mass of the Universe, at small scales hydrodynamics is fundamental, as it is the driver of many important phenomena, such as star formation, AGN feedback, stellar feedback, turbulence, shock waves, cooling flows and many others. All these phenomena contributes in shaping the evolution of astrophysical objects on many scales, from stars to clusters of galaxies. In particular, the physics of the gas have a major role in the formation and evolution of galaxies, as described in Chapter 1. Therefore, studying the gaseous phase is fundamental to correctly understand the majority of these astrophysical processes.

If we consider an inviscid fluid, neglecting the presence of magnetic fields, its dynamics is governed by the Euler equations, a set of hyperbolic, non-linear partial differential equations

$$
\begin{cases}
\dfrac{\partial \rho}{\partial t} + \nabla \cdot (\rho \boldsymbol{v}) = 0 \\[2ex]
\dfrac{\partial (\rho \boldsymbol{v})}{\partial t} + \nabla \cdot (\rho \boldsymbol{v} \otimes \mathbf{v} + P \mathbb{1}) = 0 \\[2ex]
\dfrac{\partial E}{\partial t} + \nabla \cdot (E + P) \boldsymbol{v} = 0
\end{cases}
\qquad . \qquad (2.1.1)
$$

where ρ is the density, $\boldsymbol{v}$ is the velocity, P is the pressure, E is the total energy density of the fluid and $\mathbb{1}$ is the identity matrix. Equations (2.1.1) represent, from top to bottom, the conservation of mass, momentum and energy of the fluid. The total energy density is defined as

$$
E = \frac{\rho \boldsymbol{v}^2}{2} + \frac{P}{\gamma - 1}. \qquad (2.1.2)
$$

Also, to close and solve the system we need another equation, that is an equation of state relating gas pressure, density and internal energy. Such equation for an ideal fluid (the case that we treat in this Thesis work) reads

$$
P = (\gamma - 1)\rho e, \qquad (2.1.3)
$$

where γ is the adiabatic index and e is the internal energy per unit mass. In order to solve the hydrodynamics equations (2.1.1), two families of methods are widely used, Eulerian and Lagrangian methods. Both types of methods have advantages and disadvantages and they will be briefly outlined below.

2.1.1 Eulerian codes

In an **Eulerian code** the simulated volume is discretized on a mesh (that is formed by cells) and the evolution of the fluid is obtained studying the variables that define the state of the fluid, in particular the primitive $\mathbf{W} = (\rho, P, \mathbf{v})$ or the conservative $\mathbf{Q} = (m, \mathbf{p}, E)$ variables ($\mathbf{p}$ is the momentum of the fluid), inside the grid cell volumes. Between the cell interfaces there are exchanges of mass, momentum and energy. Therefore, with this method we are focused on given volumes in space and we observe how the properties of the fluid vary over the time. There are different types of Eulerian methods, for instance *finite differences methods* (e.g. Ryu and Jones 1995, Ryu et al. 1995), in which it is studied how the variables evolve at the center of the cells, and the *finite volume methods* (e.g. Zachary and Colella

1992, Dai and Woodward 1994, Janhunen 2000, Ziegler 2004, Balsara 2004) where volume-averaged quantities are used. Nowadays, finite-volume Godunov methods (Godunov, 1959) are widely adopted. In such methods (see Section 2.3.3), the fluxes across cell interfaces are computed by solving a set of Riemann problems at these interfaces and the variables are updated consequently with a conservative scheme. If we consider constant values for the variables inside the cells, the method has a first-order accuracy; to reach the second-order it is possible to use extrapolation methods. One disadvantage of Eulerian methods is that the resolution has to be modified explicitly in different zones of the simulation in order to resolve phenomena that occur on different spatial scales.

2.1.2 Lagrangian codes

In a **Lagrangian code** the motion of individual fluid elements is followed and the variation of their properties over time is analysed (in this case there is no volume discretization). The more used methods are the so-called *Smoothed Particles Hydrodynamics* (SPH) techniques (Lucy, 1977; Gingold and Monaghan, 1977; Springel, 2010*b*), which use particles to sample the fluid elements. In this way the resolution is always automatically adapted to the flow. This is extremely attractive in some applications that need to model a large dynamic range of spatial scales, such as cosmological simulations, and the resolution does not need to be explicitly adjusted in different regions of the simulation. The main disadvantage of these types of codes is their inability in accurately representing discontinuities, which are very common in astrophysical problems, for instance shock waves or contact instabilities.

2.1.3 Arbitrary Lagrangian-Eulerian codes

Another approach that combines both Eulerian and Lagrangian codes, thus mitigating their shortcomings, is possible. In this case, the volume is discretized but the cells are allowed to move with the fluid. The numerical methods using this approach are called **Arbitrary Lagrangian-Eulerian** (ALE) methods. These methods are particularly important as they are becoming commonly used in galaxy evolution simulations nowadays for their flexibility. This family of methods had a great development in recent years with the creation of new ALE codes (Duffell and MacFadyen, 2011; Vandenbroucke and De Rijcke, 2016; Hopkins, 2015). These also include the AREPO code (see Section 2.3), which has been used in this Thesis work.

2.2 Numerical methods for gravity

Gravity is the driving force of many astrophysical phenomena that shape the evolution of the Universe, for instance it is responsible for instability processes that lead to the formation of cosmic structures. In order to determine the evolution of complex systems like galaxies it is necessary to compute the evolution of a set of N collision-less (or collisional in the case of gas particles) particles evolving under their own self-gravity (the so-called N-body problem), these particles interact with each other, feel a given gravitational acceleration and move according to it. The only way to address in full detail the N-body problem (if $N > 2$) is to use numerical methods. The problem that we want to face is to find the acceleration to which each particle is subject and solve for its motion that is governed by the second order differential equation

$$\ddot{\mathbf{x}}_i = -\nabla\Phi(\mathbf{x}_i), \qquad (2.2.1)$$

where x_i is the coordinate of the i-th particle, $\ddot{x}_i$ is its acceleration and Φ is the gravitational potential determined by all the particles present in the system and that can be computed numerically as

$$\Phi(\mathbf{x_i}) = -G \sum_{j\neq i} \frac{m_j}{[||\mathbf{x} - \mathbf{x}_j||^2 + \varepsilon^2]^{1/2}}, \qquad (2.2.2)$$

where G is the gravitational constant and m_j is the mass of the j-th particle. Also, it is worth noting the presence of the parameter ε, which did not appear in the Newtonian form of the gravitational potential. This is a numerical expedient called *gravitational softening* that is necessary to ensure that the potential does not become extremely large when two particles are very close. Evaluating the potential directly with equation (2.2.2) brings to the **direct summation technique**, with which we are simply taking the sum of N individual contributions to the gravitational potential given by all other particles. Obtaining the gravitational potential allows to compute the acceleration with equation (2.2.1), from which we can compute the evolution of velocity and position of the particles solving the following system of differential equations for each particle i

$$\begin{cases} \dot{\mathbf{v}}_i = -\nabla\Phi(\mathbf{x}_i) \\ \\ \dot{\mathbf{x}}_i = \mathbf{v}_i \end{cases} . \qquad (2.2.3)$$

Equations (2.2.3) can be numerically integrated with different ODE solving methods, but a widely used method is the Leapfrog scheme. As we will discuss in Section 2.3.4, AREPO uses this very scheme to integrate equations (2.2.3).

However, to solve for the gravitational N-body problem requires more efficient techniques. In fact the sum in equation (2.2.2) requires $N - 1$ operations and has to be repeated for N particles. This requires $N(N - 1) \sim N^2$ operations and it quickly becomes computationally prohibitive for a large number of particles, as it is customary in astrophysical applications. Fortunately, there are other techniques which allow to solve this problem in a more efficient (but approximated) way reducing the numerical complexity of the solver from N^2 to N or to $N\log N$. Some of the more used techniques include the Particle-Mesh method, the Tree Method and the Tree-PM method, that we will describe in the Sections below.

2.2.1 Particle-mesh method

The **Particle-mesh** (PM) **method** (Eastwood and Hockney, 1981) exploits the fact that the Poisson's equation (that connects the gravitational potential to the density distribution)

$$\nabla^2 \Phi = 4\pi G \rho(\mathbf{x}),$$ (2.2.4)

can be simply rewritten in Fourier space as

$$\mathbf{k}^2 \hat{\Phi}(\mathbf{k}) = 4\pi G \hat{\rho}(\mathbf{k}),$$ (2.2.5)

i.e. a simple product of terms, where $\mathbf{k}$ is the wave vector. The method is performed on a Cartesian mesh: from a given distribution of particles a scheme is used to assign a mass to each grid cell[1], based on the particles inside each cell, from which it is possible to derive a smooth density field dividing the assigned cell mass for its volume. From equation (2.2.5) it is possible, after having found the Fourier transform of the density field $\hat{\rho}$, to estimate the Fourier transform of the gravitational potential $\hat{\Phi}$. The gravitational potential is then obtained with an inverse Fourier transform. The gravitational accelerations are subsequently computed from equation (2.2.1) with a finite-difference approach and interpolated to the particle positions. The main advantage of the PM method is that it is fast and simple, in fact its complexity scales with the number of particle N. The problem is that the computation of the force is bind to the mesh resolution, the force resolution cannot go beyond the size of a

---

[1]In particular AREPO uses the cloud-in-cell scheme (Eastwood and Hockney, 1981).

single mesh cell. This is particularly problematic in cosmological simulations, where a high dynamic range of scales is present. For this reason, the method is particularly suited to compute the force field from almost homogeneous distributions of matter on large scale (Springel, 2016).

2.2.2 Tree method

The Tree method (Barnes and Hut, 1986) is based on the division of the simulation domain into eight subdomains (nodes). Each subdomains is recursively divided in other eight nodes[2] until each subdomain has one or zero particles (these are called the leaves of the tree). The goal of the Tree method is to group together particles at a relatively large distance from the particle for which we want to compute the gravitational force, in order to approximate the gravitational potential with a multipole expansion, speeding up the calculation over direct summation techniques. For its nature this method is appropriate to compute the gravitational forces coming from highly clustered particles and when a high force resolution (i.e. when the forces have to be computed at small scales) is needed, in fact the resolution automatically increases in regions where the matter is more clustered. The main disadvantage is that for large scale homogeneous matter distributions the computation becomes very onerous, due to the many gravitational terms that have to be computed to obtain an almost vanishing force. Since this is the method used to solve for the gravitational potential in this Thesis, it is described in more detail in Section 2.3.4.

2.2.3 Tree-PM method

In order to overcome their disadvantages and to combine the high resolution of the Tree method and the high speed of the PM method, many N-body codes implement a combination of these two algorithms, the so-called Tree-PM method (Bode and Ostriker, 2003; Springel, 2005; Springel et al., 2021). In these methods the gravitational potential is divided in a short-range component (computed with the Tree method) and in a long-range component (computed with a PM method). This is an approach that is particularly used in large-scale cosmological simulations.

---

[2]For this reason it is also called an Oct-Tree method.

2.3 The moving-mesh code AREPO

The AREPO code (Springel, 2010a; Weinberger et al., 2020) is a moving-mesh code that uses a finite volume solver on an unstructured Voronoi mesh for hydrodynamics and a Tree-PM method to solve the Poisson equation. The presence of a mesh that is free to move with the fluid allows to mitigate the problems that affects Eulerian and Lagrangian codes, combining the high spatial adaptivity of Lagrangian codes and the ability of accurately resolve discontinuities of Eulerian codes. This is the main reason why we chose AREPO in this work. In the last years AREPO has been successfully used in computational astrophysics in a vast number of topics, for instance in state-of-the-art cosmological simulations of galaxy formation and evolution, such as Illustris (Genel et al., 2014; Vogelsberger et al., 2014), IllustrisTNG (Naiman et al., 2018; Nelson et al., 2018; Pillepich et al., 2018; Marinacci et al., 2018; Springel et al., 2018) and Auriga (Monachesi et al., 2016; Gómez et al., 2016; Marinacci et al., 2017; Grand et al., 2017), but also in smaller scale simulations of different astrophysical objects, like isolated galaxies (Jacob et al., 2018; Pascale et al., 2021), molecular filaments in galaxies (Smith et al., 2014), type Ia supernovae (Pakmor et al., 2013) and protoplanetary discs (Munoz et al., 2014).

In this Section we briefly discuss the structure of the AREPO code. In particular, we focus on the different particle types used in our simulations (Section 2.3.1), on the distinctive structure of the mesh (Section 2.3.2), on the time integration scheme employed to solve hydrodynamics (Section 2.3.3) and gravity (Section 2.3.4) and finally on the time-step constraints set in the code (Section 2.3.5).

2.3.1 Particle types

AREPO works with the definition of point-like particles, used to sample the density distribution of the different components of the system (e.g. stars, dark matter etc.), the mass of these particle defines the mass resolution of the simulation (Table 3.3). Despite being called particles, the gas particles are not point-like, in fact the gas is discretized on a grid and has properties that are continuous in space. This mesh and its dynamics are described in Section 2.3.2. The different particles are treated in various ways. A first distinction is between collision-less and collisional particles. The dark matter and stellar particles are collision-less: this means that these particles have no interactions among them except for gravity and their dynamics is driven only by gravitational forces. On the contrary, gaseous particles are collisional

and in addition to the gravitational forces we have to solve also the hydrodynamics equations. In general, in our simulations (see Chapter 3 for more details) five particle types are present:

(i) **Particle type 0**: gas particles discretized on a Voronoi mesh. These are the only particles for which the hydrodynamics equations are solved, using the scheme in Section 2.3.3. The gas particles compose the gaseous disc (see Section 3.2) and the hot corona (see Section 3.3).

(ii) **Particle type 1**: Dark matter particles, that compose the structure of the dark matter halo (see Section 3.1).

(iii) **Particle type 2**: Bulge particles, the star particles used to model the spherical bulge in the galaxy (see Section 3.1).

(iv) **Particle type 3**: Disc particles, the star particles used to model the stellar disc of the galaxy (see Section 3.2).

(v) **Particle type 4**: Newly formed stellar particles, these are the only stellar particles for which stellar evolution is computed and hence they cause stellar feedback, according to the *SMUGGLE* model (Section 2.4). Particles type 2 and 3 are considered to be old stars that have already exhausted their ability to cause feedback on the surrounding medium.

The method to assign the initial coordinates and velocities of the particles (and other characteristics for the gas cells) is explained in detail in Chapter 3.

2.3.2 Moving mesh

AREPO uses a particular mesh to partition the simulated volume with peculiar geometric and topologic properties, called Voronoi mesh. The so-called mesh generating points are the starting points around which the Voronoi cells are generated. A **Voronoi tessellation** of space consists of non-overlapping cells around each mesh-generating points such that each cell contains the region of space closer to it than any of the other mesh-generating points.

We can also define the Delaunay triangulation, formed by tetrahedra (triangles in two dimensions) that have the mesh generating points as vertices, and each circumsphere around one of these tetrahedra is not allowed to contain any other mesh-generating point inside it. In general, it is more simple to generate a Delaunay
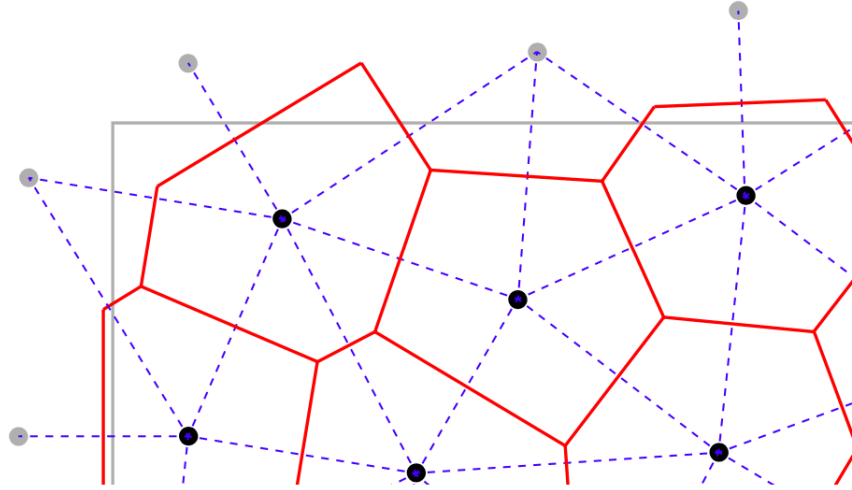
Figure 2.1: Schematic view of the Voronoi tessellation in two dimensions. The red lines show the Voronoi cells and the blue dashed lines shows the corresponding Delaunay triangulation. Black filled circles are the mesh generating points. Figure taken from Weinberger et al. (2020).

triangulation and derive from it the Voronoi tessellation. Therefore, this is what is done to build the mesh in AREPO (see Figure 2.1 for an illustration of the constituting elements of the mesh).

A fundamental property of AREPO is that it allows the grid cells to move with the fluid. At each time-step each mesh generating point is moved according to the gas bulk velocity and the Voronoi mesh is reconstructed consistently. In particular the velocity of the i-th mesh generating point is assigned as

$$\mathbf{w}_i = \mathbf{v}_i + \mathbf{v}_{\mathrm{corr,i}} \tag{2.3.1}$$

where $\mathbf{v}_i$ is the velocity of the fluid in the cell i and $\mathbf{v}_{\mathrm{corr,i}}$ is a corrective velocity (equation 2.3.4), described below. It can happen that in the reconstructed grid may be present highly distorted cells due to the fact that the mesh generating points can largely step away from the geometric centre of the cell. Such feature can decrease the accuracy of the scheme, particularly in the linear reconstruction step (equation 2.3.14). Therefore, we want the geometric centre and the mesh generating point to remain as close as possible, this can also reduce the rate at which the mesh faces can rotate during their motion. These highly distorted cells are identified by the maximum angle α_{max} within which each cell face is seen from the mesh generating point

$$\alpha_{\text{face}} = (A_{\text{face}}/\pi)^{1/2}/h_{\text{face}}, \tag{2.3.2}$$

$$\alpha_{\text{max}} = \max(\alpha_{\text{face}}), \tag{2.3.3}$$

where A_{face} is the area of each face of the cell and h_{face} is the distance between the face and the mesh generating point.

In particular, if α_{max} is greater then 0.75β, where β is a free parameter called "*cell roundness criterion*", set to $\beta = 2.25$ in our simulations, the cell is considered distorted and the velocity assigned to its mesh generating point is corrected with a velocity that points versus the center of mass of the cell, as follows (Vogelsberger et al., 2012; Weinberger et al., 2020)

$$\mathbf{v}_{\text{corr}} = \begin{cases} 0 & \text{for } \alpha_{\text{max}} \leq 0.75\beta \\ \\ f_{\text{shaping}}\frac{\alpha_{\text{max}}-0.75\beta}{0.25\beta}v_{\text{char}}\hat{\mathbf{n}} & \text{for } 0.75\beta < \alpha_{\text{max}} \leq \beta \\ \\ f_{\text{shaping}}v_{\text{char}}\hat{\mathbf{n}} & \text{for } \alpha_{\text{max}} > \beta \end{cases} \tag{2.3.4}$$

where f_{shaping} is called "*cell deformability parameter*" and is set to $f_{\text{shaping}} = 0.5$, $\hat{\mathbf{n}}$ is the normal vector to the cell and v_{char} is a characteristic velocity, corresponding to the sound speed in this work.

Another characteristic of the mesh used in AREPO is the possibility to be refined or de-refined, in this way the mass of the gas cells will have a very tight distribution around the (prescribed) mass resolution. If a cell is refined, its mesh generating point is split into a very close pair of points, while the de-refining removes a mesh generating point and its Voronoi cell, giving its volume and thermodynamic properties to the adjacent cells. These operations are triggered when a cell has less than half (de-refinement) or more than twice (refinement) mass with respect to the target mass resolution. Another operation that modifies the structure of the mesh is called conversion. Conversion happens for instance when a new stellar particle (particle type 4) is formed (see Section 2.4.2): in this case a gas cell disappears and its mass goes entirely to the stellar particle while its volume is occupied by the adjacent gas cells once the mesh is reconstructed.

2.3.3 Hydrodynamic solver

To solve the hydrodynamics equations, AREPO employs a finite-volume Godunov method on an unstructured Voronoi-mesh. The aim of this method is to employ a conservative update for the variables that describes the state of the fluid, this is done discretizing the conservative form of the Euler equations (2.3.7).

At each time-step AREPO performs the following steps to solve the hydrodynamics equations:

(i) derive the primitive variables of the fluid $\mathbf{W} = (\rho, P, \mathbf{v})$ in each cell from the conserved variables $\mathbf{Q} = (m, \mathbf{p}, E)$;

(ii) compute the gradients of the primitive variables in each cell;

(iii) assign a velocity $\mathbf{w}^n$ to each mesh generating point (equation 2.3.1);

(iv) determine the time-step from the time-step criteria (Section 2.3.5);

(v) compute the first fluxes across each cell interface using a Riemann solver;

(vi) move the mesh generating points consistently with their velocity $\mathbf{w}^n$;

(vii) compute a new Voronoi mesh, based on the new generating mesh points coordinates $\mathbf{r}'$;

(viii) compute the second fluxes on an updated mesh;

(ix) update the conserved variables in each cell, with a second order Runge-Kutta scheme (2.3.9), using the derived fluxes and obtaining the new variables $\mathbf{Q}_i^{n+1}$.

We now explain in more detail how the time integration through a finite-volume Godunov method works in AREPO. The gradients computation (step (ii)) is described in more detail later in a separate paragraph. First, for each grid cell, we define the state vector

$$\mathbf{U} = \begin{bmatrix} \rho \\ \rho\mathbf{v} \\ \rho e \end{bmatrix}, \tag{2.3.5}$$

containing, from top to bottom, density, momentum density and total energy density of the fluid. The fluxes of these variables are defined as

$$\mathbf{F}(\mathbf{U}) = \begin{bmatrix} \rho\mathbf{v} \\ \rho\mathbf{v}\mathbf{v}^T + P \\ \rho e\mathbf{v} + P\mathbf{v} \end{bmatrix}. \tag{2.3.6}$$

With these definitions the Euler equations can be written in the following compact conservative form

$$\frac{\partial \mathbf{U}}{\partial t} + \nabla \cdot \mathbf{F} = 0. \tag{2.3.7}$$

In AREPO a finite-volume strategy is employed, therefore the variables $\mathbf{U}$ are averaged inside each cell volume, obtaining the conservative variables

$$\mathbf{Q} = \int_{V_i} \mathbf{U} \, dV = (m_i, \mathbf{p}_i, E_i), \tag{2.3.8}$$

where m_i, $\mathbf{p}_i$ and E_i are the mass, the momentum and the total energy (kinetic + internal) of the i-th cell.

The conservative update of the variables $\mathbf{Q}$ in each time-step is done through a second order Runge-Kutta scheme, the Heun's method[3] (see Pakmor et al. 2016)

$$\mathbf{Q}_i^{n+1} = \mathbf{Q}_i^n - \frac{\Delta t}{2} \left(\sum_j A_{ij}^n \hat{\mathbf{F}}_{ij}^n(\mathbf{W}^n) + \sum_j A_{ij}' \hat{\mathbf{F}}_{ij}'(\mathbf{W}') \right), \tag{2.3.9}$$

where $\mathbf{Q}_i^n$ represents the variable $\mathbf{Q}$ in the i-th cell at the n-th time-step, Δt is the time-step and A_{ij} is the oriented area of the face between cells i and j. Here, the quantities with the apex n are computed in the grid from the previous time-step, the quantities with the apex $'$ are computed in the newly created Voronoi mesh. Therefore, in these scheme the fluxes have to be computed twice in two different grids for each time-step.

The coordinates of the new j-th mesh generating points are computed as follows

$$\mathbf{r}_j' = \mathbf{r}_j^n + \Delta t \mathbf{w}_j^n, \tag{2.3.10}$$

where $\mathbf{r}^n$ are the mesh generating points coordinates of the previous time-step and $\mathbf{w}^n$ are the mesh generating points velocities, computed with equation (2.3.1).

At the end of the time step these coordinates should be updated as

$$\mathbf{r}_j^{n+1} = \mathbf{r}_j^n + \frac{\Delta t}{2}(\mathbf{w}_j^n + \mathbf{w}_j'), \tag{2.3.11}$$

but, since the velocities are kept constant inside each time-step: $\mathbf{w}' = \mathbf{w}^n$, it is easy to demonstrate that

$$\mathbf{r}^{n+1} = \mathbf{r}' \tag{2.3.12}$$

---

[3]The scheme can also be thought as a hybrid method between a Runge-Kutta and a MUSCL-Hancock scheme. It has been employed instead of the original MUSCL-Hancock scheme presented in Springel (2010a).

This is fundamental because it allows to have only one mesh computation for each time-step, since it is a very onerous computational operation. The fluxes are therefore computed first from the primitive variables obtained in the previous time-step, and then from new primitive variables found with a time extrapolation as

$$\mathbf{W}_i' = \mathbf{W}_i^n + \Delta t \frac{\partial \mathbf{W}}{\partial t}. \tag{2.3.13}$$

Equation (2.3.9) is used in step (vii) to update the conservative variables inside each cell. To compute the changes of the variables inside a given cell, it is necessary to obtain the variable fluxes at each interface of the cell, quantities that measure how much mass, momentum and energy have entered and exited from the cell. Therefore, the code has to compute an approximation of the conservative variables fluxes at each interface (step v), which is done solving a so-called Riemann problem, a configuration in which we have two different constant states (left and right) separated by a single discontinuity, at each interface. This is performed with a **Riemann solver** (see Toro 2013), in particular, AREPO gives the possibility to use different types of Riemann solvers for the Euler equations (in the case of pure hydrodynamics): an exact Riemann solver or an approximate one, called HLLC (Toro et al., 1994). We used the exact Riemann solver (the default mode of operation in AREPO for hydrodynamics) for this work.

Gradients computation

The gradients are computed (step ii) using a least-square gradient estimate (Pakmor et al., 2016). This method differs from the original one by Springel (2010a) which was slightly inaccurate for distorted cells. This computation is required in order to reach a higher order spatial accuracy of the Godunov method. The primitive variables are defined at the center of each cell and finding their values at the cell interfaces allows to solve a more accurate Riemann problem at each interface.

The gradient ∇W_i of a primitive variable W_i is obtained with a linear extrapolation, such that the extrapolated value of the variable in the cell j is very close to the real one

$$\tilde{W}_j = W_i + \mathbf{d}_{ij}\nabla W_i, \tag{2.3.14}$$

where $\mathbf{d}_{ij}$ is the position vector of the j-th cell relative to the i-th cell. Of course multiple neighbour cells are involved in this computation. Therefore, to find a single value for the gradient a residuals minimization is employed, weighting the equations

squared for each couple of cells ij

$$S_{\text{TOT}} = \sum_j g_j (W_j - W_i - \mathbf{d}_{ij} \nabla W_i)^2. \qquad (2.3.15)$$

Here, $g_j = A_{ij}/|\mathrm{d}_{ij}|$ are the weights adopted, where A_{ij} is the area of the interface between the i-th and the j-th cell. Minimizing equation (2.3.15) allows to find an estimate of the gradient ∇W_i. In this way we can find a linear reconstruction of the primitive quantities $\mathbf{W} = (\rho, P, \mathbf{v})$ at the interface of the cell with equation (2.3.14), therefore allowing a better reconstruction of the primitive variable and a more accurate Riemann problem. This scheme allows to reach the second-order accuracy, but near hydrodynamical discontinuities (e.g. shock waves) it is important to reduce the order of the scheme, with a so-called slope limiter, to avoid numerical instabilities.

2.3.4 Gravitational time evolution

The gravitational time evolution is structured in the following way

(i) Computation of the gravitational potential Φ with a Tree-based method and consequent derivation of the gravitational acceleration $\mathbf{a}$.

(ii) Determination of the time-step Δt.

(iii) Time integration with a leapfrog scheme.

Gravitational potential computation

The computation of the gravitational potential Φ in AREPO is performed in general with a Tree-PM method (Section 2.2.3), this happens in cosmological simulations where the application of this method is particularly efficient. In our case we simulated an isolated galaxy and therefore we used only a Tree-based method (Section 2.2.2). After having created the tree structure (until the leaves of the tree) the computation of the potential is performed for each particle, starting from the bigger nodes with group of particles (using a multipole expansion) and then going to the sub-nodes if the approximation does not satisfy certain conditions. What is important is to determine an opening criterion, i.e. a criterion to understand if a certain multipole approximation does not differ too much from the real potential. In particular, a relative opening criterion is used

$$\frac{Gm}{d^2} \frac{L_{\text{node}}^2}{d^2} > \alpha |\mathbf{a}|, \qquad (2.3.16)$$

where m is the mass of the node, d is the distance between the node center of mass and the particle of which we are computing the potential, $\mathbf{a}$ is the acceleration of the particle at the previous time-step and α is a free parameter set to $\alpha = 0.0025$. If this criterion is satisfied, the node is opened and the potential computation is done in each sub-node. The gravitational acceleration is then obtained summing the contribute coming from each individual node (or single particle).

For the first time-step, a geometrical criterion is used, because we do not have an estimate of the acceleration in the previous time-step

$$L_{\mathrm{node}} > d\theta_{\mathrm{opening}}, \tag{2.3.17}$$

with $\theta_{\mathrm{opening}}$ a free parameter set to 0.7. This first computation of the acceleration is then repeated using the relative opening criterion (2.3.16).

Leapfrog scheme

The positions and the velocities of the particles are updated with a second-order leapfrog scheme. The characteristic that makes this method of particular interest in astrophysical numerical simulations is that it is a symplectic integrator, therefore it is an exact solution of a discrete Hamiltonian that approximates the real one of the system and it conserves its energy. A general leapfrog scheme is constructed by an alternation of drift (coordinates update) and kick (velocities update) operations

$$\begin{cases} D(\Delta t): & \mathbf{x}_i \rightarrow \mathbf{x}_i + \Delta t \mathbf{v}_i \qquad \text{(drift)} \\[2mm] K(\Delta t): & \mathbf{v}_i \rightarrow \mathbf{v}_i + \Delta t \mathbf{a}(\mathbf{x}_i) \qquad \text{(kick)} \end{cases}, \tag{2.3.18}$$

where $\mathbf{x}$ are the positions, $\mathbf{v}$ are the velocities and $\mathbf{a}$ are the accelerations of the particles. The scheme implemented in AREPO is similar to the one implemented in the GADGET-2 code (Springel, 2005), and in our case simply consists in a simple kick-drift-kick application

$$\begin{cases} \mathbf{x}_{i+1/2} = \mathbf{x}_i + \dfrac{1}{2}\Delta t \mathbf{v}_i \\[4mm] \mathbf{v}_{i+1} = \mathbf{v}_i + \Delta t \mathbf{a}(\mathbf{x}_{i+1/2}) \quad . \\[4mm] \mathbf{x}_{i+1} = \mathbf{x}_{i+1/2} + \dfrac{1}{2}\Delta t \mathbf{v}_{i+1} \end{cases} \tag{2.3.19}$$

In the first step the positions are evolved for half time-step $\Delta t/2$, then the velocities are evolved for an entire time-step Δt with the gravitational accelerations $\mathbf{a}$ computed from the updated positions $\mathbf{x}_{i+1/2}$ and finally the positions are updated for another half time-step with the newly derived velocities v_{i+1}. This method has a second-order time accuracy.

2.3.5 Time-step constraints

The time-steps Δt chosen for the time evolution of hydrodynamics and gravity are fundamental to ensure the stability of the code, in fact a time-step that is too large can lead to an unstable scheme.

The first time-step criterion valid for hydrodynamics is the *Courant-Friedrichs-Lewy* (CFL) *criterion* (Courant, Friedrichs and Lewy, 1967)

$$\Delta t \leq C_{\mathrm{CFL}} \frac{r_{\mathrm{cell}}}{v_{\mathrm{signal}}}, \qquad (2.3.20)$$

where the Courant factor C_{CFL} is a free parameter set to $C_{\mathrm{CFL}} = 0.3$ in our simulations, $r_{\mathrm{cell}} = (3V/4\pi)^{1/3}$ is the cell size, V is the cell volume, and v_{signal} is the maximum signal velocity in the fluid

$$v_{\mathrm{signal}} = \left(\gamma \frac{P}{\rho} \right)^{1/2}, \qquad (2.3.21)$$

corresponding to the sound speed. Gas bulk velocity is not taken into account (as it is done in fixed-mesh codes) because the mesh moves with the fluid flow and, therefore, *relative to the mesh*, the fluid has a small bulk velocity (much smaller than the sound speed). If magnetic fields are included, the Alfvén speed must also be considered.

The time-step for the gravitational dynamics is defined as

$$\Delta t \geq \sqrt{\frac{2C_{\mathrm{grav}}\varepsilon_{\mathrm{soft}}}{|\mathbf{a}|}}, \qquad (2.3.22)$$

where C_{grav} is a free parameter set to $C_{\mathrm{grav}} = 0.012$ in our simulations.

Also, another time-step criterion is needed to account for information from distant regions. For instance, if a shock wave is coming and the gas cell is unaware of that, the time step would be too high, causing the instability of the code. This can be

avoided using

$$\Delta t_i \geq \min_{j \neq i} \left(\frac{r_{ij}}{c_i + c_j - \mathbf{v}_{ij} \cdot \mathbf{r}_{ij} r_{ij}} \right), \qquad (2.3.23)$$

where $\mathbf{v}_{ij}$ is the velocity difference between two cells, c_i is the sound speed in the i-th cell and r_{ij} is the distance between the two cells. If a global time-step constraint is used, the time-step is chosen minimizing all the time-step just described

$$\Delta t = \min_i \Delta t_i. \qquad (2.3.24)$$

Otherwise, a more flexible scheme that uses local time-steps can be implemented. Typically, in astrophysical simulations, a wide range of density is present. For instance, in high density regions like the center of a galaxy we expect time-step smaller with respect to low density environments like in the coronal gas that surrounds galaxies or in the intergalactic medium. Therefore, evolving all the particles with the minimum time-step would result in a very poor efficient time evolution, so what is done is to allow each particle to have an individual time-step. In this way, some particles will evolve with a shorter time-step than others, with the presence of a synchronization scheme that ensures that the shorter time-steps are nested within the longer one. Local time-stepping is used also for the simulations in this work.

2.4 The *SMUGGLE* model

The **S**tars and **MU**ltiphase **G**as in **G**a**L**axi**E**s model (***SMUGGLE***; Marinacci et al. 2019) is an explicit stellar feedback and interstellar medium model for the moving-mesh code Arepo. *SMUGGLE* is a sub-resolution model[4] that describes the complex multiphase structure of the ISM and self-consistently generates gaseous outflows. Making realistic galaxy simulations requires the use of large volumes (in order to have a realistic environment and the natural interactions between different cosmic structures) while still resolving the smaller scales (to capture, for instance, the nature of star formation and SNe explosions).
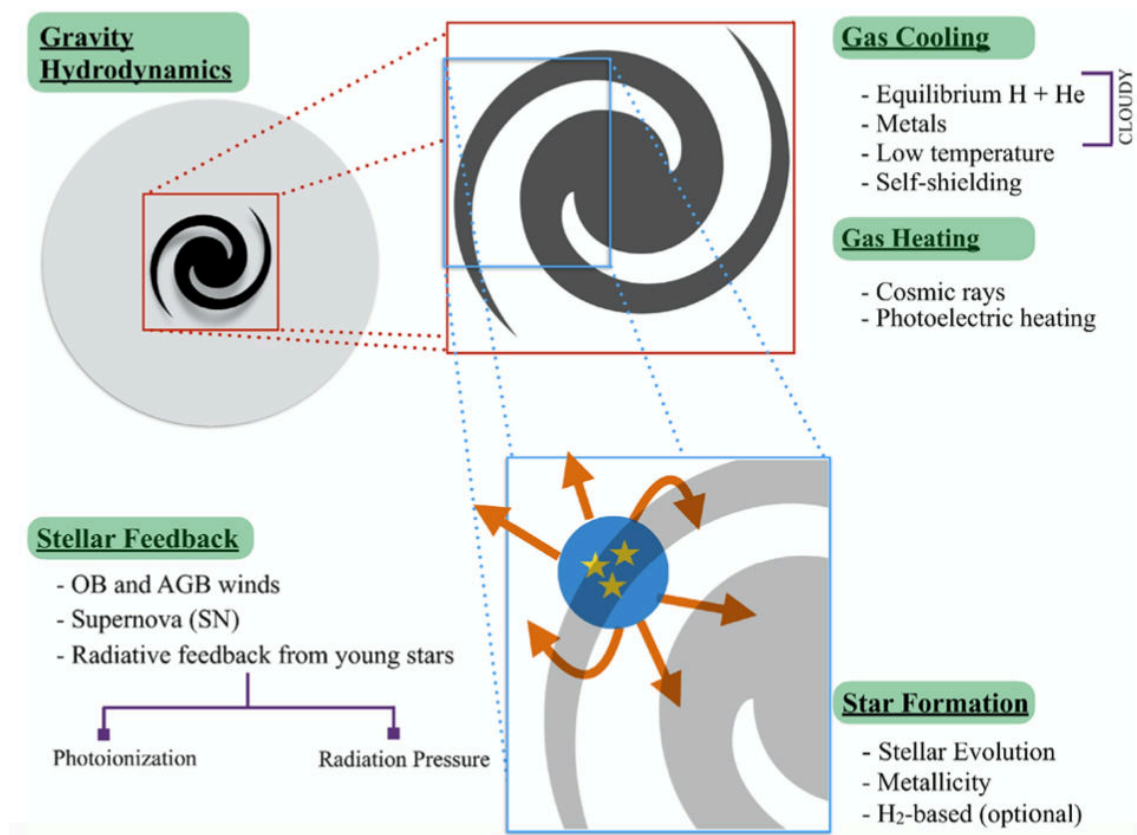

Figure 2.2: Schematic view of the main processes implemented in the *SMUGGLE* model, and their mutual interplay across spatial scales: cooling (primordial and metal line cooling, low temperature cooling and self-shielding) and heating (cosmic rays and photoelectric heating) of the gas; star formation and stellar feedback (i.e. supernovae, stellar winds and radiative feedback). Figure taken from Marinacci et al. (2019).

In general, the ISM structure is very complex, with cold, warm and hot phases

---

[4]A subresolution model is a set of numerical prescriptions used to capture physical processes that are unresolved, i.e. that happen on scales below the resolution of the simulations.

that coexist in the same environment. What is commonly done to numerically implement the ISM is to use an equation of state instead of resolving individually the different phases of the gas, for instance treating the gas as a two-fluid component with cold clouds inside a hot medium (Springel and Hernquist, 2003; Agertz et al., 2011). This could lead to an ISM model that is too smooth on parsec scales, missing its real complexity. In order to capture the ISM complex nature it is necessary to accurately model both the different gaseous phases and stellar feedback with its associated injection of energy, momentum and mass into the ISM.

In this Section we describe in detail the physical processes considered in the *SMUGGLE* model and their numerical implementation. The main processes implemented in the *SMUGGLE* model (schematically described in Figure 2.2) are:

(i) **Cooling**, in particular primordial and metal cooling lines, low-temperature cooling and an implementation of gas self-shielding, cosmic rays and photo-electric **heating processes** (Section 2.4.1);

(ii) A stochastic implementation of the **star formation** (Section 2.4.2), complemented with a prescription for stellar evolution (Section 2.4.3) taken from Vogelsberger et al. (2013).

Also, an extremely important part of this model is the implementation of the stellar feedback that occurs through three main different channels:

(iii) **Supernova feedback** (Section 2.4.4). After explaining the numerical implementation of this phenomena, we give a brief description of the SN remnant evolution and the implementation of the momentum boost from the PdV work (Section 2.4.4). Also, we explain in detail the method used to couple the energy and momentum generated to the surrounding gas (Section 2.4.4);

(iv) **Radiative feedback** (Section 2.4.5) from young and massive stars. The radiation can have an impact on the ISM mainly through **photoionization** (Section 2.4.5) and **radiation pressure** (Section 2.4.5);

(v) **Stellar winds feedback** (Section 2.4.6) from two classes of stars: OB and AGB stars.

The implementation of cooling, star formation and stellar feedback is inspired by the one in the FIRE-2 model (Hopkins et al., 2018) with some modifications.

2.4.1 Cooling and heating

Radiative cooling is the process through which gas cools down emitting photons. All these processes can be parametrized by the so-called cooling function

$$L = n^2 \Lambda_{\text{cool}}(T, X, Z) \ \text{ erg cm}^3 \ \text{s}^{-1}, \tag{2.4.1}$$

where L is the luminosity per unit volume, n is the gas number density and Λ_{cool} is the cooling function, that depends on the temperature T, on the ionization state X and on the metallicity Z of the gas.

On the other hand, also processes that heat the gas are possible, we can therefore define a heating function Λ_{heat}. The balancing between the cooling and heating functions gives the net cooling function

$$\Lambda_{\text{net}} = \Lambda_{\text{cool}} - \Lambda_{\text{heat}}. \tag{2.4.2}$$

In galaxy formation and evolution simulations accounting for the cooling and the heating of the gas is extremely important, since such processes can affect the thermal properties and state of the gas, for instance promoting or hindering the formation of stars. The main cooling and heating processes that have been considered in *SMUGGLE* are: (i) cooling from a primordial network of hydrogen (H) and helium (He) that comprehends also (ii) Compton cooling off cosmic microwave background (CMB) photons; (iii) metal line cooling. These first processes are implemented in the same way of Vogelsberger et al. (2013). In addition, the *SMUGGLE* model accounts also for (iv) low-temperature metal lines, fine structure and molecular cooling processes; (v) cosmic ray heating and (vi) photo-electric heating. Now we briefly describe each of these processes.

The total cooling rate Λ_{cool} is computed as follows

$$\Lambda_{\text{cool}} = \Lambda_{\text{p}} + \frac{Z}{Z_\odot} \Lambda_{\text{m}} + \Lambda_{\text{C}} + (1 - f_{\text{ssh}}) \Lambda_{\text{mol}}, \tag{2.4.3}$$

where Λ_{p} is the net primordial cooling rate from two-body processes, Λ_{m} is the net metal cooling rate and Λ_{C} is the cooling due to the Compton scattering with the CMB photons, $Z/Z_\odot$ is the gas metallicity in solar units, Λ_{mol} is the low temperature cooling rate (equation 2.4.6) and f_{ssh} is the gas self-shielding. A primordial mixture of H and He (i.e. H, H^+, He, He^+, He^{++}) is affected by different processes: two-body processes (collisional excitation and ionization, recombination, dielectric recombination and bremmstrahlung emission), photoionization from a UV background and

Compton cooling with the CMB photons. The **primordial net cooling rates** Λ_p are computed from ionization equations using rates from Cen (1992) and Katz et al. (1996). The metal cooling lines are computed from the CLOUDY photo-ionization code[5] (Ferland et al., 1998) assuming ionization equilibrium and a optically thin gas. In this way it is possible to compute Λ_m considering all metal lines for a given temperature and density (Smith et al., 2008). The Compton cooling off CMB photons rate is taken from Ikeuchi and Ostriker (1986)

$$\Lambda_C = 5.41 \times 10^{-36} n_e T (1+z)^4 \ \ \text{erg cm}^{-3} \ \text{s}^{-1}, \tag{2.4.4}$$

where n_e is the electrons number density, T is the temperature of the gas and z is the redshift. For both the primordial and the metal cooling rates it is important to consider also the presence of a UV background in the CLOUDY calculations, this affects the thermal and ionization state of the gas (Efstathiou, 1992; Gnedin and Hollon, 2012) decreasing the cooling rates. The photoionization and photoheating rates are obtained from the space-uniform UV background from Faucher-Giguere et al. (2009), which includes the contribute from star-forming galaxies and quasars, where galaxies are dominants at redshifts $z > 3$. In our case the simulations are performed at redshift $z = 0$ and the background is consequently taken at this redshift.

The code also accounts for **gas self-shielding**, a phenomenon that prevents UV radiation to reach the central zones of a dense gas cloud. In the outer parts the UV radiation can photoionize the hydrogen, but, as the density increases, fewer and fewer photons can reach the central zones. *SMUGGLE* accounts for the self-shielding effect using the fitting formula in Rahmati et al. (2013)

$$f_{ssh} = (1-f)\left[1 + \left(\frac{n_H}{n_0}\right)^\beta\right]^{\alpha_1} + f\left[1 + \frac{n_H}{n_0}\right]^{\alpha_2}, \tag{2.4.5}$$

where n_H is the neutral hydrogen number density and the parameters (α_1, α_2, β, f, n_0) parametrize the dependence of the self-shielding from the UV background with the redshift (see Table A1 in Rahmati et al. 2013) and have been obtained applying the radiation transfer code TRAPHIC to cosmological simulations (Pawlik and Schaye, 2008). In particular, for redshift $z = 0$ the set of parameters is: $\log(n_0/\text{cm}^{-3}) = -2.94$, $\alpha_1 = -3.98$, $\alpha_2 = -1.09$, $\beta = 1.29$, $f = 0.01$. The self-shielding parameter f_{ssh} suppresses the heating and ionization rates used for the primordial network and

---

[5]This code balances the heating and the radiative cooling to find an equilibrium solution, accounting for all the transitions of the considered atomic species.

also the input radiation field (i.e. the UV spectrum) given to the CLOUDY code for the metal line cooling calculations (the optically thin approximation is not realistic). f_{ssh} is also used for the computation of the low temperature cooling.

An important feature of the *SMUGGLE* model is the presence of cooling processes from **low temperature** metal lines, fine structure and molecules lines that allow the gas to reach very low temperatures ($T \sim 10$ K) and, consequently, to form stars in high density and low temperature regions. This cooling channel is parametrized with the fit to the CLOUDY tables computed by Hopkins et al. (2018)

$$
\Lambda_{\mathrm{mol}} = 2.896 \times 10^{-26} \Bigg\{ \left(\frac{T}{125.215\ K} \right)^{-4.9202} + \left(\frac{T}{1349.86\ K} \right)^{-1.7288} +
$$
$$
\left(\frac{T}{6450.06\ K} \right)^{-0.3075} \Bigg\}^{-1} \times \left(0.001 + \frac{0.10 n_H}{1 + n_H} + \frac{0.09 n_H}{1 + 0.1 n_H} + \frac{(Z/Z_\odot)^2}{1 + n_H} \right) \times \quad (2.4.6)
$$
$$
\left(\frac{1 + (Z/Z_\odot)}{1 + 0.00143 n_H} \right) \times \exp \left(- \left[\frac{T}{158000\ K} \right]^2 \right)\ \ \mathrm{erg\ s^{-1}\ cm^3}.
$$

Equation (2.4.6) is multiplied for the factor $(1 - f_{ssh})$ to account for the self-shielding of the gas.

It is also important to consider heating processes such as cosmic ray (Field et al., 1969) and photoelectric heating (Wolfire et al., 2003), in fact they are thought to have a fundamental role in maintaining the stability of both the cold ($T \sim 50$ K) and the warm ($T \sim 8000$ K) phases of the ISM (Wolfire et al., 1995). **Cosmic ray heating** is taken from Guo and Oh (2008)

$$
\Lambda_{\mathrm{CR}} = -10^{-16}(0.98 + 1.65) \tilde{n}_e e_{\mathrm{CR}} n_H^{-1}\ \mathrm{erg\ s^{-1}\ cm^3}, \quad\quad (2.4.7)
$$

where $\tilde{n}_e$ is the electron number density in units of the neutral hydrogen number density n_H and e_{CR} is the cosmic rays energy density that is parameterized as follows

$$
e_{\mathrm{CR}} = \begin{cases} 9 \times 10^{-12} & \mathrm{erg\ cm^{-3}}\ \ \mathrm{for}\ n_H > 0.01\ \mathrm{cm^{-3}} \\[2em] 9 \times 10^{-12} \left(\frac{n_H}{0.01\ \mathrm{cm^{-3}}} \right) & \mathrm{erg\ cm^{-3}}\ \ \mathrm{for}\ n_H \leq 0.01\ \mathrm{cm^{-3}} \end{cases} . \quad (2.4.8)
$$

Cosmic ray heating occurs through two main channels: Coulomb interactions between the cosmic rays and the electrons of the gas and hadronic collisions [6], rep-

---

[6]Cosmic rays protons can interact with the thermal gas particles producing a cascade of particle that is mainly composed of π^+, π^- and π^0.

resented, respectively, by the first and the second term in equation (2.4.7). This heating acts mainly on the dense gas, as seen in equation (2.4.8).

The second main heating process considered is the **photoelectric heating** driven by dust grains that are present in the interstellar medium. The photons of the radiation field (mainly UV radiation due to high mass young stars) can interact with the grains through photoelectric effect and extract electrons from them. Then, the heating happens through Coulomb interactions of these electrons with the free electrons of the ISM. The main contributors to this process are the polycyclic aromatic hydrocarbons (PAHs)[7]. The heating rate Λ_{phot} is taken from Wolfire et al. (2003) [8]

$$
\Lambda_{\text{phot}} = -1.3 \times 10^{-24} \tilde{e}_v^{\text{pe}} n_H^{-1} \left(\frac{Z}{Z_\odot} \right) \times
$$
$$
\left(\frac{0.049}{1 + (x_{\text{pe}}/1925)^{0.73}} + \frac{0.037(T/10^4 \text{ K})^{0.7}}{1 + (x_{\text{pe}}/5000)} \right) \text{ erg s}^{-1} \text{ cm}^3,
\tag{2.4.9}
$$

where

$$
x_{\text{pe}} \equiv \frac{\tilde{e}_v^{\text{pe}} T^{0.5}}{\Phi_{\text{PAH}} n_e}.
\tag{2.4.10}
$$

In equation 2.4.10 $\tilde{e}_v^{\text{pe}}$ is the photon energy density in Milky Way units (the so-called Habing (1968) field) and therefore it is set to $\tilde{e}_v^{\text{pe}} = e_v^{\text{pe}}/(3.9 \times 10^{-14} \text{ erg cm}^3) = 1$, Φ_{PAH} is a parameter that incorporates the electron-PAH collision rates and is set to $\Phi_{\text{PAH}} = 0.5$ from CI observations in the galactic plane (Jenkins and Tripp, 2001).

Therefore, the total heating rate is obtained as

$$
\Lambda_{\text{heat}} = \Lambda_{\text{CR}} + \Lambda_{\text{phot}}.
\tag{2.4.11}
$$

After accounting for all these processes, the total net cooling rate is obtained with equation (2.4.2).

2.4.2 Star formation

Another crucial aspect of the model is the implementation of star formation. Stars are modeled via collision-less particles (called star or stellar particles) and each of

---

[7]The PAHs are chemical compounds formed by aromatic rings of hydrogen and carbon.

[8]This is a modification of the rates from Bakes and Tielens (1994) for a higher abundance of PAHs derived from more recent observations of the Infrared Space Observatory (Tielens et al., 1999).

them represents a simple stellar population[9] (SSP). A SSP is characterized by an initial mass function (IMF) $\Phi(m)$, a function that parametrizes the mass distribution of the newly formed stars, giving the fraction of stars with a given mass inside the SSP. The integral of the IMF weighted on the mass of each star, m, is equal to the mass, $M_\star$, of the SSP (in this case the star particle) at its birth, i.e.

$$M_\star(t = t_0) = \int_{M_{\mathrm{min}}}^{M_{\mathrm{max}}} m\Phi(m)\ \mathrm{d}m, \tag{2.4.12}$$

where t_0 is the birth time of the star particle, $M_{\mathrm{min}} = 0.1$ M$_\odot$ and $M_{\mathrm{max}} = 100$ M$_\odot$. The choice of this function is extremely important because it determines, for instance, the rate of type II SNe explosions, affecting both the energy and momentum injection in the ISM and its chemical enrichment. In particular the *SMUGGLE* model uses a Chabrier (2003) IMF, characterized by a log-normal trend for low mass stars and by a power-law for higher masses

$$\Phi(m) = \begin{cases} 0.158 \left(\dfrac{1}{2.3m} \right) \exp\left[-\dfrac{(\log(m) - \log(0.08))^2}{2 \times 0.69^2} \right] & \text{for } m \leq 1\ M_\odot \\[4mm] 0.238 \times m^{-2.3} & \text{for } m > 1\ M_\odot \end{cases} . \tag{2.4.13}$$

This IMF is top-heavy compared to the Salpeter (1955)[10] IMF, meaning that from the formation of a population of stars we expect less low mass and more high mass stars compared to the Salpeter case.

The star formation process is treated with an approach based on the Springel and Hernquist (2003) model, in which a gas cell can turn into a star particle under certain conditions.

(i) At first, gas density must be above a density threshold ρ_{th} in order to allow for its gravitational collapse. Most of the star formation happens in the dense cores of giant molecular clouds in the spiral arms of the galaxy (Herbig, 1962; Cohen and Kuhi, 1979; Ward Thompson et al., 2002). The density of these systems is $\simeq 10^2 - 10^3$ cm^{-3} (Ferriere, 2001), therefore the threshold is set to

---

[9]A simple stellar population is an ideal stellar population in which all the stars: (i) are formed at the same time; (ii) have the same chemical composition.

[10]First derivation of the initial mass function, commonly used as a comparison for its simple analytic form $\Phi(m) = km^{-2.35}$.

$\rho_{\text{th}} = 100 \text{ cm}^{-3}$ and the condition is

$$\rho > \rho_{\text{th}}, \tag{2.4.14}$$

where ρ is the density of the gas cell.

(ii) The second condition restricts the star formation only to the regions that cannot resist to the gravitational collapse and therefore are gravitationally bound (Semenov et al., 2017). This information is encoded in the virial parameter defined for each gas cell i as (see Hopkins et al. 2018)

$$\alpha_i = \frac{||\nabla \otimes v_i||^2 + (c_{s,i}/\Delta x_i)^2}{8\pi G \rho_i}, \tag{2.4.15}$$

where $c_{s,i}$ is the sound speed, Δx_i is the cell size, ρ_i is the cell density, G is the gravitational constant. $||\nabla \otimes v_i||^2$ is the norm of the velocity gradient tensor[11], computed as

$$||\nabla \otimes v_i||^2 \equiv \sum_{i,j} \left(\frac{\partial v_i}{\partial x_j} \right)^2, \tag{2.4.16}$$

here v_i is the gas velocity of the i-th cell. The star formation is allowed only in star particles with $\alpha < 1$.

If these two criteria are satisfied by a given gas cell i, the star formation rate is computed as follows

$$\dot{M}_\star = \varepsilon \frac{M_{\text{gas}}}{t_{\text{dyn}}}, \tag{2.4.17}$$

otherwise it is set to zero. In equation (2.4.17) M_{gas} is the gas cell mass, ε is the star formation efficiency, set to $\varepsilon = 0.01$ as suggested by observations (e.g. Krumholz and Tan 2007), and t_{dyn} is the dynamical time

$$t_{\text{dyn}} = \sqrt{\frac{3\pi}{32 G \rho_{\text{gas}}}}, \tag{2.4.18}$$

where ρ_{gas} is the gas density. From the star formation rate $\dot{M}_\star$ of a given gas cell i it is possible to derive the stellar mass $M_{\star,i}$ that has to be formed in a time-step Δt in that cell i as

$$M_{\star,i} = M_i \left[1 - \exp\left(-\frac{\dot{M}_\star \Delta t}{M_i} \right) \right], \tag{2.4.19}$$

---

[11]$\otimes$ is the outer product, e.g. $(u \otimes v)_{ij} = u_i v_j$.

where M_i is the mass of the i-th gas cell. The stellar mass formed in this way would be much smaller than the gas cell mass. For numerical reasons, it would be better if an entire given gas cell turned into a star particle in a certain time-step, in order to have a star particle mass similar to the mass of the gas particles. This can be implemented with a stochastic method (e.g. Springel and Hernquist 2003) that, on average, recovers the correct stellar mass formed per time-step across the whole galaxy in the following way. For each cell an uniformly-distributed random variable between 0 and 1 p^* is extracted at each time step. The gas cell is then converted entirely into a star particle if $p^* < p$, where $p = 1 - \exp(-\dot{M}_\star \Delta t / M_i)$ is the fraction of the gas cell mass that would be converted in stars in a single time-step. In this way the correct stellar mass is formed in the galaxy at each time-step.

2.4.3 Stellar evolution

The stellar evolution model adopted in *SMUGGLE* is the same described in Vogelsberger et al. (2013), with the addition of stellar mass loss from OB stars (see Section 2.4.6). The main mechanisms that give back to the ISM mass and metals that have been considered in the stellar evolution model are stellar winds from young and massive OB stars and from asymptotic giant branch (AGB) stars, and supernova explosions (type II and type Ia). In this section we briefly summarize how the stellar evolution model works; more details on single evolutionary channels are given in Sections 2.4.4 and 2.4.6.

The mass and metals that are returned to the ISM are tracked as a function of time, with an approach similar to Wiersma et al. (2009). In doing so, the stellar evolution is integrated in time in order to find the mass and metal losses at each time-step (see equations 2.4.20 and 2.4.23). What is assumed is that the evolution after the main sequence happens instantaneously, this is reasonable because the post main sequence phases are much shorter ($< 1/10$ of the entire life of the star). Therefore, after a certain lifetime each star loses some fraction of its mass with a certain metallicity. This time is parametrized with the stellar lifetime function $\tau(m, Z)$, depending on the mass m and metallicity Z of the star. This function is taken from Portinari et al. (1998) and it was obtained summing the hydrogen and helium burning phases length. From this function we can evaluate the inverted lifetime function $M(t = t_0 + \tau, Z)$, that is the mass of a star leaving the main sequence at an age t (t_0 is the birth time of the star). The mass of gas that is returned to the ISM in a single time step Δt from a SSP can be obtained from the stellar recycling fraction $f_{\rm rec}(m, Z)$, i.e. the fraction of the initial mass of the star

that is released in the ISM over its entire life. Depending on the mass m and on the metallicity Z the main contribution to this recycle of mass is different. For instance, more massive stars ($> 13 M_\odot$) will lose mass mainly through type II SNe, while low mass stars will have a greater contribution from the AGB phase. The total mass released in the ISM in a time-step Δt is

$$\Delta M_{\text{rec}}(t, \Delta t, Z) = \int_{M(t+\Delta t)}^{M(t)} m f_{\text{rec}}(m, Z) \Phi(m) \text{d}m. \qquad (2.4.20)$$

Also it is important to track the release of each element. The mass of a given element i recycled to the ISM in a time-step is given by

$$\Delta M_i(t, \Delta t, Z) = Z_i \int_{M(t+\Delta t)}^{M(t)} m f_{\text{rec}}(m, Z) \Phi(m) \text{d}m = Z_i \Delta M_{\text{rec}}, \qquad (2.4.21)$$

where Z_i is the initial mass fraction of the element i. In this case the chemical enrichment was not considered and therefore the released mass has the same chemical composition of the stellar particle at its birth.

Elements are processed by thermonuclear reactions during the lifetime of a star, bringing to a chemical composition of the ejected mass that differs from the initial one of the star. To include the presence of this chemical enrichment (in particular nine elements are tracked: H, He, C, N, O, Ne, Mg, Si, Fe), it is possible to define the yield of an element i, i.e. the net created mass for each element (these have to be obtained for each mass and metal return channel), as

$$y_i(m, Z) = M_{i,\text{enrich}}(m, Z) - m Z_i f_{\text{rec}}(m, Z), \qquad (2.4.22)$$

Then, the mass of a given element returned to the ISM in a single time-step is defined as

$$\Delta M_i(t, \Delta t, Z) = \int_{M(t+\Delta t)}^{M(t)} (y_i + m Z_i f_{\text{rec}}(m, Z)) \Phi(m) \text{d}m. \qquad (2.4.23)$$

The yields for AGB stars are taken from Karakas (2010), for core collapse SNe are taken from Portinari et al. (1998), obtained using the stellar evolution tracks from Padova (e.g. Bertelli et al. 2009) and the nucleosynthesis model from Woosley and Weaver (1986). Also the stellar recycling fractions $f_{\text{rec}}(m, Z)$ have been obtained from these works. The yields for thermonuclear SNe are obtained from Thielemann et al. (2003) and Travaglio et al. (2004).

2.4.4 Feedback from supernovae

Supernova feedback is one of the main feedback processes that can occur in star-forming galaxies. It is thought to be fundamental in regulating the star formation and the structure of the ISM (e.g. Agertz et al. 2011, 2013), also generating turbulence (Martizzi et al., 2016) and galactic outflows (Li et al., 2017). Most of the times it functions as negative feedback for the star formation in the galaxy, heating the gas and generating superbubbles[12]. These can cause the formation of outflows from the disc, creating the so-called galactic fountains (Chapter 1). One of the characteristics of the *SMUGGLE* model is the ability to self-consistently generate galactic-scale outflows. In particular, the *SMUGGLE* model accounts for type II and type Ia SNe.

- **Type II supernovae** (core-collapse SNe) are considered to be the main injectors of mass and they release the majority of the α elements in the ISM. These SNe explosions originate from the collapse of high-mass stars (approximately with a mass > 8 $M_\odot$). After the formation of an iron core there are no thermonuclear reactions possible and the core collapses on itself, making the envelope fall on it and generating a shock wave that creates the SN explosion.

- **Type Ia supernovae** (thermonuclear SNe) inject the majority of iron in the ISM. Type Ia explosions occur when a white dwarf (WD) activates the burning of the carbon in a degenerate environment causing the explosion of the structure. To reach this condition the WD needs to be in a binary system. Two scenarios are possible: the so-called double and single degenerate scenarios. The *double degenerate scenario* involves the presence of a WD binary system, the merger between these two objects can form a WD with a mass greater then the Chandrasekhar mass $M_{\rm ch} \sim 1.44$ $M_\odot$ (i.e. the limit mass that can be maintained in equilibrium by mean of electron degeneracy pressure), bringing to the collapse of the structure and to the triggering of the carbon burning. In the *single degenerate scenario* the WD is in a binary system with a star that under certain conditions can lose mass that is subsequently accreted onto the WD until the carbon burning is triggered, in this situation it can happen at a mass $< M_{\rm ch}$, bringing to the so-called *Sub-Chandrasekhar Type Ia SNe*. The uncertainties on the progenitors of these SNe and on the time after the birth of a certain population at which these SNe explode make the parametrization of these phenomena not trivial.

---

[12]In an OB stars association multiple SNe can explode in a short time, each single bubble generated from the explosions can merge and form a superbubble.

Supernova remnant evolution

In order to better understand the numerical implementation of SN feedback, in this Section we briefly discuss the evolutionary phases of a SN remnant. We can schematically describe a SN as a point-like explosion. In this very small region (where is present the SN progenitor) $\sim 10^{51}$ erg of energy are released and the ejecta expands with a velocity $v_{\mathrm{ej}} \gg c_s$, where c_s is the sound speed in the ISM. Therefore, there is the formation of a shock wave that pushes and heats the gas. The SN remnant is formed by a bubble of hot and rarefied gas and by an outer shell, where almost all the material is concentrated (see Figure 2.3)[13].
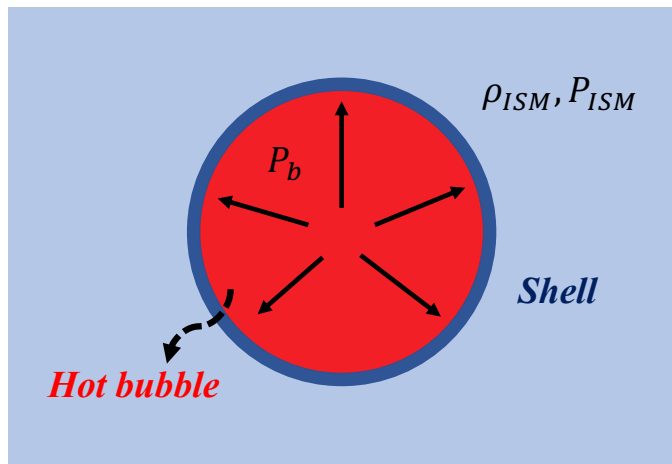
Figure 2.3: Schematic representation of a SN explosion. The blue layer is the shell and the red region is the bubble of the remnant (with an internal pressure P_b). The ISM is outside the remnant, with a density ρ_{ISM} and a pressure P_{ISM}.

The pressure of the bubble P_b is higher then the external pressure of the ISM and this causes the expansion of the remnant over the time. This expansion can be schematically divided in four phases:

(i) **Free-expansion phase**: initially the ejecta of material is expanding without any resistance from the external environment. This phase ends when the ejecta have dragged a mass of ISM approximately equal to the mass of the ejecta itself. This is a very short period that lasts ~ 200 yr;

(ii) **Sedov-Taylor phase**[14]: this is the energy-conserving phase of the supernova evolution, where radiative losses are negligible. The internal pressure gener-

---

[13]We consider a uniform density for the interstellar medium, due to the small region in which the SN explosion takes place, hence the blast wave can be approximated as spherical.

[14]This phase is named after Sedov (1946) and Taylor (1950) who independently found a self-similar solution to the Euler equation describing the time evolution of this phase.

ated by the explosion is higher than the ISM pressure, thus it is expanding the shell of the supernova remnant making mechanical PdV work and generating an increase of the momentum (see Figure 2.4) between the start and the end of this phase (the so-called momentum boost). The shell radius evolves as

$$R_s \propto \left(\frac{E_{\mathrm{SN}}}{\rho}\right)^{1/5} t^{2/5}. \qquad (2.4.24)$$

This phase lasts $\sim 10^4$ yr;

(iii) **Radiative phase**: when the shell reaches the cooling radius (after $\sim 10^4$ yr), i.e. the radius at which the cooling time is equal to the age of the SN remnant, the radiative losses become important and the remnant is not energy conserving anymore. At this radius the temperature of the shell is $\sim 10^6$ K, and in this regime the cooling function is at its peak due to the metals emission lines. In this phase the shell radius evolves as

$$R_s \propto t^{2/7}; \qquad (2.4.25)$$

(iv) **Momentum-conserving phase**: after $\sim 3 \times 10^4$ yr the gas inside the bubble radiates all its energy and the momentum reaches an asymptotic value. The shell radius evolves as

$$R_s \propto t^{1/4}. \qquad (2.4.26)$$

In Figure 2.4 we can see results from high resolution hydrodynamical simulations of SN remnants (Martizzi et al., 2015), in which we can appreciate the presence of the different phases in its evolution. In particular, we see the radial momentum (left-hand panel) and the thermal energy (right-hand panel) of a SN remnant as a function of the distance from the center of the bubble. In the first phase ($R < 4$ pc, blue line) the radial momentum increases in time due to the Sedov-Taylor phase (ii). After this phase, the thermal energy drops down due to the radiative losses (iii). Finally, the radial momentum remains constant in time (iv), but with a value that is higher then the starting momentum, in particular it can be larger by a factor of ~ 10 with respect to the initial one.
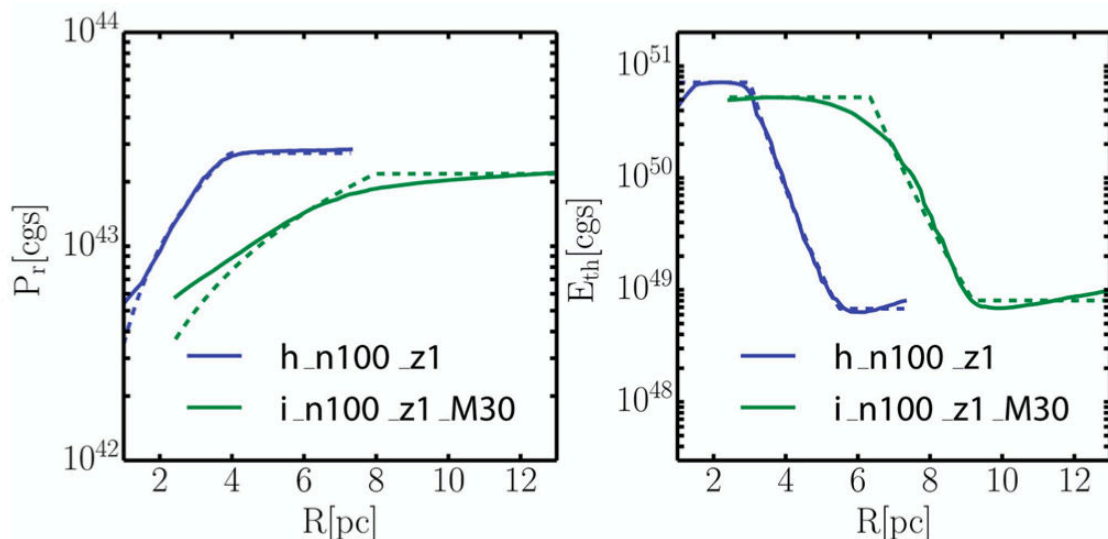
Figure 2.4: Radial momentum (left-hand panel) and thermal energy (right-hand panel) of a SN remnant as a function of the shock position R. The Figure shows results from simulations with a homogeneous medium (blue line) and an inhomogeneous medium (green line). Figure taken from Martizzi et al. (2015).

Energy and momentum budget derivation

Here we describe how the number of SNe and the consequent release of energy and momentum are implemented in the *SMUGGLE* model. The total energy injected in the ISM by a single SN is defined as

$$E_{\mathrm{SN}} = f_{\mathrm{SN}} E_{51}, \qquad (2.4.27)$$

in our simulations $f_{\mathrm{SN}} = 1$, as the average energy released per SN in the ISM is $E_{51} \sim 10^{51}$ erg.

As mentioned in Section 2.4.2, each stellar particle represents a simple stellar population, not a single star. For this reason multiple SNe can explode in a single stellar particle in a given time-step Δt. It is therefore important to compute the number of type Ia (N_{SNIa}) and type II (N_{SNII}) SNe at each time-step. In this way we can obtain the total energy $E_{\mathrm{SN,tot}}$ and momentum $p_{\mathrm{SN,tot}}$ injected in the ISM. These are defined for each star particle and each time-step as follows

$$E_{\mathrm{SN,tot}} = f_{\mathrm{SN}} E_{51} (N_{\mathrm{SNII}} + N_{\mathrm{SNIa}}), \qquad (2.4.28)$$

$$p_{\mathrm{SN,tot}} = p_{\mathrm{SNII,tot}} + p_{\mathrm{SNIa,tot}} = \sqrt{2 N_{\mathrm{SNII}} E_{\mathrm{SN}} M_{\mathrm{SNII,tot}}} +$$
$$\sqrt{2 N_{\mathrm{SNIa}} E_{\mathrm{SN}} M_{\mathrm{SNIa,tot}}}, \quad (2.4.29)$$

where $M_{\mathrm{SNII,tot}}$ and $M_{\mathrm{SNIa,tot}}$ are the total ejecta mass of the type II and type Ia SNe.

The total number and the total ejecta mass of type II SNe are found integrating the initial mass function $\Phi(m)$ (see equation 2.4.13) (Vogelsberger et al., 2013)

$$N_{\mathrm{SNII}} = \int_{\mathrm{M}(t+\Delta t)}^{\mathrm{M}(t)} \Phi(m) \, \mathrm{d}m, \quad (2.4.30)$$

$$M_{\mathrm{SNII,tot}} = \int_{\mathrm{M}(t+\Delta t)}^{\mathrm{M}(t)} m f_{\mathrm{rec}}(m, Z) \Phi(m) \, \mathrm{d}m, \quad (2.4.31)$$

where $f_{\mathrm{rec}}(m, Z)$ is the mass released from a single star with a mass m and a metallicity Z (Portinari et al., 1998) and $M(t)$ is the mass of a star leaving the main sequence at an age t (as already explained in Section 2.4.3), it is assumed that only stars between $M_{\mathrm{SNII,min}} = 8\ M_\odot$ and $M_{\mathrm{SNII,max}} = 100\ M_\odot$ can explode as type II SNe. We note that the number of type II SNe is strongly dependent on the chosen IMF because the latter determines the fraction of stars with $M > 8\ M_\odot$.

The evolution of type Ia SNe, in terms of the delay after the formation of the stellar population at which the SN Ia will occur, is unknown. The time after which the SN explodes cannot be well constrained starting from the mass of the star, as it is for type II SNe. This happens because of the uncertainties on the nature of their progenitors (single and double degenerate scenarios), on the real form of the IMF and on the fractions of binary system (that are thought to be necessary for these type of supernovae). For these reasons type Ia SN rates are not well constrained.

In *SMUGGLE* the rate has been parametrized with a delay time distribution (DTD) of SNe Ia events (Dahlen et al., 2004; Strolger et al., 2004; Greggio, 2005; Mannucci et al., 2006). The rates of type Ia SNe ($\mathrm{SNR_{Ia}}$) should follow the star formation rate (SFR) of the galaxy, but with a certain delay time, as they need the presence of a WD, the final state in the evolution of low mass stars. Hence, the $\mathrm{SNR_{Ia}}$ can be obtained with a convolution of the star formation history $\mathrm{SFR}(t)$ over the DTD

$$\mathrm{SNR_{Ia}} = \int_0^t \mathrm{SFR}(t')\mathrm{DTD}(t - t') \, \mathrm{d}t'. \quad (2.4.32)$$

The star formation history of an SSP is a Dirac delta function centered on the birth

time of the population. The number of type Ia SNe at a certain time-step Δt is, therefore,

$$N_{\text{SNIa}} = \int_t^{t+\Delta t} \text{DTD}(t')\mathrm{d}t'. \tag{2.4.33}$$

The delay time distribution is defined as a power-law in time (Maoz et al., 2012)

$$\text{DTD}(t) = \Theta(t - \tau_8)N_0 \left(\frac{t}{\tau_8}\right)^{-s} \frac{s-1}{\tau_8}, \tag{2.4.34}$$

where $\Theta(t - \tau_8)$ is the Heaviside step function[15], meaning that $\text{SNR}_{\text{Ia}} = 0$ for $t < \tau_8$. In equation (2.4.34) $\tau_8 = 40$ Myr is the main sequence life time of an 8 $M_\odot$ star, $s = 1.12$ and $N_0 = 2.6 \times 10^{-3}$ SN $M_\odot^{-1}$. Due to the nature of type Ia SN explosions the ejected mass is constant and given by $M_{\text{SNIa}} \sim 1.37$ $M_\odot$ SN^{-1}. Therefore, the total mass ejected in a time-step by a single star particle is

$$M_{\text{SNIa,tot}} = M_{\text{SNIa}} N_{\text{SNIa}}. \tag{2.4.36}$$

The metal return for both type II and type Ia SNe is computed from the stellar yields as mentioned in Section 2.4.3. The method used to distribute the mass and the metals in the ISM is described in detail in Section 2.4.4.

SN explosions are discrete events, so, to ensure this characteristic a particular time-step $\Delta t_\star$ for the stellar particles is imposed (see Section 2.3.5 for the AREPO time-step constraints)

$$\Delta t_\star = \min\left(\Delta t_{\text{grav}}, \Delta t_{\text{evol}}\right), \tag{2.4.37}$$

Δt_{grav} is the gravitational time-step and Δt_{evol} is defined as

$$\Delta t_{\text{evol}} = \min\left(\Delta t_{\text{SNII}}, \frac{t_{\text{age}}}{300}\right) \text{ yr}, \tag{2.4.38}$$

where $\Delta t_{\text{SNII}} = \tau_8/N_{\text{SNII,8}}$, $N_{\text{SNII,8}}$ is the number of type II SNe over a time τ_8. These parameters are computed consistently with the stellar evolution model (Section 2.4.3). With this time-step limit a rate of ~ 1 SN per time-step is expected.

Hence, at each time-step for each star particle we compute the total number N_{SN}

---

[15]The Heaviside step function is defined as

$$\Theta(t - \tau_8) = \begin{cases} 1 & \text{for } t \geq \tau_8 \\ 0 & \text{for } t < \tau_8. \end{cases} \tag{2.4.35}$$

of type II and type Ia SNe in a time step $\Delta t_\star$ with equations (2.4.30) and (2.4.33). Then, to obtain the actual number of SNe, we use $N_{\mathrm{SN}} = \lambda$ as the expectation value of a Poisson distribution

$$P(n; \lambda) = \frac{\lambda^n \mathrm{e}^{-\lambda}}{n!}, \tag{2.4.39}$$

from which the actual number of events per time-step $\Delta t_\star$ is sampled; that will usually be 0 or 1 SN events per time-step due to the time-step limit. From these quantities the energy, the momentum ejected from the star particle in the ISM (equations 2.4.28 and 2.4.29) and the mass and metals return are obtained.

Sedov-Taylor momentum boost

In reality, the momentum obtained with equation (2.4.29) underestimates the real one, due to the limited resolution of galaxy formation simulations ($\sim 10 - 100$ pc) that does not allow one to fully resolve the cooling radius of the supernova remnant. An analytical expression of the cooling radius, from which it is apparent that this scale can be at best only marginally resolved in our simulations, is given by (Cioffi et al., 1988)

$$r_{\mathrm{cool}} = 28.4 E_{51}^{2/7} \langle n \rangle^{-3/7} f(Z) \text{ pc}, \tag{2.4.40}$$

where E_{51} is the SN energy in units of 10^{51} erg, $\langle n \rangle$ is the average density within the cooling radius and $f(Z)$ is defined in equation (2.4.44).

We want to add to the gas the final momentum that would be generated naturally from the SN remnant evolution if we had enough resolution to resolve the cooling radius and, therefore, the Sedov-Taylor phase. Instead, due to the limited resolution of our calculations, energy and mass are returned to the ISM on scales larger than r_{cool}. The momentum boost generated by the Sedov-Taylor phase is not negligible (Figure 2.4) and, therefore, it has to be accounted in the model. High-resolution simulations of the evolution of SN remnants in a variety of environments (e.g. Cioffi et al. 1988) suggest that the value of the terminal momentum p_t (that remains constant from the momentum-conserving phase) is

$$p_t = 4.8 \times 10^5 E_{\mathrm{SN,tot}}^{13/14} \left(\frac{\langle n_H \rangle}{1 \text{ cm}^{-3}} \right)^{-1/7} f(Z)^{3/2} \text{ M}_\odot \text{ km s}^{-1}, \tag{2.4.41}$$

where $\langle n_H \rangle$ is the neutral hydrogen number density averaged around the star particle with weights determined with an SPH kernel (see equation 2.4.44) and

$$f(Z) = \min \left[\left(\frac{\langle Z \rangle}{Z_\odot} \right)^{-0.14}, 2 \right], \tag{2.4.42}$$

where $Z_\odot = 0.0127$ is the solar metallicity and $\langle Z \rangle$ is the gas metallicity averaged around the star particle in the same way of $\langle n_H \rangle$.

The momentum that is added to each gas particle influenced by a SN explosion is increased by an amount

$$\Delta p_i = \tilde{w}_i \text{min} \left[p_{\text{SN,tot}} \sqrt{1 + \frac{m_i}{\Delta m_i}}, p_t \right]. \qquad (2.4.43)$$

Here, the term $p_{\text{SN,tot}} \sqrt{1 + m_i/\Delta m_i}$, comes from the energy conservation, m_i is the gas cell mass and $\Delta m_i = \tilde{w}_i (M_{\text{SNII,tot}} + M_{\text{SNIa,tot}})$. p_t is the terminal momentum and $\tilde{w}_i$ (defined in equation 2.4.46) is a weight function used to divide the energy and the momentum injected from the SN explosion. Also, to compute the correct terminal momentum for a star particle in a time-step Δt, the terminal momentum p_t has to be multiplied by the total number of supernovae ($N_{\text{SNII}} + N_{\text{SNIa}}$) that occurs in the time-step in that star particle.

Supernova energy and momentum coupling

The energy and momentum (but also mass and metals) that come from supernovae explosions (and also from other feedback channels) have to be injected in the gas cells around the star particles. This is done using weight functions. The number of neighbours cells that are influenced by stellar feedback is defined as

$$N_{\text{ngb}} = \frac{4\pi}{3} h^3 \sum_i W(|\mathbf{r}_i - \mathbf{r}_s|, h), \qquad (2.4.44)$$

where W is the standard cubic spline SPH kernel (Monaghan and Lattanzio, 1985), h is a search radius and $|\mathbf{r}_i - \mathbf{r}_s|$ is the distance between the gas cell and the star particle. Equation (2.4.44) is solved iteratively in order to find the parameter h with a predetermined value of N_{ngb}. In our simulations we set $N_{\text{ngb}} = 64$.

To avoid numerical instabilities, Marinacci et al. (2019) imposed a limit to the radius within which the gas cells are affected by feedback. The coupling scale h_{coupling} is limited to a maximum radius R_{SB}, which in our simulations is fixed at 0.86 kpc, however, the coupling scale for the injection of mass and metals is always set to h to ensure the mass and metal conservation.

Finally, for each gas cell i the weights are defined as

$$w_i = \frac{\Delta \Omega_i}{4\pi} = \frac{1}{2} \left\{ 1 - \frac{1}{[1 + A_i/(\pi |\mathbf{r}_i - \mathbf{r}_s|^2)]^{1/2}} \right\}, \qquad (2.4.45)$$

where $A_i = \pi \Delta x_i^2$ is the gas cell area. In this way each gas cell within h_{coupling} receives a fraction of energy and momenta (while mass and metals are returned within the scale h) proportional to the fraction of the solid angle 4π covered by the cell as seen from the stellar particle position. The total energy and momentum (equations 2.4.28 and 2.4.29) is injected in each gas cell multiplied by the factor

$$\tilde{w}_i = \frac{w_i}{\sum_i w_i}, \tag{2.4.46}$$

which ensures that each cell receives the correct amount of momentum and energy.

2.4.5 Radiative feedback

Radiative feedback is thought to be important for the thermal and dynamical state of the ISM. It can affect its temperature through photoionization by young massive stars and it can inject additional momentum thanks to radiation pressure. Also, this feedback channel is important due to its timing, in fact the majority of energy and momentum is released before the first SN explosions (Murray et al., 2009; Lopez et al., 2011; Walch et al., 2012), therefore, it can disperse giant molecular clouds, setting a low-density environment and making SN feedback more efficient. Because it occurs before SN explosions it is also known as being part of the so-called early stellar feedback.

Photoionization

Young and massive stars (OB stars) are one of the main sources of photoionization in disc galaxies and cause the formation of HII regions. The photoionization is a process in which a bound electron absorbs a photon with energy high enough to remove it from the atom. In particular, for neutral hydrogen the process is

$$\text{H} + h\nu \rightarrow \text{H}^+ + e^-, \tag{2.4.47}$$

where the neutral hydrogen H is photoionized only by photons with an energy $E = h\nu > 13.6$ eV. These high-energy UV photons are abundantly produced by OB stars. Around these stars this process forms the HII regions (i.e. the so-called Strömgren sphere), in which the hydrogen is all photoionized within the Strömgren radius (the size of the HII region) and all neutral outside of it.

In the *SMUGGLE* model the ionizing photon rate emitted by a single star particle

is parametrized as

$$N_\star = \frac{L_\star}{\langle h\nu \rangle} = \frac{\gamma_\star M_\star}{\langle h\nu \rangle}, \tag{2.4.48}$$

where $L_\star$ is the star particle luminosity and $M_\star$ is the star particle mass. $\gamma_\star = 10^3 \, L_\odot/M_\odot$ is the mass-to-light ratio and $\langle h\nu \rangle = 17$ eV is the average photon energy above 13.6 eV, which corresponds to the peak emission of a black-body with a temperature $T \sim 40000$ K, consistent with the properties of OB stars (Rybicki and Lightman, 1991).

The photoionizing photons (E>13.6 eV) are all absorbed by the hydrogen within the Strömgren radius, that is most of the time smaller then the effective coupling scale h_{coupling}. For this reason a probabilistic approach is used. For each gas cell we can define a probability of being photoionized

$$\mathcal{P} = \frac{n_\star}{\alpha_{\text{rec}} n_H^2 V}. \tag{2.4.49}$$

This probability is derived assuming that the ionizing photon rate, scaled by the same weights used for the SN explosions, is equal to the recombination rate $\dot{N}_{\text{rec}}$ (i.e. the number of recombination per second)

$$n_\star = \dot{N}_{\text{rec}} = \alpha_{\text{rec}} n_H^2 V, \tag{2.4.50}$$

where $n_\star = \tilde{w}_i N_\star$, $V = 4/3\pi\Delta r^3$ is the cell volume, $n_H = X\rho/m_p$ is the average hydrogen number density in the cell (X is the hydrogen mass fraction and m_p is the proton mass) and $\alpha_{\text{rec}} = 2.6 \times 10^{-13}$ cm^3 s^{-1} is the hydrogen recombination rate.

A gas cell is considered photoionized if three conditions are satisfied, in this case the temperature of the gas cell is set to $T_{\text{phot}} = 1.7 \times 10^4$ K[16] and its cooling is disabled for a time t_{off}, equal to the star particle time-step $\Delta t_\star$:

(i) First, a number $\mathcal{P}'$ is extracted randomly between 0 and 1, the gas cell is eligible for photoionization if $\mathcal{P}' < \mathcal{P}$.

(ii) The thermal energy per mass unit of the gas cell must be $u_{\text{therm}} < 1.2 u_{\text{phot}}$, where u_{phot} is the thermal energy per mass unit corresponding to T_{phot}.

(iii) The cooling in the gas cell must be active, therefore $t_{\text{off}} = 0$.

If one of the conditions (ii) and (iii) is not satisfied it means that the gas cell is already photoionized. This mechanism causes the formation of a region with a higher

---

[16]The temperature of a hydrogen gas ionized from photons with $\langle h\nu \rangle = 17$ eV.

pressure with respect to the external neutral environment, causing the expansion of the H II region.

Radiation pressure

Another source of momentum is the pressure generated from the radiation emitted by these stars. The total momentum injected in a time-step Δt from a star particle is defined as

$$\Delta p = \frac{L_\star}{c}(1 + \tau_{\mathrm{IR}})\Delta t, \tag{2.4.51}$$

where $L_\star = \gamma_\star M_\star$ is the star particle luminosity, c is the light speed and $\tau_{\mathrm{IR}} = \kappa_{\mathrm{IR}}\Sigma_{\mathrm{gas}}$ is the gas optical depth to infrared radiation. $\kappa_{\mathrm{IR}} = 10(Z/Z_\odot)\ \mathrm{cm}^2\ \mathrm{g}^{-1}$ is the opacity in the infrared band and Σ_{gas} is the gas column density, defined using a Sobolev approximation (see Hopkins et al. 2018). In particular, the Sobolev length for each star particle j is

$$l_j = h_{\mathrm{coupling,j}} + \frac{\rho_j}{||\nabla\rho_j||}. \tag{2.4.52}$$

Here, ρ_j and $\nabla\rho_j$ are the gas density and its gradient, computed with a SPH approach. Then, the gas column density is obtained as

$$\Sigma_{\mathrm{gas,j}} = \langle\rho_s\rangle_j l_j, \tag{2.4.53}$$

where

$$\langle\rho_s\rangle_j = \sum_j W(|\mathbf{r}_i - \mathbf{r}_j|, h)m_i. \tag{2.4.54}$$

In equation (2.4.54), W is the cubic spline SPH kernel, $|\mathbf{r}_i - \mathbf{r}_j|$ is the distance between the gas cell and the star particle, m_i is the mass of the i-th gas cell and h is the coupling scale obtained solving equation (2.4.44).

This momentum is injected at each time-step in the gas cells around the star particle in the same way described in Section 2.4.4 for SNe (within h_{coupling}). Also, the same maximum coupling radius R_{SB} is used for both photoionization and radiation pressure.

2.4.6 Feedback from stellar winds

Another important feedback source is represented by stellar winds. The *SMUGGLE* model accounts for stellar winds generated by two classes of stars: young and massive type OB stars and asymptotic giant branch (AGB) stars. These provide two channels

of feedback that act at different moments. At early times winds from OB stars play an important role, in fact they can pre-process the environment dispersing the dense gas clouds, leading to a more efficient SN feedback, with a role similar to the radiative feedback (Matzner, 2002; Krumholz and Matzner, 2009). The stellar winds can also be an important feedback source at later times through AGB winds, injecting momentum and energy in the ISM.
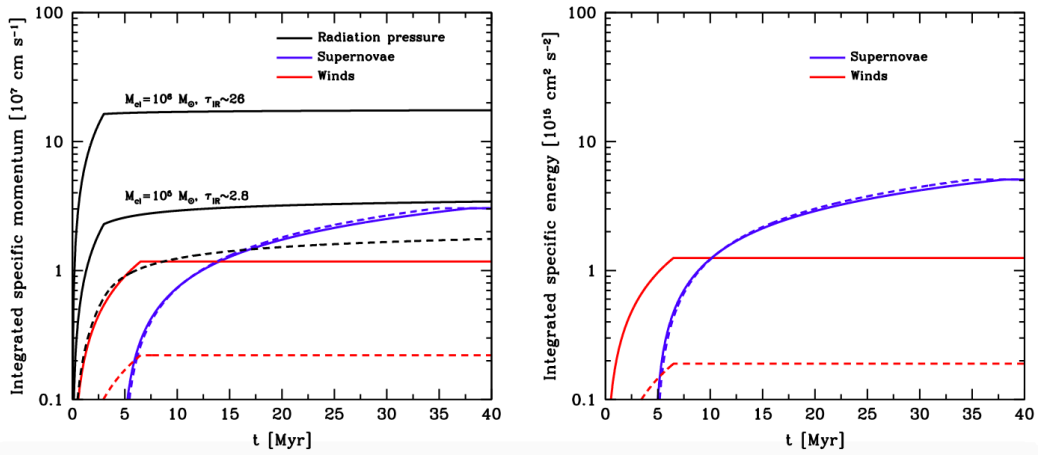

Figure 2.5: Integrated specific momentum as a function of time (left-hand panel) due to radiation pressure (black line), type II SNe (blue line) and stellar winds (red line) with $Z = Z_\odot$ (solid lines) and $Z = 0.01 Z_\odot$ (dashed lines). Also, the radiation pressure is shown for different stellar population masses (i.e. $m_\star = 10^5 \ M_\odot$ and $m_\star = 10^6 \ M_\odot$). Integrated specific energy as a function of time (right-hand panel) injected from SNe (blue line) and stellar winds (red line). Figure taken from Agertz et al. (2013).

It is worth noting that the different feedback channels considered in *SMUGGLE* have an integrated specific momentum, defined as $\int p(t)/m_\star \mathrm{d}t$, of the same order of magnitude but that is released on different time scales. Figure 2.5 shows the integrated specific momentum as a function of time due to radiation pressure, type II SNe and stellar winds. In particular, we can see how these different channels of feedback act at different times (see Agertz et al. 2013): first we have the momentum injection from stellar winds and radiative feedback that acts before the explosion of the first SNe, confirming their role in pre-processing the gas. At later times, feedback is dominated by SNe explosions.

Stellar winds in *SMUGGLE* are implemented as follows. First, the mass loss for the two type of stars is derived. The cumulative mass loss per stellar unit mass for

OB stars is parameterized as (see Hopkins et al. 2018)

$$m_{\text{closs}} = \begin{cases} f(t) & \text{if } t > 1 \text{ Myr} \\ g(t) & \text{if } 1 \text{ Myr} < t < 3.5 \text{ Myr} \\ h(t) & \text{if } 3.5 \text{ Myr} < t < 100 \text{ Myr} \end{cases}, \qquad (2.4.55)$$

where

$$\begin{cases} f(t) = 4.763 \times 10^{-3}(0.01 + \tilde{Z})t \\ \\ g(t) = 4.763 \times 10^{-3}(0.01 + \tilde{Z})\dfrac{t^{2.45+0.8\log(\tilde{Z})} - 1}{2.45 + 0.8\log(\tilde{Z})} + f(1) \\ \\ h(t) = g(3.5) - 4.57 \times 10^{-2}\left[\left(\dfrac{t}{3.5}\right)^{-2.25} - 1\right] + 4.2 \times 10^{-6}(t - 3.5) \end{cases}, \quad (2.4.56)$$

here $\tilde{Z}$ is the star particle metallicity in solar units and for $t > 100$ Myr $m_{\text{closs}} = h(100)$.

The mass and metal losses from AGB stars are treated with the AREPO stellar evolution model from Vogelsberger et al. (2013) (see Section 2.4.3). Then, the mass loss by a star particle with a mass $M_\star$ in a time-step Δt is computed as

$$M_{\text{loss}} = M_\star[m_{\text{closs}}(t + \Delta t) - m_{\text{closs}}(t)]. \qquad (2.4.57)$$

In particular, OB stellar winds are considered only for times smaller then the life time of a 8 $M_\odot$ star (i.e. the smaller progenitor of a type II SN).

The energy E_{winds} and momentum p_{winds} injected around the stellar particle at a given time-step Δt are defined as

$$E_{\text{winds}} = \Delta t L_{\text{kin}} = M_{\text{loss}} \times \Psi \times 10^{12} \text{ erg g}^{-1}, \qquad (2.4.58)$$

where

$$\Psi = \frac{5.94 \times 10^4}{1 + \left(\dfrac{t_{\text{Myr}}}{2.5}\right)^{1.4} + \left(\dfrac{t_{\text{Myr}}}{10}\right)^5} + 4.83, \qquad (2.4.59)$$

and

$$p_{\text{winds}} = \sqrt{2M_{\text{loss}}E_{\text{winds}}}. \qquad (2.4.60)$$

The assignment of these two quantities to the gas cells near the star particle is performed as in the supernova case (Section 2.4.4). The main difference is that stellar winds are a continuous phenomenon, unlike supernovae which explode in a discrete manner, and are implemented accordingly.

Initial conditions

3

The initial conditions (referred to as ICs hereafter) are the starting point from which the time evolution of any hydrodynamical N-body simulation is computed. ICs are a set of physical variables that are assigned to each particle depending on its type (Section 2.3.1). In this Chapter we describe the methods used to create these ICs for the Milky Way-like multicomponent galaxy model that we simulate in this work with the moving-mesh code AREPO. The physical properties of each component have been assigned following observational constraints. The ICs of the galaxy have been generated according to the approach adopted in Springel et al. (2005, see also Hernquist 1993 and Springel 2000). This method allows to build a multicomponent galaxy with all the the constitutive components in approximate equilibrium. These include: a dark matter halo and a stellar bulge that follow a Hernquist profile, an exponential thick stellar disc, an exponential thick gaseous disc and a galactic hot corona described by the same Hernquist profile of the dark matter halo. As described in Section 2.3.1, AREPO treats the different particle types in various ways: we assigned to both collisional and collision-less particles a set of Cartesian coordinates (x, y, z) and velocities (v_x, v_y, v_z). The collisional particles (i.e. the gas particles) are also characterized with a temperature (or more precisely by a specific internal energy) and a metallicity (Sections 3.2.5 and 3.3).

The Chapter is structured as follows. In Section 3.1 we present the theoretical density profiles and the velocity structure of the dark matter halo and the bulge. The same properties are discussed for both the stellar and gaseous discs in Section 3.2, and for the hot corona in Section 3.3. In Section 3.4 we present the numerical implementation used to sample the ICs. In Section 3.5 we illustrate the galaxy parameters used in this work. In Section 3.6 we test the ICs thus generated showing the different quantities characterizing the constitutive components of the galaxy compared with the theoretical profiles and the observational constraints.

3.1 Dark matter halo and bulge

In this Section we describe the structural and kinematic properties of the model used to sample the ICs of the dark matter halo and the stellar bulge.

The **dark matter halo** is modelled using a spherical Hernquist (1990) profile

$$\rho_{\rm dm}(r) = \frac{M_{\rm dm}}{2\pi} \frac{a}{r(r+a)^3}, \tag{3.1.1}$$

where a is the scale radius, $M_{\rm dm}$ is the total mass of the dark matter halo and $r = \sqrt{x^2 + y^2 + z^2}$ is the spherical radius. From the Hernquist profile the cumulative mass function (i.e. the mass enclosed within a radius r) can be derived analytically integrating the density profile as

$$M_{\rm dm}(r) = 4\pi \int_0^r \rho_{\rm dm}(r')r'^2 \, {\rm d}r' = M_{\rm dm}\left(\frac{r}{r+a}\right)^2, \tag{3.1.2}$$

this physical quantity will be used to sample the particles positions (Section 3.4), making sure that they follow the analytic density profile. Cosmological N-body simulations have shown that the density profiles of dark matter halos are well fitted by the so-called Navarro, Frenk and White (NFW) profile (Navarro et al., 1997)

$$\rho_{\rm dm}(r) = \frac{\rho_s}{\frac{r}{r_s}(1 + \frac{r}{r_s})^2}, \tag{3.1.3}$$

where r_s is the scale radius of the NFW profile and ρ_s is the characteristic density

$$\rho_s = \frac{200}{3}\rho_{\rm cr}\frac{c^3}{[\ln(1+c) - c/(1+c)]}. \tag{3.1.4}$$

Here, $c = r_{200}/r_s$ is the concentration parameter of the NFW profile (tipically more massive halos have smaller concentrations), where r_{200} is the radius within which the mean density of the dark matter halo is 200 times the critical density $\rho_{\rm cr}$ of the Universe [1]. However, using a Hernquist profile instead of a NFW is convenient because it brings some advantages over the NFW distribution:

(i) the Hernquist profile in the outer parts goes as $\rho(r) \propto r^{-4}$, so for $r \to +\infty$ the total mass converges, making it a more realistic configuration. Instead, the NFW profile goes as $\rho(r) \propto r^{-3}$ and a truncation of the profile is needed to have a finite mass;

---

[1] r_{200} is assumed conventionally as the virial radius of the system, in fact the virial radius corresponds to $\sim 180\rho_{\rm cr}$ for an Einstein-de Sitter Universe (Coles and Lucchin, 2003).

(ii) the Hernquist profile does have an analytic distribution function, which, in some cases simplifies the sampling of the ICs, while the NFW profile does not. This approach can be convenient, for instance, when the halo is the only component of the system or when it provides the dominant contribution to the total galaxy gravitational potential. In these cases the sampling of the distribution function can give an exact result for the system equilibrium. This approach has not been used in this work.

We associated the properties of the Hernquist model to those of a NFW profile in order to have a strict connection with the cosmological simulations. In doing so, we assume that the Hernquist profile total mass is the same mass contained in the NFW profile within the virial radius r_{200}. Then we impose the profiles to be identical in the inner parts ($r \ll r_{200}$)

$$\rho_{\mathrm{dm}} = \rho_{\mathrm{NFW}}, \tag{3.1.5}$$

and, putting together equations (3.1.4) and (3.1.5) we find the relation

$$a = r_s \sqrt{2[\ln(1+c) - c/(1+c)]}, \tag{3.1.6}$$

between the scale radii r_s and the halo concentration a.

The **bulge** is assumed to be spherical and is also modelled with a Hernquist profile

$$\rho_{\mathrm{b}}(r) = \frac{M_{\mathrm{b}}}{2\pi} \frac{b}{r(r+b)^3}, \tag{3.1.7}$$

where b is the bulge scale length. The cumulative mass function has the same form of the dark matter halo (3.1.2). The bulge mass is defined as $M_b = M_{200} m_b$, where m_b is the bulge fraction and M_{200} is the virial mass of the galaxy (the mass of the galaxy contained within r_{200}). The mass of the dark matter halo is assumed as the difference between M_{200} and the mass of all the other components (see the upcoming sections of this Chapter for their detailed description).

3.1.1 Velocity structure

Here we provide a theoretical description for the dark matter halo and bulge velocity structure. This will be important to define the three velocity component (v_x, v_y, v_z) for each particle. For spherical non-collisional structures (dark matter halo and bulge) we assume that the distribution function depends only on the energy and on

the z-component of the angular momentum L_z. In this configuration the mixed second order velocity momenta and the first momenta in radial and vertical directions are null $\langle v_R v_\phi \rangle = \langle v_R v_z \rangle = \langle v_\phi v_z \rangle = 0$, $\langle v_R \rangle = \langle v_z \rangle = 0$ (Binney and Tremaine, 2011). If the distribution function of the system were known, it would be simple to derive the velocities. However, the distribution function is unknown for our model galaxy, therefore, the particle velocities for the dark matter halo and the bulge can be derived from the Jeans equations using the so-called **Gaussian approximation**: we assume that, at each point r, the velocities (v_R, v_z, v_ϕ) in cylindrical coordinates follow a triaxial Gaussian distribution, from which they are randomly sampled. v_R is distributed as a normal distribution with dispersion σ_R and mean $\langle v_R \rangle$, the same happens for v_ϕ and v_z but with dispersions σ_ϕ and σ_z and mean $\langle v_\phi \rangle$ and $\langle v_z \rangle$. With this method we are not computing the exact equilibrium distribution, but this approximation reveals good enough for the generation of ICs that are in approximate equilibrium. Once the velocities have been sampled, we convert them in Cartesian coordinates as described in Section 3.4.2.

The non-vanishing second-momenta can be obtained from the Jeans equations as:

$$\langle v_z^2 \rangle = \langle v_R^2 \rangle = \frac{1}{\rho} \int_z^\infty \rho(z, R) \frac{\partial \Phi}{\partial z} \, \mathrm{d}z \ , \tag{3.1.8}$$

$$\langle v_\phi^2 \rangle = \langle v_R^2 \rangle + \frac{R}{\rho} \frac{\partial (\rho \langle v_R^2 \rangle)}{\partial R} + v_c^2, \tag{3.1.9}$$

where $v_c = R \, \partial \phi / \partial R$ is the circular velocity, ρ is the density of the dark matter halo or the bulge, $\langle v_\phi^2 \rangle$ is the azimuthal second order velocity moment, $\langle v_R^2 \rangle$ is the radial second order velocity moment and Φ is the total gravitational potential, which includes the contribution of all galaxy components. Also, a mean streaming component in the azimuthal direction $\langle v_\phi \rangle$ can be present. The velocity dispersion in the azimuthal direction is then

$$\sigma_\phi^2 = \langle v_\phi^2 \rangle - \langle v_\phi \rangle^2, \tag{3.1.10}$$

where $\langle v_\phi \rangle$ is the mean of the azimuthal velocity. We assume that the bulge has no net rotation, this implies that the mean streaming component is set to zero. For the dark matter halo $\langle v_\phi \rangle$ is taken as a fraction of the circular velocity $\langle v_\phi \rangle = f_c v_c$ under the assumption that the halo and the disc have the same specific angular momentum (Springel and White, 1999).

3.2 Stellar and gaseous discs

In this Section we discuss the radial (Subsection 3.2.1) and vertical (Subsection 3.2.2) structure of both stellar and gaseous discs. Furthermore, in Subsection 3.2.3 we describe the procedure used to set the disc scale length and in Subsection 3.2.4 we describe how the velocity distribution of the discs particles are sampled.

3.2.1 Radial discs structure

Observationally it has been shown that disc galaxies have radial exponential profiles (Freeman, 1970; Van Der Kruit and Searle, 1981; Courteau et al., 1996), for this reason the stellar and the gaseous discs have been modeled with exponential surface density profiles

$$\Sigma_\star(R) = \frac{M_\star}{2\pi h_\star^2}\exp(-R/h_\star) \; , \tag{3.2.1}$$

$$\Sigma_g(R) = \frac{M_g}{2\pi h_g^2}\exp(-R/h_g), \tag{3.2.2}$$

respectively. In equations (3.2.1) and (3.2.2), $h_\star$ is the scale length of the stellar disc and h_g is the scale length of the gaseous disc, $M_\star$ is the mass of the stellar disc and M_g is the mass of the gaseous disc while R is the cylindrical radius, defined as $R = \sqrt{x^2 + y^2}$. The radial cumulative mass profiles are given by

$$M_\star(R) = 2\pi \int_0^R \rho_\star(R')R' \; \mathrm{d}R' = M_\star\left[1 - \left(1 + \frac{R}{h_\star}\right)e^{-R/h_\star}\right] \; , \tag{3.2.3}$$

$$M_g(R) = 2\pi \int_0^R \rho_g(R')R' \; \mathrm{d}R' = M_g\left[1 - \left(1 + \frac{R}{h_g}\right)e^{-R/h_g}\right]. \tag{3.2.4}$$

We set $M_d = M_\star + M_g = m_d M_{200}$, where m_d is the fraction mass of the disc (summing the contributes from stellar and gaseous discs). All the parameters of our galaxy model are listed in Table 3.2.

3.2.2 Vertical discs structure

While radially both discs have an exponential profile, vertically the stellar disc follows a sech^2 profile, that corresponds to isothermal sheets perpendicular to the disc plane (Spitzer Jr, 1942; Bahcall and Soneira, 1980)

$$\rho_\star(R, z) = \frac{\Sigma_\star(R)}{2z_0} \text{sech}^2\left(\frac{z}{z_0}\right),$$ (3.2.5)

where $\rho_\star(R, z)$ is the stellar density and z_0 is a free parameter that determines the scale height of the stellar disc.

In the case of the stellar disc the parameter z_0, that sets the 'temperature', can be chosen freely (the velocities are determined in order to maintain the disc in equilibrium with this scale height in the total potential of the galaxy), but this cannot be done for the gaseous disc, in which the vertical distribution is determined by the vertical hydrostatic equilibrium, i.e. by the balance between the gas pressure and gravity (including gas self-gravity):

$$\frac{1}{\rho_g}\frac{\partial P}{\partial z} = -\frac{\partial \Phi}{\partial z}.$$ (3.2.6)

In equation (3.2.6), ρ_g is the density, P is the pressure of the gas and Φ is the total gravitational potential. For a given potential this equation is solved obtaining ρ_g, assuming that

$$\Sigma_g(R) = \int_{-\infty}^{+\infty} \rho_g(R, z)\, \mathrm{d}z,$$ (3.2.7)

where $\Sigma_g(R)$ is the gas surface density described in (3.2.2) and $\rho_g(R, z)$ is the gaseous disc density. This process is done through an iterative method, an initial potential Φ is assumed and with this initial estimate the vertical gas distribution is obtained solving equations (3.2.6) and (3.2.7). Once the vertical gas distribution is obtained, a new potential is computed with a hierarchical multipole expansion based on a tree code and the whole process is repeated until the convergence is reached, i.e. when the desired surface density at each radius is obtained.

3.2.3 Disc scale length

The scale length of the stellar disc $h_\star$ is calculated from the angular momentum of the disc assuming that the latter is related to the total angular momentum of the dark matter halo (Mo et al., 1998; Springel and White, 1999). From cosmological N-body simulations it emerges that the dark matter halos begin to rotate because of the tidal forces between them (dark matter halos are not perfectly spherical). The baryons that collapse inside the halo potential will then have a certain angular momentum. Considering a NFW profile, it is possible to calculate the total energy

of the halo truncated at r_{200} from the virial theorem as

$$E = -\frac{GM^2}{2r_{200}}f_c, \tag{3.2.8}$$

where M is the virial mass of the dark matter halo and f_c can be calculated from the concentration parameter

$$f_c = \frac{c}{2}\frac{1 - 1/(1+c)^2 - 2\ln(1+c)/(1+c)}{[c/(1+c) - \ln(1+c)]^2}. \tag{3.2.9}$$

It is often convenient to define a dimensionless spin parameter λ, that characterizes the angular momentum J, as

$$\lambda = \frac{J|E|^{1/2}}{GM_{200}^{5/2}}. \tag{3.2.10}$$

From which is simple to derive

$$J = \lambda G^{1/2}M_{200}^{3/2}r_{200}^{1/2}\left(\frac{2}{f_c}\right)^{1/2}, \tag{3.2.11}$$

where λ is a model free parameter that can be chosen to set the desired disc scale length. In fact, we assume that the angular momentum of the disc is related to the angular momentum of the halo $J_d = j_d J$. With this condition we can derive the disc scale length. In the thin disc approximation the angular momentum of the disc is given by

$$J_d = M_d \int_0^\infty V_c(R)\left(\frac{R}{h}\right)^2\exp\left(-\frac{R}{h}\right)\mathrm{d}R. \tag{3.2.12}$$

Then, for a given set of parameters: λ (spin parameter), m_d (disc mass fraction), M_{200} (virial mass of the galaxy), v_{200} (circular velocity at R_{200}) and j_d (conversion factor between the disc and the dark matter halo angular momenta), the scale length $h_\star$ is found iteratively solving equation (3.2.12) in order to obtain the best approximation for the disc angular momentum. Notice that, while the thin disc approximation assumed in equation (3.2.12) is good enough for the calculation of $h_\star$, in our ICs and in the simulations the disc has non negligible thickness, it has in fact a stratification in the z-direction (as explained in Section 3.2.2).

3.2.4 Velocity structure

Here we describe the derivation of the discs velocity structure.

For the stellar disc we adopt a Gaussian approximation for the velocity distribution (as described in Section 3.1.1) as well. Observations suggest that there is a connection between $\langle v_R^2 \rangle$ and $\langle v_z^2 \rangle$ (Hernquist, 1993), in particular we assumed $\sigma_R = \langle v_R^2 \rangle = \langle v_z^2 \rangle$. To obtain the mean streaming velocity we use the epiciclic approximation, valid for quasi-circular orbits in an axisymmetric potential

$$\sigma_\phi^2 = \frac{\sigma_R^2}{\eta^2}, \tag{3.2.13}$$

where η is defined as

$$\eta^2 = \frac{4}{R}\frac{\partial \phi}{\partial R}\left(\frac{3}{R}\frac{\partial \phi}{\partial R} + \frac{\partial^2 \phi}{\partial R^2}\right)^{-1}. \tag{3.2.14}$$

The streaming component in the azimuthal direction is set to

$$\langle v_\phi \rangle = \left(\langle v_\phi^2 \rangle - \frac{\sigma_R^2}{\eta^2}\right)^{1/2}. \tag{3.2.15}$$

For the gaseous disc only the azimuthal component has to be computed. This can be obtained from the stationary equation of momentum conservation in the radial direction tht yields

$$v_{\phi,\text{gas}}^2 = R\left(\frac{\partial \phi}{\partial R} + \frac{1}{\rho_g}\frac{\partial P}{\partial R}\right). \tag{3.2.16}$$

3.2.5 Temperature and metallicity

The gaseous components in the ICs are also characterized with a temperature profile and a metallicity distribution. The initial temperature in the disc is assumed constant at the value of 10^4 K, and from this temperature T, we obtain the internal energy per unit mass as

$$u = \frac{k_B}{\mu(\gamma - 1)m_p}T \ , \tag{3.2.17}$$

here $k_B = 1.38 \times 10^{-16}$ erg K^{-1} is the Boltzmann constant, $\gamma = 5/3$ is the adiabatic index and $\mu = 4/[8 - 5(1 - f_H)]$ is the mean molecular weight for a full ionized gas ($f_H = 0.76$ is the hydrogen mass fraction). Although the temperature is constant in the ICs, when the galaxy is evolved in time we expect the formation of a multiphase gas, with both very low ($\sim 10^2$ K) and very high temperatures ($\sim 10^6$ K), due

to cooling and heating mechanisms, to the stellar feedback, implemented in the *SMUGGLE* model (Section 2.4), and also to the mixing and accretion of the hot coronal gas. The overall metallicity of the gas in the disc is set to $Z = Z_\odot$ for simplicity (see 3.4.3 for details about the metallicity sampling).

3.3 Hot corona

In addition to the components described above, we also include a hot corona around the galaxy. As explained in Chapter 1 the corona is essential for sustaining the star formation in the disc over a long time (> 10 Gyr) and the main purpose of this Thesis project is to analyze its interaction with the material that is ejected from the disc due to stellar feedback. In particular, the properties of the hot corona have been modeled using the few observations available for this component in the Milky Way, in fact the extremely low densities of this gas makes it very difficult to observe. The corona follows the same profile of the dark matter halo (Hernquist, 1990)

$$\rho_{\mathrm{cor}}(r) = \frac{M_{\mathrm{cor}}}{2\pi} \frac{r_{\mathrm{cor}}}{r(r + r_{\mathrm{cor}})^3} \ , \tag{3.3.1}$$

where M_{cor} is the total mass and r_{cor} is the scale length of the hot corona. For simplicity we set $r_{\mathrm{cor}} = r_s$. As we will shortly discuss, this condition allows us to determine the corona temperature directly from the velocity dispersion of the dark matter halo. We assume that the coronal gas is in hydrostatic equilibrium in the dark matter halo potential, therefore the velocity field of this gaseous component is zero.

To compute the equilibrium configuration, we start from the radial Jeans equations that, under the assumption of steady-state equilibrium ($\partial/\partial t = 0$ and $\bar{v}_r = 0$) and spherical symmetry ($\bar{v}_\phi = \bar{v}_\theta = 0$, $\sigma_{\theta r}^2 = \sigma_{\theta\phi}^2 = \sigma_{\phi r}^2 = 0$ and $\sigma_{\theta\theta}^2 = \sigma_{\phi\phi}^2$) reduces to:

$$\frac{1}{\rho}\frac{\partial \rho \sigma_{rr}^2}{\partial r} + 2\frac{\sigma_{rr}^2 - \sigma_{\theta\theta}^2}{r} = -\frac{\partial \phi}{\partial r} = -\frac{GM(r)}{r^2} \ . \tag{3.3.2}$$

Assuming that the dark matter halo is isotropic ($\sigma^2 = \sigma_{rr}^2 = \sigma_{\theta\theta}^2$) yields

$$\frac{1}{\rho}\frac{\partial \rho \sigma^2}{\partial r} = -\frac{GM}{r^2}. \tag{3.3.3}$$

We note that this equation has the same functional form of the hydrostatic equilibrium equation (3.3.4).

This gaseous halo is set in hydrostatic equilibrium in the dark matter halo potential, in fact the velocity field is zero, so the corona and therefore its pressure must obey the equation

$$\frac{1}{\rho_{\mathrm{cor}}} \frac{\partial P}{\partial r} = -\frac{GM}{r^2},$$ (3.3.4)

where $P = \rho_{\mathrm{cor}} k_B T / \mu m_p$ is the gas pressure. Comparing equations (3.3.3) and (3.3.4)[2], we obtain

$$\sigma^2 = \frac{k_B T}{\mu m_p},$$ (3.3.5)

where T is the temperature of the gas, μ is the mean molecular weight and m_p is the proton mass. σ is the dark matter halo velocity dispersion, from which it is possible to derive the temperature profile of the hot corona:

$$T = \frac{\mu m_p \sigma^2}{k_B} .$$ (3.3.6)

Finally, a uniform metallicity (set to $0.1 Z_\odot$) is also assigned to the coronal gas. The computation of the metallicity is described in Section 3.4.3.

3.4 Sampling of the initial conditions

After describing the theoretical models that are at the foundations of the ICs construction, we proceed explaining how the physical properties are actually assigned to each particle. It is important to make an accurate realization of the analytical profiles described above, because these ICs are then used as a starting point to compute the time evolution of the galaxy. To do so, we need to sample the particle positions in the phase space: i.e. the position and the velocity of each particle. For the gas particles we also need to set the internal energy and the metallicity to compute their evolution in terms of metallicity and temperature. The positions and the velocities of the particles (dark matter, stars and gas) are computed directly from their respective profiles.

3.4.1 Position sampling

The particle positions of each component are derived with the **inversion method**, a general statistical method to sample a variable X from a probability density function $f_X(X)$:

---

[2]Note that we can simplify the density dependence only because the dark matter halo and the corona follow the same density profile.

(i) Given a probability density function $f_X(X)$ we calculate the cumulative distribution function

$$F_X(X) = \int_{-\infty}^{X} f_X(\tau)\, d\tau\ . \tag{3.4.1}$$

This is a monotonically non-decreasing function with values between 0 and 1.

(ii) We set $u = F_X(X)$, where u is a random number between 0 and 1 extracted from a uniform distribution.

(iii) We invert the equation to find the variable X: $X = F_X^{-1}(u)$; X will be distributed as $f_X(X)$.

In our case the density distribution is the probability density function $f_X(X)$, from which we derive F_X, i.e. the normalized cumulative mass profile.

Spherical systems

For the dark matter halo, the bulge and the hot corona the inversion can be carried out analitically, since they all follow a Hernquist profile. In this case, the normalized cumulative mass function is

$$F_X(r) = \left(\frac{r}{r+a}\right)^2 , \tag{3.4.2}$$

which, imposing

$$u = \left(\frac{r}{r+a}\right)^2 , \tag{3.4.3}$$

can be inverted to find

$$r = \frac{a\sqrt{u}}{1 - \sqrt{u}}. \tag{3.4.4}$$

In equations (3.4.2) and (3.4.3) u is a number between 0 and 1 extracted from a uniform random distribution. This procedure allows us to sample the spherical distance from the galaxy center r. To find the missing components required to attribute to each particle its (x, y, z) positions we procede as follows. We set the azimuthal coordinate ϕ as

$$\phi = 2\pi v, \tag{3.4.5}$$

where v is another random variable extracted from 0 to 1. In this way $0 < \phi < 2\pi$. The polar angle θ can go from 0 to π and is derived as

$$\theta = \text{arcos}(2w - 1), \tag{3.4.6}$$

with w being another random variable. The Cartesian coordinates (x,y,z) are then simply derived from the spherical coordinates (r,θ,ϕ):

$$x = r\sin(\theta)\cos(\phi), \tag{3.4.7}$$

$$y = r\sin(\theta)\sin(\phi), \tag{3.4.8}$$

$$z = r\cos(\theta). \tag{3.4.9}$$

Axisymmetric systems

For the stellar disc the vertical position z can be computed analitically, since the vertical profile follows a sech^2 profile (equation 3.2.5):

$$z = \frac{z_0}{2\ln(u/(1 - u))}, \tag{3.4.10}$$

where u is a random number extracted from 0 to 1. For the gaseous disc the vertical position z is derived from the vertical density structure computed as described in Section 3.2.2.

Instead, for the radial component the analytical inversion of equations (3.2.3) and (3.2.4) is not possible, but we can estimate it with the **Newton-Raphson method**, an iterative root-finding algorithm. Starting with an equation written in the form $f(x) = 0$, we find the root iteratively as follows

$$x_{n+1} = x_n - \frac{f(x_n)}{f'(x_n)}, \tag{3.4.11}$$

where x_{n+1} is a better approximation of the root. For the stellar disc $x = R/h_\star$, and $f(x_n)$ is given by

$$f(x_n) = -1 + \left(1 + x_n\right)\exp(-x_n) + u \tag{3.4.12}$$

while the first derivative $f'(x_n)$ reads

$$f'(x_n) = -x_n\exp(-x_n). \tag{3.4.13}$$

Starting from $x_1 = 1$, the process described in equation 3.4.11 is repeated until convergence is reached, in particular until $|x_{n+1} - x_n|/x_n < 10^{-7}$. Since the cumulative mass profiles are monotonically non-decreasing functions, we expect to find a solution R_i to the problem $\mathrm{M}(R_i)/M_{\mathrm{tot}} = u$, where u is a random number uniformly distributed between 0 and 1. The cylindrical radius is then obtained as $\mathrm{R} = x_n\, h_\star$. The stellar disc is sampled from 0 to ∞, while the gaseous disc extends only from 0 to $10 h_g$. Therefore, the functions $f(x_n)$ and $f'(x_n)$ used in the Newton-Raphson algorithm must be modified accordingly

$$f(x_n) = \frac{-1 + (1 + x_n)\exp(-x_n)}{1 - (1 + 10)\exp(-10)} + u, \qquad (3.4.14)$$

$$f'(x_n) = -\frac{x_n\exp(-x_n)}{1 - (1 + 10)\exp(-10)}. \qquad (3.4.15)$$

The cylindrical radius is then found as $\mathrm{R} = x_n\, h_g$. After obtaining R and z, we sample ϕ in the same way described in equation (3.4.5) and then we pass from cylindrical to Cartesian coordinates:

$$x = R\cos(\phi), \qquad (3.4.16)$$

$$y = R\sin(\phi), \qquad (3.4.17)$$

$$z = z. \qquad (3.4.18)$$

3.4.2 Velocity sampling

Here we explain how the sampling for the particle velocities is performed. For each particle position computed as described in Section 3.4.1 the velocity components are sampled from three Gaussian distributions with means and standard deviations found in Sections 3.1.1 and 3.2.4. The first step is to compute the velocity dispersions in the radial, vertical and azimuthal directions solving the differential equations described in Section 3.2.4 on a logarithmic grid in R and z. We used 512 grid points for each direction and a box size of ~ 857 kpc in which the galaxy is inserted. The use of a logarithmic grid is motivated by the fact that we want a finer sampling on each scale, from the largest to the smallest. Then, we used a bilinear interpolation to find the velocity dispersions at the particles positions. Once the velocity dispersions have been computed, we assume that the velocities (except for the coronal gas) are distributed with a normal distribution with mean and dispersion described in Section 3.2.4. For this task we applied the polar form of the **Box-Muller algorithm** (Box and Muller, 1958), a method to extract random variables that are Gaussian

distributed.

First, two pseudo-random number y_1 and y_2 are extracted from a uniform distribution (from -1 to 1). We define $r = y_1^2 + y_2^2$ and if $r = 0$ or $r \geq 1$ the couple $y_{1,2}$ is discarded and re-extracted. Otherwise we compute:

$$\xi_0 = y_{1,2}\sqrt{\frac{-2\ln r}{r}}, \qquad (3.4.19)$$

resulting in ξ_0 as being distributed as a Gaussian distribution with mean $m = 0$ and variance $\sigma^2 = 1$. The first time we set $y_{1,2} = y_1$. Then, the second time that we need another Gaussian variable, $y_{1,2} = y_2$ is directly used without the need of re-extracting another (y_1, y_2) couple. After both elements of the $y_{1,2}$ couple are used the algorithm starts again from the beginning.

If we want Gaussian distributed values with a given mean m and variance σ, we simply multiply for σ and add m. For instance, for the stellar disc we have

$$v_R = \xi_0\sqrt{\sigma_R^2}, \qquad (3.4.20)$$

$$v_z = \xi_0\sqrt{\sigma_z^2}, \qquad (3.4.21)$$

$$v_\phi = \xi_0\sqrt{\sigma_\phi^2} + \langle v_\phi \rangle. \qquad (3.4.22)$$

In this case the mean in the radial and in the vertical directions are zero, while in the azimuthal direction a free streaming component is present. This is valid also for the dark matter halo, whereas for the bulge component no net rotation is present and $\langle v_\phi \rangle = 0$ (see Section 3.1.1). Also, in the case of the gaseous disc only the azimuthal velocity component has to be computed. This is not sampled from a distribution but its value is set by equation (3.2.16, see Section 3.2.4). For the hot coronal gas all velocity components are set to zero. The velocities (v_R, v_ϕ, v_z) are then converted from cylindrical to Cartesian coordinates (v_x, v_y, v_z):

$$v_x = v_R\frac{x}{R} - v_\phi\frac{y}{R}, \qquad (3.4.23)$$

$$v_y = v_R\frac{y}{R} + v_\phi\frac{x}{R}, \qquad (3.4.24)$$

$$v_z = v_z, \qquad (3.4.25)$$

where x and y are the Cartesian coordinates of the particle (described in Section 3.4.1) and R is the cylindrical radius.

3.4.3 Metallicity sampling

In this section we describe the sampling of the metallicity for the gas particles. This is an essential component of the simulations that we performed in this work. Indeed, gas metallicity is a fundamental property in galaxy formation and evolution: its main effect is a more efficient cooling of the gas that can promote the gravitational collapse of the gas and lead initially to a more efficient star formation. Hence, it is important to model this property in a faithfully physical way, in order to obtain more realistic simulations describing galaxy evolution. In the ICs, the gas particles in the disc and in the hot corona have a homogeneous, although different, metallicity: the hot corona particles have $Z = 0.1Z_\odot$, in line with observational determinations (see Chapter 1), and the gaseous disc particles have $Z = Z_\odot$. The metallicity is treated as a passive scalar, that means that in each gas cell is evolved passively through a continuity equation

$$\frac{(\partial \rho Z)}{\partial t} + \nabla \cdot (\rho Z \boldsymbol{v}) = 0, \tag{3.4.26}$$

each gas cell has its own metallicity Z_i that is transported by the fluid.

The code traces not only the global metallicity but also the abundances of nine chemical elements (i.e. Hydrogen, Helium, Carbon, Nitrogen, Oxygen, Neon, Magnesium, Silicon and Iron). To different metallicities correspond different chemical abundances of the different elements. These are derived as follows.

Table 3.1: Primordial abundances (these abundances are mass fractions, therefore they are defined as the ratio between the mass of a given element X and the total mass of all the elements) $f_{\rm prim}$ and solar abundances $f_\odot$ of different elements: Hydrogen (H), Helium (He), Carbon (C), Nitrogen (N), Oxygen (O), Neon (Ne), Magnesium (Mg), Silicon (Si) and Iron (Fe). Solar abundances are taken from Asplund et al. (2009).

	H	He	C (10^{-3})	N (10^{-3})	O (10^{-3})	Ne (10^{-3})	Mg (10^{-3})	Si (10^{-3})	Fe (10^{-3})
$f_{\rm prim}$	0.76	0.24	0	0	0	0	0	0	0
$f_\odot$	0.7388	0.2485	2.4	0.7	5.7	1.2	0.7	0.7	1.3

The abundance of a given element X is computed with a linear interpolation between two sets of abundances: primordial abundances $f_{\rm prim}$ and solar abundances $f_\odot$, which are taken from Asplund et al. (2009) and reported on Table 3.1. Therefore,

given the gas metallicity Z_i, in each cell i we have:

$$f_{X,i} = f_{X,\text{prim},i} + \frac{Z_i}{Z_\odot}(f_{X,\odot,i} - f_{X,\text{prim},i}) \ , \qquad (3.4.27)$$

where $f_{X,\text{prim}}$ is the primordial abundance of the element X, $f_{X,\odot}$ is the solar abundance of the element X and $Z_\odot = 0.0127$ is the solar metallicity (we are considering only the nine elements in Table 3.1). In each cell the sum of the abundances of the nine elements has to be $\sum_X f_{X,i} = 1$, as the total mass has to be conserved.

3.5 Model parameters

In Table 3.2 we report the different parameters used to create our ICs. The values adopted for our galaxies are similar to those used in Marinacci et al. (2019). In particular, the total mass of the galaxy is $\sim 1.6 \times 10^{12}$ M$_\odot$, of which 1.53×10^{12} M$_\odot$ are contained in the dark matter halo, 1.5×10^{10} M$_\odot$ in the bulge and 5.63×10^{10} M$_\odot$ in the disc (stars + gas). The only parameter that changes is the mass of the corona (see Table 4.1 for more details). In Table 3.3 the resolution level adopted in our model is illustrated.

Table 3.2: *Structural parameters of the Milky Way-type galaxy.* In the first grey row, from left to right: circular velocity of the halo at r_{200} (v_{200}); dark matter halo mass (M_{dm}); dark matter halo scale length (r_s); bulge mass (M_b); bulge scale length (a); stellar disc mass ($M_\star$). In the second grey row, from left to right: stellar disc scale length ($h_\star$); stellar disc scale heigth (z_0); gaseous disc mass (M_g); gaseous disc scale length (h_g); mass of the corona (M_{cor}); corona scale length (r_{cor}).

v_{200} (km s^{-1})	M_{dm} ($M_\odot$)	r_s (kpc)	M_b ($M_\odot$)	a (kpc)	$M_\star$ ($M_\odot$)
169	1.53×10^{12}	36.46	1.5×10^{10}	1.3	4.73×10^{10}
$h_\star$ (kpc)	z_0 (pc)	M_g ($M_\odot$)	h_g (kpc)	M_{cor} ($M_\odot$)	r_{cor} (kpc)
3.8	380	9×10^9	7.6	variable	36.46

A representation of the gaseous component of the ICs is shown in the column density maps of Figure 3.1, where we can see the galaxy face-on (left-hand panel) and edge-on (right-hand panel). The presence of a galactic corona (much less dense than the disc) is particularly evident around the galaxy in the edge-on projection.

The 'cloudy' patches present in the corona density projection are caused by a low number of gas particles that does not make a smooth sampling possible.

Table 3.3: *Parameters that define the resolution level.* From left to right: gravitational softening length for dark matter particles (ε_dm); gravitational softening length for star particles ($\varepsilon_\star$); gravitational softening length for gas cells (ε_g, in this case the softening length is variable and changes with the volume of the gas cell); mass of dark matter particles (m_dm); mass of gas cells (m_g); mass of bulge particles (m_b); mass of disc particles (m_d).

ε_dm (pc)	$\varepsilon_\star$ (pc)	ε_g (pc)	m_dm $(M_\odot)$	m_g $(M_\odot)$	m_b $(M_\odot)$	m_d $(M_\odot)$
43	43	variable	10^6	3.16×10^4	10^5	8.3×10^4
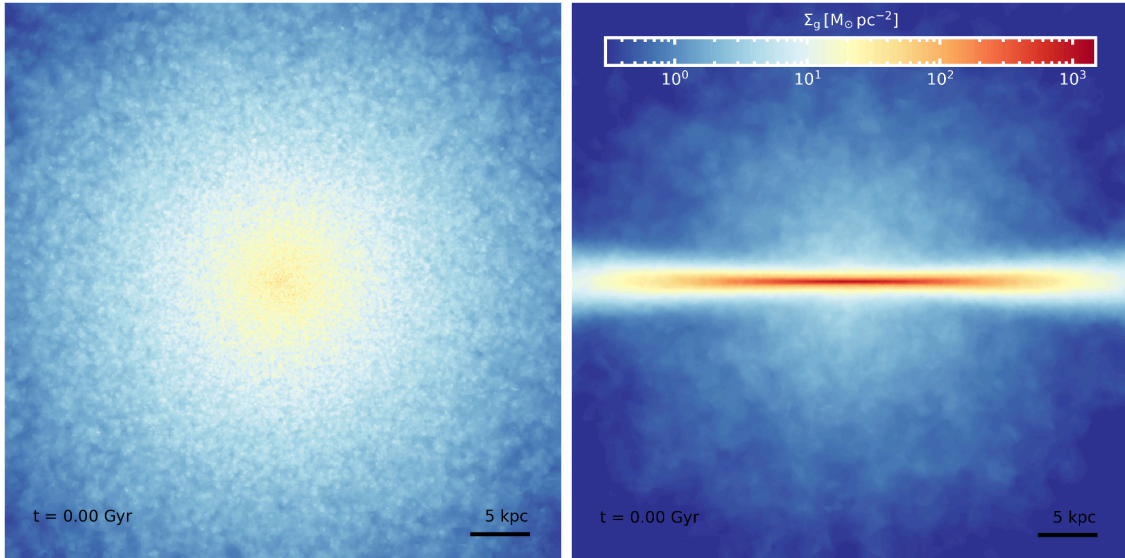
Figure 3.1: Projected density of the gas of the ICs shown face-on (left panel) and edge-on (right panel). Note the presence of the galactic corona around the disc of the galaxy in the right-hand panel.

3.6 Testing the initial conditions

In this Section we show the results obtained after testing the ICs. We will compare the profiles obtained from the ICs with the corresponding analytical models. We show different physical quantities derived from the ICs for our galaxy model. In particular we obtained density and cumulative mass profiles (Section 3.6.1), circular velocity profiles (Section 3.6.2), velocity dispersion profiles (Section 3.6.3) and temperature and metallicity profiles (Section 3.6.4).

3.6.1 Density and cumulative mass profiles

The method used to derive these profiles is different depending on the galaxy component. For spherical components (dark matter halo, bulge and hot corona) we divided the space into spherical shells. We then computed the mass of the particles within each shell and divided it by the shell volume. In this way we obtained the (volumetric) density as a function of the distance from the centre of the system. For the axisymmetric components (stellar and gaseous discs) the procedure is the same, but the space is divided into cylindrical shells (these systems have a cylindrical symmetry): in this way we derive the density at a given (galactocentric) distance from the center considering the particles with any z-values in a given bin and we obtain surface density profiles.

To each (volumetric or surface) density measurement we associate an error consisting of two terms:

(i) **Sampling error**: the operation of counting the number of particles in each bin entails a sampling error (that comes from a Poisson distribution). The sampling error of the density in the i-th bin can be calculated as follows:

$$\sigma_{p,i} = \frac{\sqrt{N_i}}{V_{s,i}} m_p, \tag{3.6.1}$$

where N_i is the number of particles in the i-th bin, m_p is the mass of the single particle and $V_{s,i}$ is the volume of the spherical or cylindrical shell. This formula is valid if all the particles of one type have the same mass.

(ii) **Root mean square error**: this error contains informations on any deviation from spherical or cylindrical symmetry of the system. The space has to be divided in different parts (we chose to divide it in octants for spherical components and in quadrants for axisymmetric components, for simplicity). In each

octant or quadrant, we calculated the density profile and evaluated the root mean square error of these different realizations of the density profile in the i-th bin as

$$\sigma_{\mathrm{rms,i}} = \sqrt{\sum_{j=1}^{n} \frac{(\hat{\rho}_i - \rho_{i,j})^2}{n}}, \qquad (3.6.2)$$

where j goes from 1 to $n = 8$ (or $n = 4$), $\hat{\rho}_i$ is the mean between the densities of the eight (or four) realizations in the i-th bin and $\rho_{i,j}$ is the density in the j-th octant (or quadrant) and in the i-th bin.

The total error in a given bin i is then calculated by summing the previous terms in quadrature

$$\sigma_{\mathrm{tot,i}} = \sqrt{\sigma_{p,i}^2 + \sigma_{\mathrm{rms,i}}^2}. \qquad (3.6.3)$$

Similarly, the cumulative mass profiles are calculated summing the mass inside the spherical radius r for the spherical components or inside the cylindrical radius R for the axisymmetric components. This is done counting the number of particles at a distance $< r$ (or $< R$) from the center of the system and multiplying it for the particle masses. We do not associate any error to this measurements.

Spherical systems

In this section we analyze the profiles obtained for the dark matter halo, the bulge and the hot corona. Figure 3.2 shows the density and cumulative mass profiles. In the dark matter halo profiles (top panel) the agreement of both the density (left-hand panel) and the cumulative mass (right-hand panel) profiles with the analytic ones is evident. The error-bars are larger in the inner parts due to the low statistics. In fact, a logarithmic grid in radius was used and for this reason only a few particles fall in the central bins. The same holds for the bulge (middle panel) and the hot corona (bottom panel) profiles. In the bottom panels the normalized residuals are displayed, the latter are defined as the difference between the values measured from the N-body realization x_i and the one from the analytic models x_{true}, this has been done for both density and cumulative mass profiles. Also, the residuals thus calculated, have been normalized by the root mean square error:

$$\mathrm{residuals} = \frac{x_{\mathrm{true}} - x_i}{\sigma_{\mathrm{rms,i}}}. \qquad (3.6.4)$$

The errors on the residuals are computed as the errors on the density points ρ_{true}, normalized by σ. It is apparent that the residuals are extremely low ($< 1\%$), except
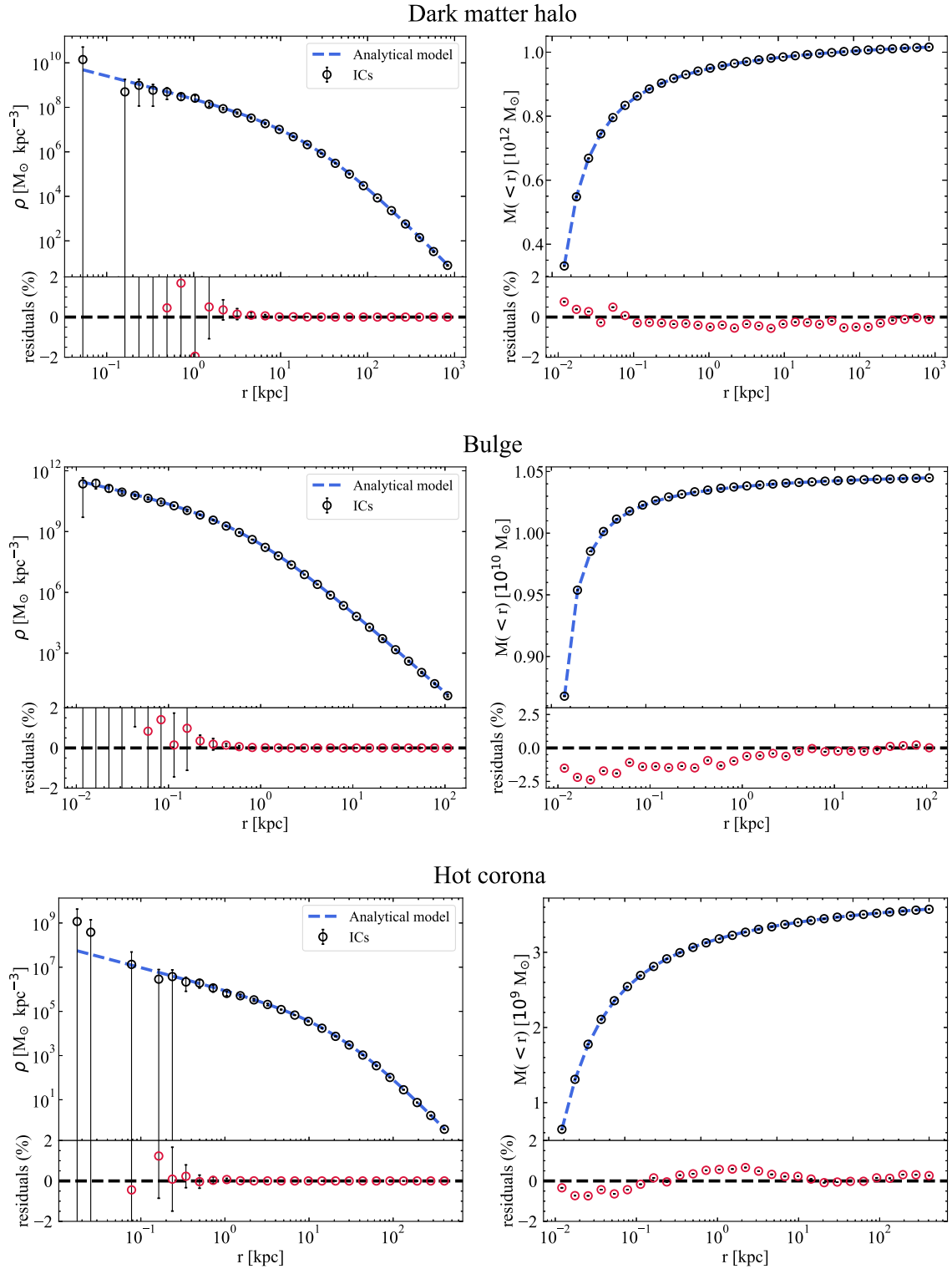
Figure 3.2: Density profile (left-hand panel) and cumulative mass profile (right-hand panel) of dark matter halo (top panel), bulge (middle panel) and corona (bottom panel). The black points with error-bars represent the ICs. The dashed blue lines represent the analytical model (Hernquist profile, equations 3.1.1 and 3.1.7). In the lower panels the red points represent the residuals between the analytical profile and the sampled points; the dashed black line indicates the zero residual.

for the density points in the inner bins where, however, within the error-bars the residuals are still consistent with zero. It is clear how the ICs points reproduce well the analytical profiles within the associated errors. This means that the analytical profiles are approximated very well by the sampling made for the construction of these ICs.

Axysimmetric systems
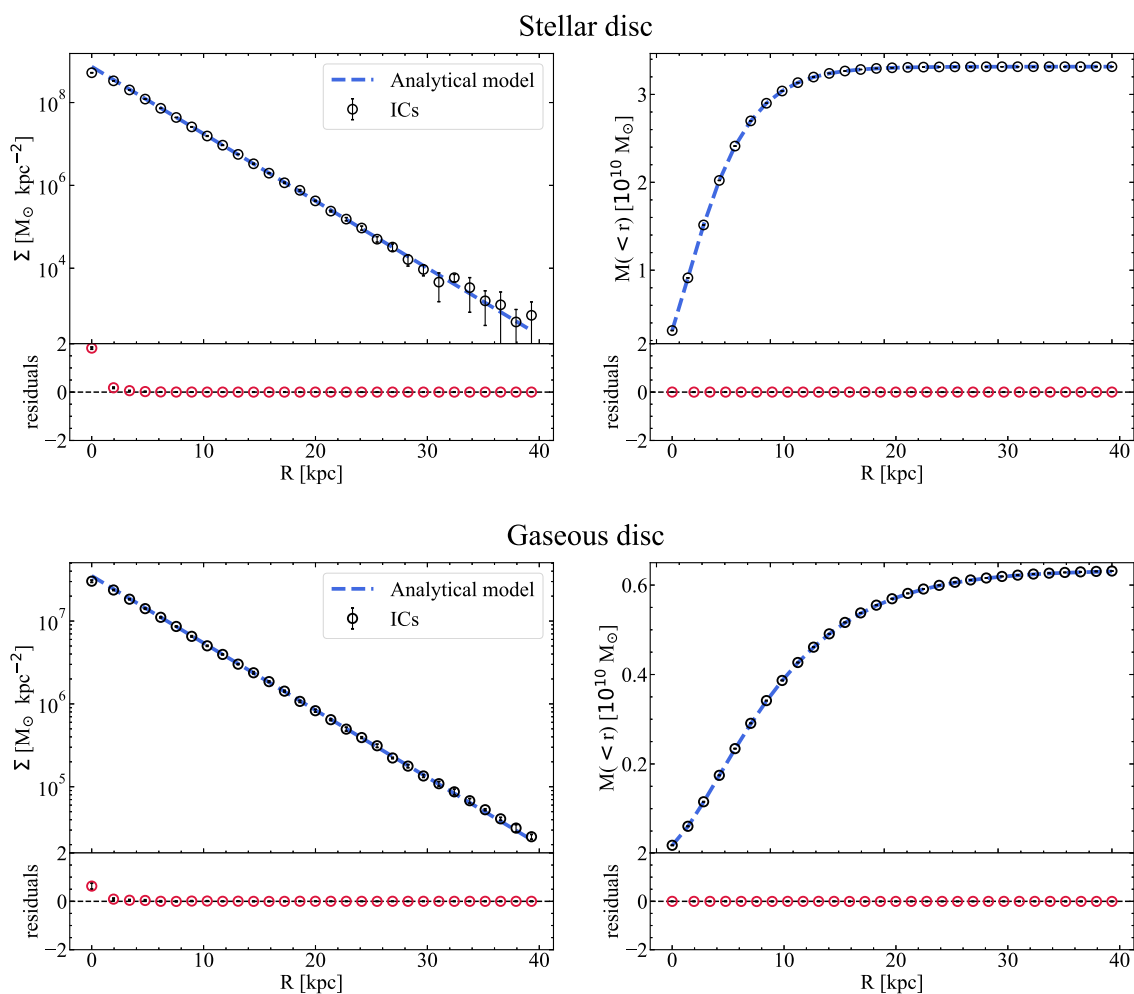
Figure 3.3: Surface density profile (left-hand panels) and cumulative mass profile (right-hand panels) of the stellar (top panels) and gaseous (bottom panels) discs. The black points with error-bars represent the ICs. The dashed blue lines represent the analytical model (exponential disc, equations 3.2.1 and 3.2.2). In the lower panels the red points represent the residuals between the analytical profile and the sampled points; the dashed black line is the zero residual.

In Figure 3.3 we show the density and cumulative mass profiles of the stellar (top panel) and the gaseous discs (bottom panel). Here, the error-bars are larger in the outer parts because a linear grid in radius was used and a lower particle count is present in the external regions. For these components the residuals (red points in the lower panels) are consistent with zero, therefore the points derived from the ICs are in very good agreement with the analytical profiles described in Section 3.2.1.

3.6.2 Rotation curve

In this Section we show the rotation curves derived from the ICs and we compare them with the analytical profiles and with the observed values in the Milky Way. A rotation curve is a profile that shows the circular velocity (the velocity that an object at a certain distance would have to maintain a circular motion in a given gravitational potential Φ) as a function of the distance from the centre of the system. The rotation curves have been fundamental in astrophysics in general, since their observation in spiral galaxies is one of the major evidence of the existence of dark matter (Van de Hulst et al., 1957; Rubin et al., 1978). Reproducing these curves correctly is fundamental to obtain a realistic setup for our galaxy model.

The circular velocity for the spherical components (dark matter halo, bulge and hot corona) is derived from the first and the second Newton's theorems. In a spherical system the circular velocity at a distance r from the center is

$$v_c^2(r) = \frac{GM(r)}{r},$$

(3.6.5)

where $M(r)$ is the total mass enclosed within the spherical radius r.

For the disc components we are assuming a thin disc approximation, for simplicity. The potential produced by this system in cylindrical symmetry can be calculated as (Binney and Tremaine, 2011)

$$\Phi(R) = -2\pi G \int_0^\infty \hat{\Sigma}_0(k) e^{-k|z|} J_0(kR) \, dk \ ,$$

(3.6.6)

where $\hat{\Sigma}_0(k)$ is the Hankel transform of the disc surface density Σ and $J_0(kR)$ is the Bessel function of the first kind. Knowing the disc potential we can obtain the circular velocity from the equality:

$$\frac{v_c^2(R)}{R} = \frac{\partial \Phi(R)}{\partial R} \ .$$

(3.6.7)

The circular velocities, for the stellar and gaseous components respectively, are

$$v_{c,\star}^2(R) = \frac{2GM_\star}{h_\star}y^2[I_0(y)K_0(y) - I_1(y)K_1(y)] \; , \tag{3.6.8}$$

$$v_{c,g}^2(R) = \frac{2GM_g}{h_g}x^2[I_0(x)K_0(x) - I_1(x)K_1(x)] \; , \tag{3.6.9}$$

where $x = R/(2h_g)$ and $y = R/(2h_\star)$. I_n and K_n are the modified Bessel functions of the first and second kind, respectively,

$$I_\alpha(x) = \sum_{m=0}^{\infty} \frac{1}{m!\Gamma(m+\alpha+1)}\left(\frac{x}{2}\right)^{2m+\alpha}, \tag{3.6.10}$$

$$K_\alpha(x) = \frac{\pi}{2}\frac{I_{-\alpha}(x) - I_\alpha(x)}{\sin(\alpha\pi)}, \tag{3.6.11}$$

where Γ is the gamma function.
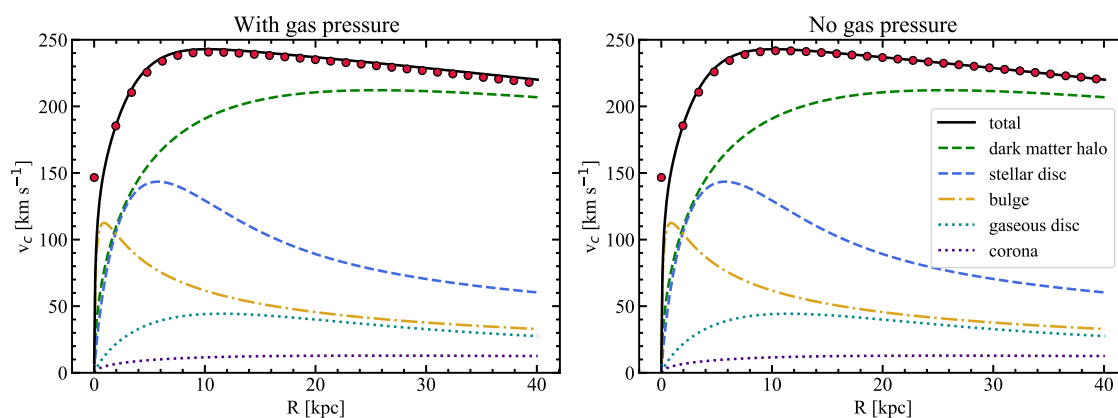
Figure 3.4: Rotation curve of the gaseous disc taking into account (left-hand panel) and without taking into account (right-hand panel) the gas pressure support. The solid black line represents the total rotation curve, the dashed lines represent the rotation curve of the different components: dark matter halo (green); stellar disc (blue); bulge (yellow); gaseous disc (light blue); corona (purple). The red points with error-bars are the azimuthal component of the velocity v_ϕ computed from the ICs.

Finally, the total circular velocity is given by

$$v_c^2(R) = \frac{G[M_{\rm dm}(< R) + M_{\rm b}(< R) + M_{\rm cor}(< R)]}{R} + v_{c,\star}^2(R) + v_{c,g}^2(R), \tag{3.6.12}$$

where $M_{\rm dm}(< R)$, $M_{\rm b}(< R)$ and $M_{\rm cor}(< R)$ are the cumulative mass functions of

dark matter halo, bulge and hot corona and $v_{c,\star}(R)$ and $v_{c,g}(R)$ are the circular velocity profiles of the stellar and the gaseous disc.

The measurement of the circular velocity in the ICs is made with a method similar to the one used for determining the density profiles (Section 3.6.1). First we divided the system in cylindrical shells. Then, for each gas or stellar particle, we derived the azimuthal velocity v_ϕ from the velocity in Cartesian components as

$$v_\phi = -v_x \sin\theta + v_y \cos\theta, \qquad (3.6.13)$$

where $\sin\theta = y/R$ and $\cos\theta = x/R$. In each shell j we computed the mean of the azimuthal velocities weighted by the mass of the individual gas (or star) particles

$$\bar{v}_{\phi,j} = \frac{\sum_i v_{\phi,i} m_i}{\sum_i m_i}, \qquad (3.6.14)$$

obtaining a circular velocity profile. In equation (3.6.14) the sums go from 1 to the number of particle inside the j-th shell. To these measurement we associated an uncertainty as the root mean square error between different realizations of the circular velocity profiles, as described in equation (3.6.2).
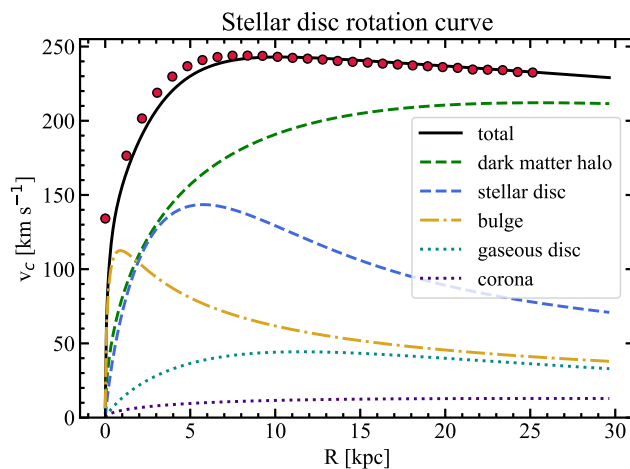
Figure 3.5: Rotation curve of the stellar disc. The solid black line represents the total rotation curve, the dashed lines represent the rotation curve of the different components: dark matter halo (green); stellar disc (blue); bulge (yellow); gaseous disc (light blue); hot corona (purple). The red points with error-bars are the azimuthal component of the velocity v_ϕ for the star particles computed from the ICs.

In Figure 3.4 we show the rotation curve for the gaseous disc. The red points with error-bars [3] represent the circular velocity v_ϕ derived from the ICs of the galaxy,

---

[3]In this case the error-bars are very small and cannot be seen in the Figures.

whereas the black solid line represents the total analytical circular velocity that is expected considering all the different galaxy components, computed with equation (3.6.12).

The dashed lines represent the contribution given from each single component: dark matter halo (green), stellar disc (blue), bulge (yellow), gaseous disc (light blue), hot corona (purple), computed using the single terms in equation (3.6.12). As we can see the gaseous components (gaseous disc and hot corona) do not contribute significantly at any radius to the total circular velocity. In the inner parts (< 1 kpc) the bulge is the dominant component, whereas in the outer parts the rotation curve is totally dominated by the dark matter halo. It is important to note that the red points are almost always under the analytical profile. This is due to the fact that we are considering the gaseous disc. In fact, the azimuthal velocity for this component in the ICs is calculated with equation (3.2.16) considering also the pressure support of the gas. The analytical curves are derived considering equation (3.6.7) and they do not include the contribution of pressure support, for this reason in Figure 3.4 it seems as if we are overestimating the circular velocity with respect to the analytical profile. This is demonstrated in the right-hand panel of Figure 3.4, where the rotation curve is plotted without considering the contribution of the gas pressure. We can see that the red points are almost perfectly lying on the analytical black curve.

In Figure 3.5 we show the rotation curve for the stellar disc. In this case the ICs (red points) show a very good agreement with the analytical profile for radius $R > 10$ kpc, since stars are collision-less particles and have not an associated pressure.

We also performed a consistency check on the rotation curve derived from our ICs comparing it to observations of the circular velocity at the solar radius. In particular, the circular speed at the solar radius ($R_\odot \sim 8$ kpc) is (Binney and Tremaine, 2011):

$$v_c(R_\odot) = (220 \pm 20) \text{ km s}^{-1}, \tag{3.6.15}$$

and this is a value consistent with that obtained in our ICs (~ 240 km s^{-1}).

3.6.3 Velocity dispersion

In this Section we show the velocity dispersion profiles for the dark matter halo and the bulge and the vertical velocity dispersion profile for the stellar disc.

Dark matter halo and bulge velocity dispersion

The velocity dispersion profiles for the spherical components are obtained in the following way. First the space is divided into spherical shells. To each particle is associated a velocity vector (v_x, v_y, v_z) as described in Section 3.4.2. The velocity dispersion in each shell is computed as the standard deviation of the (x, y, z)-component of the velocities. For instance, for the velocity dispersion of v_x we obtain

$$\sigma_x = \sqrt{\frac{\sum_{i=1}^{N}(v_{x,i} - \bar{v}_x)^2}{N}} = \sqrt{\frac{1}{N}\sum_{i=1}^{N}(v_{x,i}^2) - \bar{v}_x^2}, \qquad (3.6.16)$$

where $\bar{v}_x$ is the mean of v_x weighted on the mass, computed as in equation (3.6.14), for the particles inside the i-th shell and N is the number of particle in the shell. In this case the error-bars are computed as the dispersion between different realizations of the velocity dispersion profile (the space is divided in octants as for the density profiles). In Figure 3.6.3 we show the velocity dispersions as a function of the radius for the dark matter halo (left-hand panel) and the bulge (right-hand panel). The velocity dispersion of the dark matter has a decreasing trend, starting from ~ 180 km s^{-1} in the center and arriving to ~ 60 km s^{-1} at 250 kpc. In the bulge σ is increasing to a maximum of ~ 125 km s^{-1} at 3 kpc and then remains almost constant in the first 10 kpc. This is consistent with the observations of the bulge velocity dispersion in the Milky Way (Valenti et al., 2018).
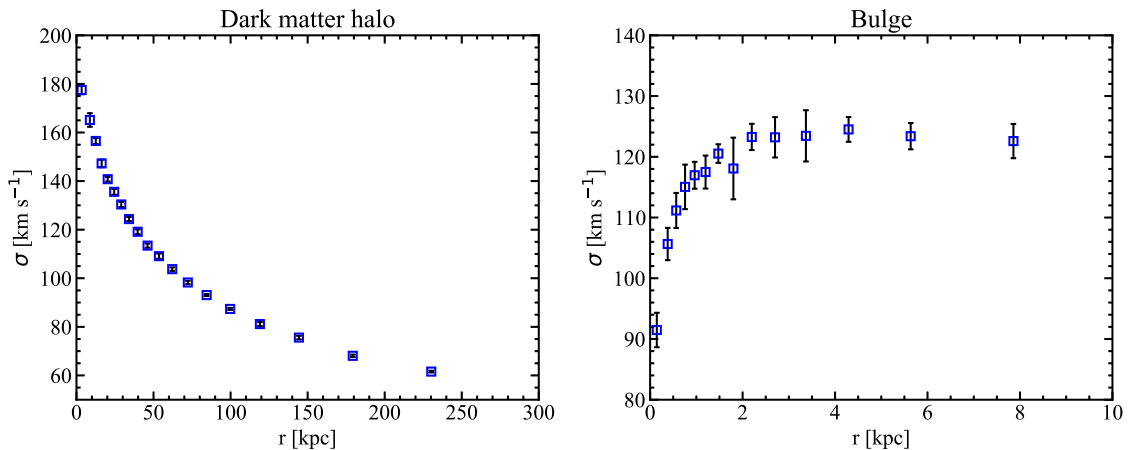
Figure 3.6: Velocity dispersion as a function of radius (blue points with error-bars) for the dark matter halo (left-hand panel) and for the bulge (right-hand panel).

Vertical stellar disc velocity dispersion

Also, it is possible to check the vertical velocity dispersion of the stellar disc under the thin and infinite disc approximation. Close to the plane of the disc $|z| \approx 0$ the stellar disc is dominating the gravitational potential (the gaseous disc is negligible in mass) and therefore it drives the dynamics of the stars. The vertical equilibrium of the stars in the total potential is set by the vertical Jeans equation

$$\frac{\partial(\rho_\star \sigma_z^2)}{\partial z} + \rho_\star \frac{\partial \Phi}{\partial z} = 0, \tag{3.6.17}$$

where $\rho_\star$ is the stellar density, Φ is the total gravitational potential, $\sigma_z = \sigma_R$ is the vertical velocity dispersion. From equation (3.6.17) it is possible to derive the vertical velocity dispersion σ_z. Under these assumptions the dominant component of the potential near the disc is the z-component, therefore the Poisson's equation can be written as

$$\frac{\partial^2 \Phi}{\partial z^2} = -4\pi G \rho(z), \tag{3.6.18}$$

from which we derive

$$\frac{\partial \Phi}{\partial z} = -4\pi G \int_0^z \rho(z) \ \mathrm{d}z = -2\pi G \Sigma_\star \tanh\left(\frac{z}{z_0}\right). \tag{3.6.19}$$

Solving equation (3.6.18) with (3.6.19) we find (Van Der Kruit, 1988)

$$\sigma_z^2 = -\frac{1}{\rho} \int_0^\infty \rho \frac{\partial \Phi}{\partial z} \ \mathrm{d}z = 2\pi G \Sigma_\star z_0. \tag{3.6.20}$$

In Figure 3.7 we show the vertical velocity dispersion σ_z, for the star particles in the stellar disc as a function of the cylindrical radius R computed in the same way as the dark matter and bulge velocity dispersions (equation 3.6.16). The analytical profile (red dashed line) has been calculated with equation (3.6.20). The deviation in the central parts is caused by the presence of the bulge that dominates the gravitational potential in the inner regions, an effect that is not captured by our simplified analytic treatment. Also in the outer parts the approximation of thin infinite disc is not valid anymore, since the dark matter halo starts to dominate the total potential. As we can see σ_z is decreasing with radius. Indeed, the stellar density will decline exponentially moving to the outer parts of the disc and, consequently, this component will exert a lower gravitational attraction. Since the disc scale height is held constant in the ICs, this results in a decrease of the vertical velocity dispersion for increasing galactocentric distances (as it is also evident from equation 3.6.20).
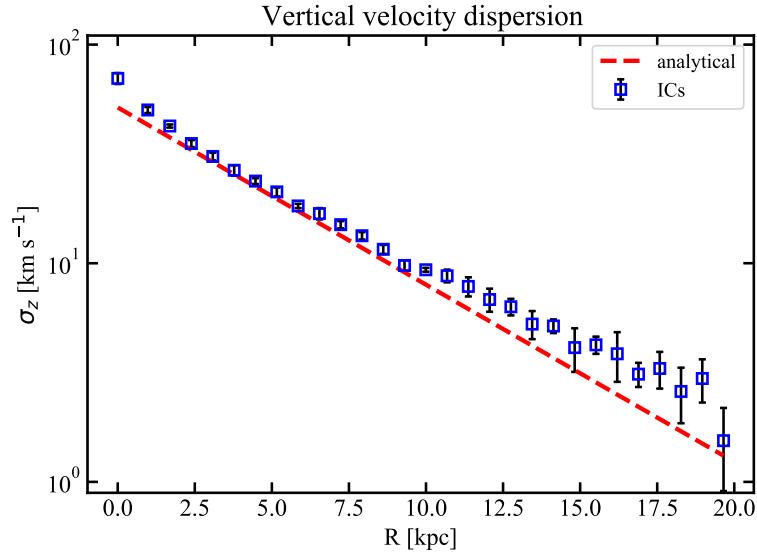
Figure 3.7: Vertical velocity dispersion as a function of radius (blue points with error-bars) for the stellar disc; the red dashed line represents the approximate analytical solution derived from the vertical Jeans equation. The points are not in agreement with the analytical profile in the inner (because of the bulge presence) and outer parts (because the thin disc approximation is not valid).

To make a consistency check we compare the vertical velocity dispersion profile in Figure 3.7 with the observations for the vertical velocity dispersion of old star in the solar neighbourhood (Binney and Tremaine, 2011)

$$\sigma_z(R_\odot) = (19 \pm 2) \text{ km s}^{-1}, \tag{3.6.21}$$

obtaining a good agreement at $R_\odot$.

3.6.4 Temperature and metallicity profiles

Here we show the temperature and metallicity profiles for the gas, these are fundamental properties to model in order to obtain a more realistic time evolution of the galaxy. In Figure 3.8 we show the temperature profiles of the ICs for the gaseous disc (left panel) and the hot corona (right panel). As expected the temperature in the disc is constant at a value of 10^4 K, while the coronal gas temperature follows the trend of the dark matter halo velocity dispersion profile, reaching its peak in the center ($\sim 2.5 \times 10^6$ K). This temperature is around the virial temperature of the dark matter halo. In Figure 3.9 we show, as a consistency check, the metallicity profiles for the gaseous disc and the corona. As expected, the gaseous disc has a metallicity $Z_d = 1\ Z_\odot$ and the corona has a metallicity $Z_{cor} = 0.1\ Z_\odot$.
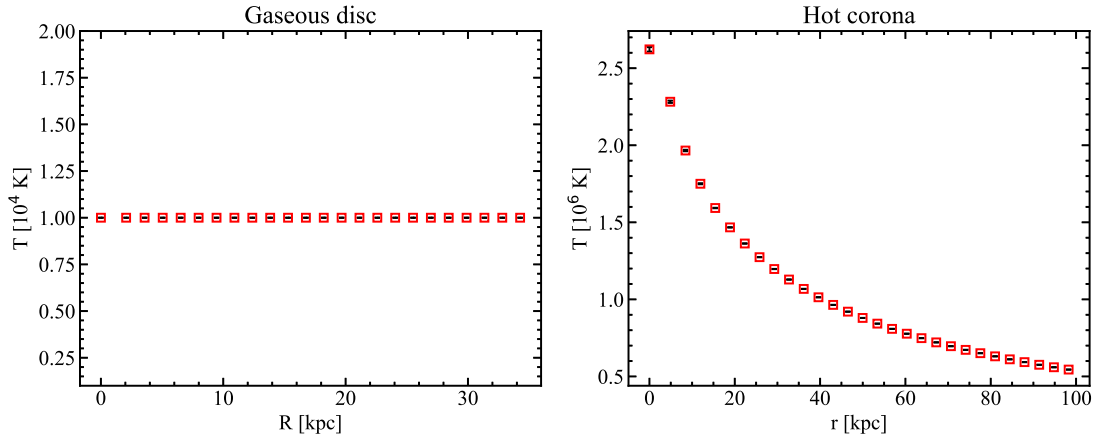
Figure 3.8: Temperature profiles of the gaseous disc (left panel) and the hot corona (right panel).
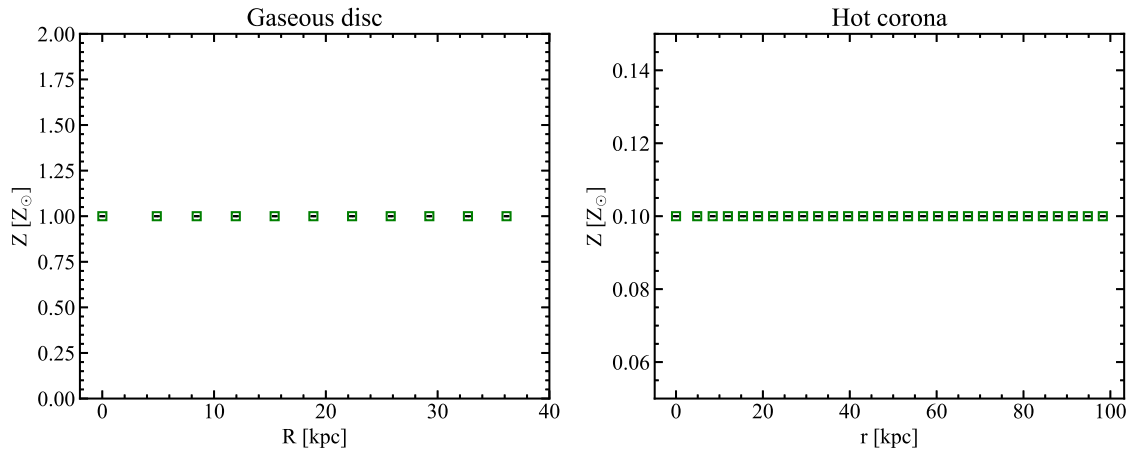
Figure 3.9: Metallicity profiles of the gaseous disc (left-hand panel) and the hot corona (right-hand panel).

Simulations results

<div style="text-align: right">4</div>

In this Chapter we present the results obtained from the numerical simulations performed with AREPO. First, we run adiabatic simulations, i.e. without the presence of the dissipation processes implemented in the *SMUGGLE* model (see Section 2.4), to ensure that the different components of the galaxy are in equilibrium; the results are shown in Section 4.1. Afterwards, we carried out a series of simulations using the *SMUGGLE* model; we present these results in Section 4.2.

In order to create an observationally-motivated hot corona we used the few observational constraints available for the mass of the Milky Way corona. In particular, we explored a range of masses relying on indirect estimates (see Chapter 1) based on pulsar rotation measures and ram-pressure stripping of dwarf spheroidal galaxies and the Large Magellanic Cloud around the Milky Way (Grcevich and Putman, 2009; Gatto et al., 2013; Salem et al., 2015; Anderson and Bregman, 2010). We performed simulations for five coronal masses: four adiabatic simulations (COR_A1, COR_A2, COR_A3, COR_A4) and three simulations with the *SMUGGLE* model (COR_S1, COR_S2, COR_S3). The masses of the corona used in these simulations are listed in Table 4.1, while the corresponding density profiles are shown in Figure 4.1: the red dashed lines represent the corona of the COR_S1 and COR_S2 simulations, the blue dashed lines COR_A1 and COR_A2, and the black dashed line COR_S3. As we can see from Figure 4.1 all the chosen masses are in agreement with the observational points, except for COR_S3, that has been chosen to represent a setup with an almost negligible coronal mass.

Table 4.1: Mass of the corona chosen for the adiabatic simulations (first row) and the simulations with *SMUGGLE* (second row).

adiabatic	COR_A1	COR_A2	COR_A3	COR_A4	-
SMUGGLE	-	-	COR_S1	COR_S2	COR_S3
$M_{\mathrm{cor}}(r < r_{\mathrm{vir}}) \, [M_\odot]$	1.1×10^{11}	3.4×10^{10}	1.38×10^{10}	6.8×10^9	6.8×10^8
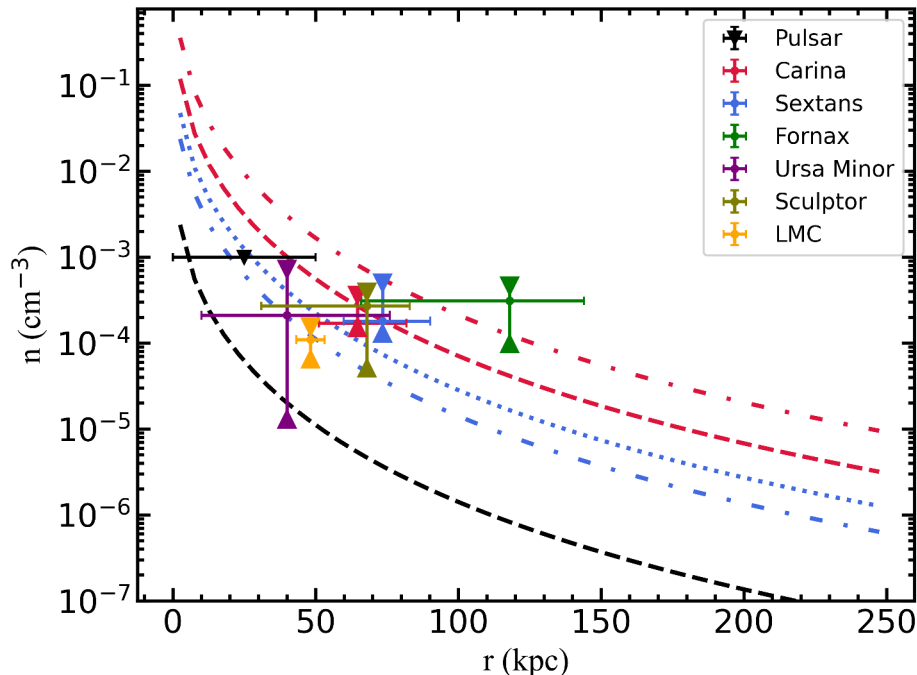
Figure 4.1: Hot corona number density profiles compared with several observational constraints: ram-pressure stripping from the dwarf spheroidal galaxies Fornax, Ursa Minor and Sculptor (Grcevich and Putman 2009), Carina and Sextans (Gatto et al. 2013) and the Large Magellanic Cloud (Salem et al. 2015); Pulsar rotation measures from Anderson and Bregman (2010). The dashed and the dash-dotted red lines represent respectively the models of the corona with $M(r < r_{\mathrm{vir}}) = 1.1 \times 10^{11} \mathrm{M}_\odot$ (COR_A1) and $M(r < r_{\mathrm{vir}}) = 3.4 \times 10^{10} \mathrm{M}_\odot$ (COR_A2) whereas the blue lines depict the ICs with $M(r < r_{\mathrm{vir}}) = 1.38 \times 10^{10} \mathrm{M}_\odot$ (COR_S1) and $M(r < r_{\mathrm{vir}}) = 6.8 \times 10^{9} \mathrm{M}_\odot$ (COR_S2) and the black dashed line shows a coronal model with $M(r < r_{\mathrm{vir}}) = 6.8 \times 10^{8} \mathrm{M}_\odot$ (COR_S3).

4.1 Adiabatic simulations

In this Section we present the numerical setup and the results of the adiabatic simulations of the Milky Way-like galaxies. By adiabatic simulation we mean a simulation in which the galaxy evolves with hydrodynamics and gravity only, without the presence of dissipation processes (as star formation, cooling, heating and stellar feedback). The simulations are carried out with the moving-mesh code AREPO (described in detail in Section 2.3) and the ICs have been created by following the procedure described in Chapter 3. The system is enclosed within a box with edges ≈ 857 kpc long. The resolution level used in the simulations has been shown in Table 3.3. The galaxy parameters are the ones listed in Table 3.2 and used in Section 3.6, except for the mass of the hot corona that is changed in each simulation to study its

stability. In particular, we performed four simulations with different coronal masses: COR_A1, COR_A2, COR_A3, COR_A4, listed in Table 4.1. The system is evolved in isolation for 2 Gyr. In Section 3.6 we have seen that the ICs are in agreement with the analytical profiles, now we carry out these different simulations to observe if an equilibrium is actually present and if the configuration remains stable during its evolution.
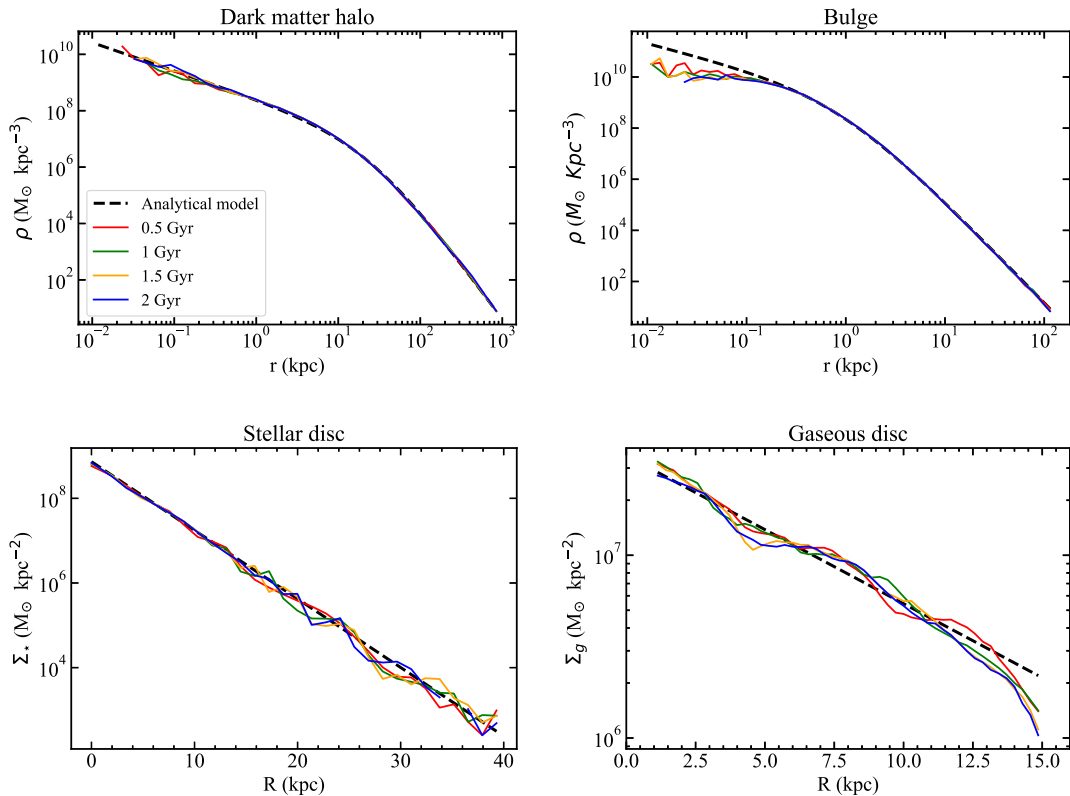
Figure 4.2: Evolution of density profiles in the COR_A2 simulation. The panels represent the dark matter halo (top left panel), bulge (top right panel), stellar disc (bottom left panel) and gaseous disc (bottom right panel). The black dashed line shows the analytical profiles and the coloured lines represent the density profiles at different times, as indicated in the legend.

We obtained density profiles for the bulge, the dark matter halo, the stellar disc and the gaseous disc (shown in Figure 4.2) at four different times, $t = 0.5, 1, 1.5, 2$ Gyr, for the COR_A2 simulation. Figure 4.2 shows how these profiles remain almost unchanged in each snapshot, following the analytical profile imposed in the ICs. The density profiles have been computed with the same method described in Section 3.6.1. However, the accurate determination of the center of the system
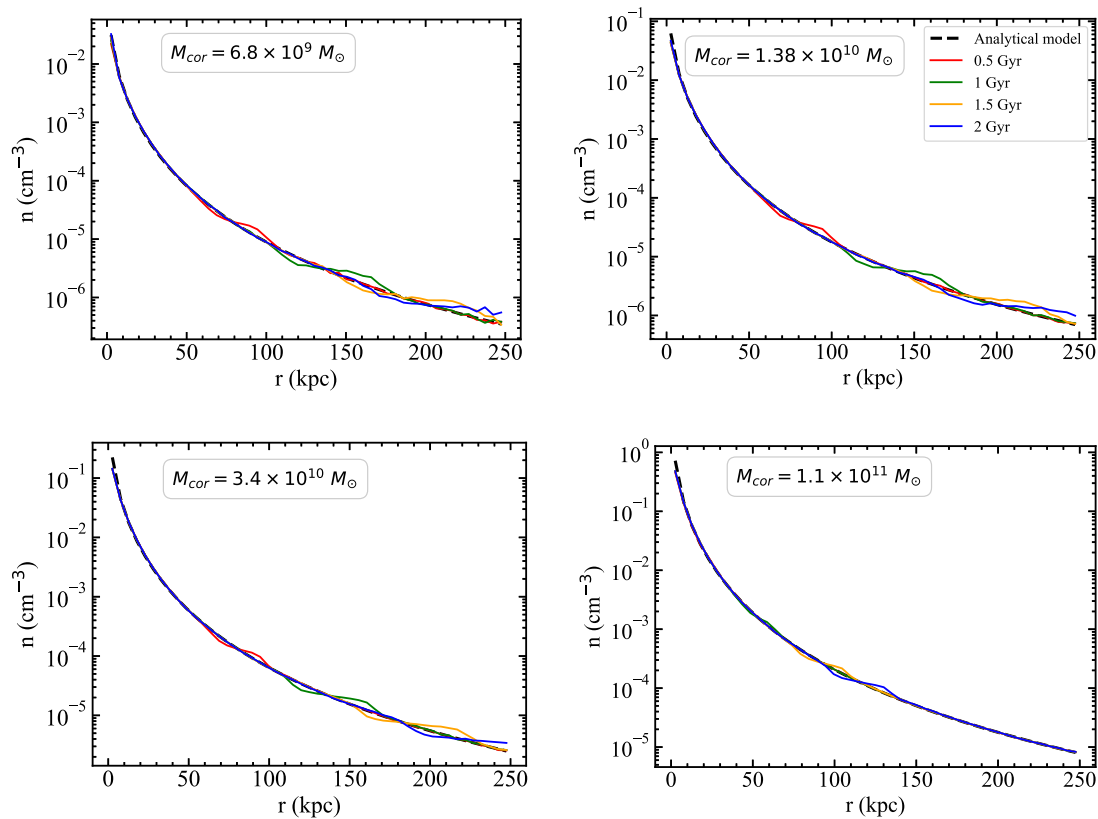
Figure 4.3: Number density profiles adiabatic evolution as a function of the galactocentric distance for the simulations COR_A4 (top left panel), COR_A3 (top right panel), COR_A2 (bottom left panel) and COR_A1 (bottom right panel). The black dashed line shows the analytical profiles and the coloured lines represent, respectively, the density profiles at different times, as indicated in the legend.

requires some care. AREPO uses a Tree method to compute the gravitational potential (see Section 2.3), this method does not conserve the momentum at machine precision and we may expect a shift of the center of mass of the galaxy from one snapshot to another. This can cause an artificial flattening in the inner parts of the profiles (< 1 kpc). We corrected the center of mass shift using the *shrinking sphere method* (Power et al., 2003), an iterative method to find the center of mass of the system. First, we computed the (x,y,z)-position of the center of mass of a given spherical component (dark matter halo, bulge, corona) as

$$x_{\text{cm}} = \frac{\sum_i m_i x_i}{\sum_i m_i}, \tag{4.1.1}$$

from the particles inside a sphere with a radius of 100 kpc. Then, the center of the sphere is moved to the newly calculated center of mass and its radius is decreased by 2.5%. This computation is repeated until the radius of the sphere is 0.1 kpc. The coordinates of the different particles are corrected by shifting them with the center of mass calculated for each different snapshot. The inner density (< 1 kpc) of the bulge slightly differs from the analytical profile, however this is a numerical artefact due to the adopted values of the gravitational softening of the bulge particles (0.09 kpc). Since the adopted softenings are quoted as Plummer equivalent softenings, at scales below $\approx 2.8\varepsilon$ we cannot fully trust the obtained density profile. The lower right panel shows the density profile of the gaseous disc, after the start of the simulation the gas particles that belong to the disc and to the corona cannot be easily identified anymore due to the mass exchange that the two gas components can undergo. In order to separate the disc and the corona particles and obtain plots of a single component, we employed a selection in temperature T and height above and below the disc plane z. In particular, we labeled as disc particles all those particles with $T < 5 \times 10^5$ K and $|z| < 2.5$ kpc. All the other gas cells have been attributed to the corona.

In Figure 4.3 we show the time evolution of the hot corona density profile for the four different masses used in the simulations. In particular they are computed at 0.5 Gyr (red), 1 Gyr (green), 1.5 Gyr (orange) and 2 Gyr (blue), and are compared with the analytical profile (black dashed line). These plots give an evidence of the stability of the corona in these adiabatic simulations. After 2 Gyr the coronal gas still reasonably follows the initial profile. The *shrinking sphere method* was used also in this case to correct for the center of mass position.

In Figure 4.4 (top row) we show the adiabatic evolution of the azimuthal velocity for the stellar (left-hand panel) and gaseous (right-hand panel) discs for the COR_A2 simulation. In both cases the kinematics structure is approximately maintained over 2 Gyr. The selection problems that affected the gaseous disc density profile are present also here, for $R > 15$ kpc a large fraction of corona particles are selected, causing an underestimation of the azimuthal velocity, but this could also be caused by an exchange of moment between the disc and the corona. In Figure 4.4 (bottom row) we show the adiabatic evolution of the velocity dispersion for the dark matter halo (left-hand panel) and the bulge (right-hand panel) for the COR_A2 simulation. The profiles remain stable in all the adiabatic simulations also in this case.

In Figure 4.5 we show the gas column density in face-on (upper panels) and edge-on (lower panels) projections for $t = 0.45$, 0.9 and 1.35 Gyr. Each panel is 50×50
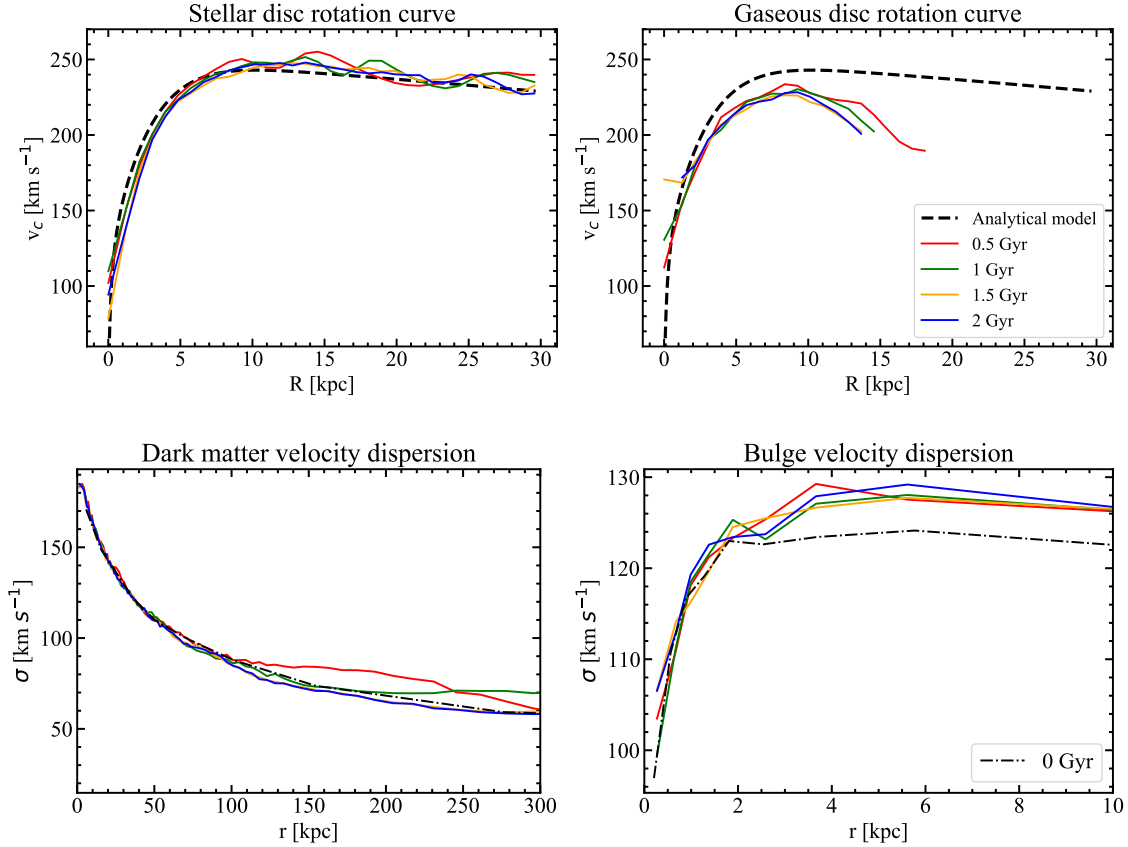
Figure 4.4: Rotation curve (top row) adiabatic evolution of stellar (left-hand panel) and gaseous (right-hand panel) discs for the COR_A2 simulation, the black dashed lines represent the analytical profiles; velocity dispersion (bottom row) adiabatic evolution of dark matter halo (left-hand panel) and bulge (right-hand panel) for the COR_A2 simulation, the black dash-dotted lines represent the profiles at t=0 Gyr. The coloured lines represent respectively the profiles at different times, as indicated in the legend.
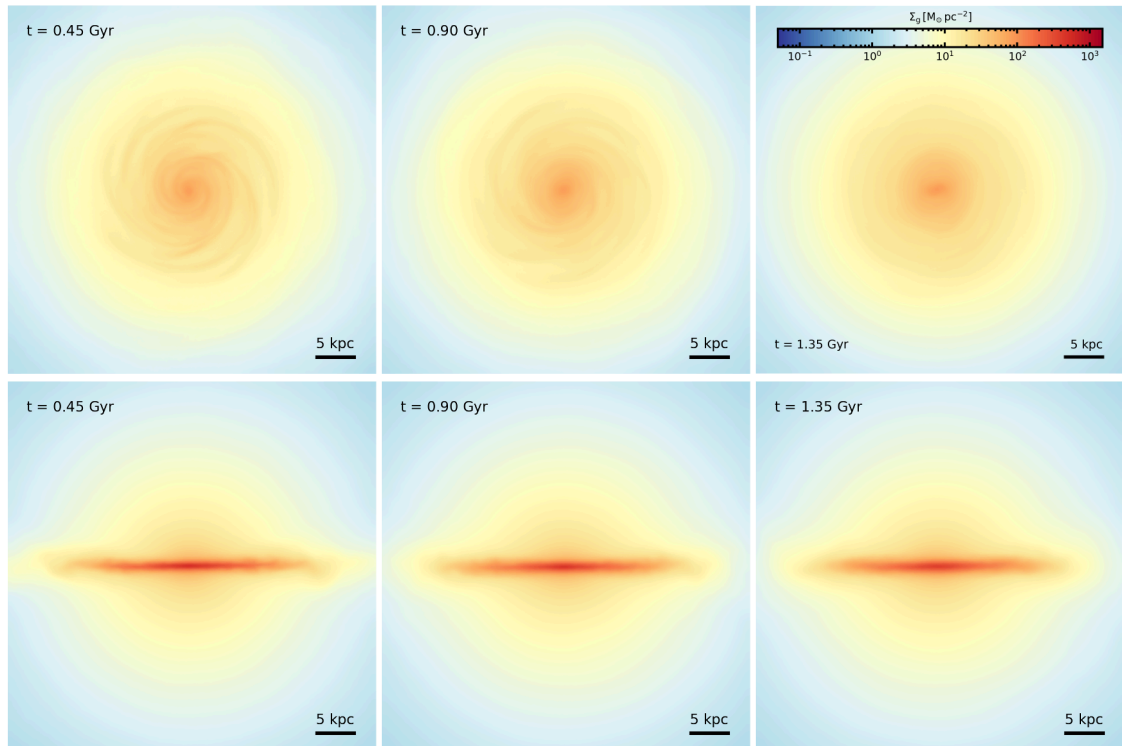
Figure 4.5: Face-on (top row) and edge-on (bottom row) gas column density maps of the Milky-Way like galaxy computed in the COR_A2 simulation at $t = 0.45$ Gyr (left panels), $t = 0.9$ Gyr (middle panels), $t = 1.35$ Gyr (right panels). We can visually appreciate the stability present in the different galaxy components, in particular in the hot corona, that can be seen in the edge-on projections.

kpc wide and is comprised of 1024×1024 pixels that give a resolution of ~ 50 pc. These projections visually confirm the dynamical stability of the simulated galaxy model, with a configuration that remains almost unchanged for a time span of 2 Gyr.

4.2 Simulations with the *SMUGGLE* model

The next step is to simulate an isolated galaxy using the *SMUGGLE* model, in order to compute a realistic evolution of the galaxy that includes dissipative processes, such as star formation, cooling and heating of the gas, and stellar feedback (see Section 2.4). We performed three simulations: COR_S1, COR_S2 and COR_S3, with different coronal masses, reported in Table 4.1, using the same parameters mentioned in Section 4.1. We analyzed the simulations focusing on the interplay between the disc and the corona and its influence on the star formation of the galaxy. In particular we show: (i) the star formation rate and its connection with the circulation of gas, studying outflow and inflow rates of gas (Subsection 4.2.1), (ii) the time evolution of the different gas phases (cold, warm and hot) and (iii) the role of the metallicity (Subsection 4.2.2).

4.2.1 Star formation-outflow/inflow connection

As mentioned in Chapter 1, the formation of stars is a fundamental process to understand the evolutionary state of galaxies; in star-forming galaxies like the Milky Way a star formation rate (SFR) of $\sim 1-2$ $M_\odot$ yr^{-1} is measured, therefore, we expect our simulations to reproduce this quantity in the presence of the corona. Figure 4.6 shows the SFR of the galaxy as a function of time for the three simulations COR_S1, COR_S2 and COR_S3. All three simulations present a large bump in the SFR for times $t < 0.5$ Gyr. We note that the massive the corona the higher the bump. This bump is due to the rapid collapse of the corona in the central regions, caused by a configuration of non-equilibrium due to the presence of an efficient radiative cooling from the beginning of the simulation, which was not present (by definition) in the adiabatic simulations. Adiabatically, we set the corona in hydrostatic equilibrium, but the activation of the cooling processes causes a significant deviation from it. This causes the corona to lose pressure support in the central regions and accrete (too) rapidly onto the disc. This problem is due to the numerical implementation of the corona, which is already in place at the beginning of the simulations. A realistic

simulation would gradually form the hot corona in time following the processes mentioned in Chapter 1. Some solutions to this problem could be the addition of rotation to the coronal gas or the implementation of a different coronal density profile, as we will be briefly discussing in Chapter 5.

After this first "collapse" phase, that keeps the SFR at a relatively high level for ~ 0.5 Gyr, the SFR stabilizes thanks to the self-regulation between star formation and stellar feedback achieved by the *SMUGGLE* model. It is worth noting that there is still a strict connection between the SFR and the mass of the corona: the more massive the corona, the higher the star formation rate level at late times. This behaviour is caused by the accretion of the coronal gas onto the disc of the galaxy. A higher coronal gas accretion rate induces higher densities of the gas in the disc and a larger star formation rate than in a no accretion scenario. In the COR_S1 simulation the SFR starts from $\sim 5 - 6$ $M_\odot$ yr^{-1} after the bump and it decreases to ~ 2 $M_\odot$ yr^{-1} at 2 Gyr.
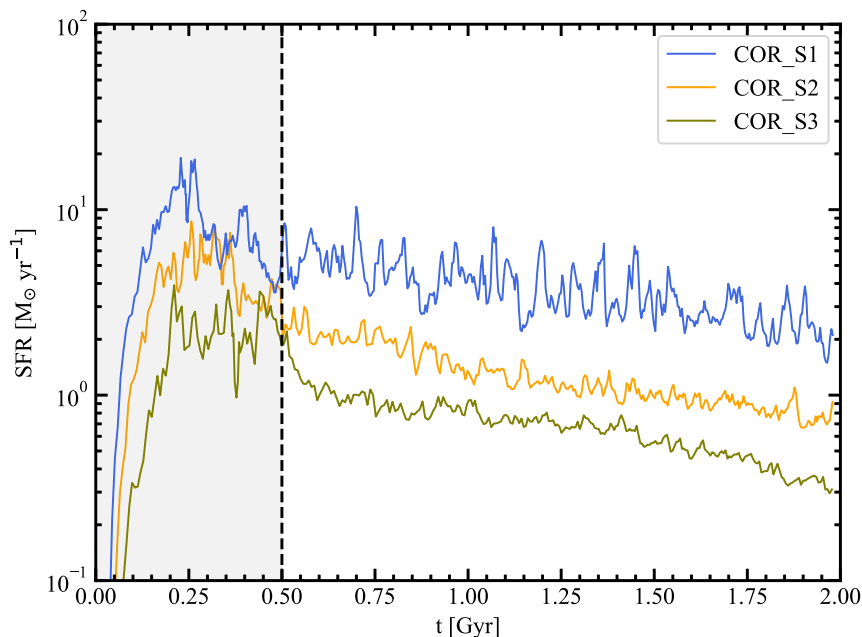
Figure 4.6: SFR of the galaxy as a function of time for the three simulations performed: COR_S1 (blue), COR_S2 (yellow) and COR_S3 (green). We note the presence of a SFR bump in the first 0.5 Gyr (highlighted by the grey band) due to an initial collapse of the corona caused by the activation of the radiative cooling processes. In general, in all the three simulations, the higher the coronal mass, the higher the SFR, pointing out a link between the presence of this component and the level of the star formation.

The same decreasing trend is present in the COR_S2 and in the COR_S3 simula-

tions. In COR_S2 the SFR remains over 1 $M_\odot$ yr^{-1} (starting from ~ 2 $M_\odot$ yr^{-1} after the bump) until 1.7 Gyr (in good agreement with the SFR observed nowadays in the Milky Way), when it continues decreasing to ~ 0.7 $M_\odot$ yr^{-1}. COR_S3 features a SFR after the bump that goes from ~ 1 $M_\odot$ yr^{-1} at 0.5 Gyr to ~ 0.4 $M_\odot$ yr^{-1} at 2 Gyr. It is worth noting the presence of a periodicity in the SFR (visible in particular in the COR_S1 simulation), this 'up-and-down' trend is linked to the self-regulation between the formation of stars and the stellar feedback that it causes. On the one hand, the periodic activation of the stellar feedback temporarily reduces the star formation injecting energy and momentum in the ISM, heating the gas and ejecting it from the disc. On the other hand, the periodic (re-)accretion of gas onto the disc can support fresh star formation.

We show now the face-on and edge-on surface density maps of the COR_S1, COR_S2 and COR_S3 simulations at different times, as indicated in each panel. From the face-on projection of COR_S1 (Figure 4.7) it is evident the gaseous disc structure of the galaxy. As the simulation starts, the first stars begin to form, generating radiative feedback and stellar winds that are followed by the supernova explosions: the formation of low-density cavities (surface densities $< 1 M_\odot$ pc^{-2}) caused by these phenomena is evident. These cavities, filled with hot gas, can extend over the plane of the disc and are responsible for the production of outflows. Along the spiral arms of the galaxy, on the edges of the generated cavities, are present high-density gas filaments, where most of the star formation takes place. The same phenomenon happens for COR_S2 (Figure 4.7) and COR_S3 (Figure 4.8). Looking at the projections, we note that the size of the disc increases as the mass of the corona decreases. This could be caused by a redistribution of the angular momentum from the disc to the corona caused by the gas circulation (that is more intense in COR_S1), but this speculation requires further investigations.

Focusing on the edge-on projections (Figures 4.10, 4.11 and 4.12), in a first phase, as mentioned, the hot corona collapses rapidly onto the disc (see top left panel of Figure 4.10), and this causes the initial bump in the SFR. Then the corona inflates again and continues its evolution. From the edge-on projections of the COR_S1 model of Figure 4.10 it can be appreciated the presence of outflows ejected from the disc. In this case the outflows can reach relatively large distances from the galaxy midplane (~ 10 kpc) and then fall back onto the disc. This is apparent in the 1.15 Gyr image where we can see the arc trajectory made by the galactic fountain. In Figure 4.11 we show the gas column density edge-on projections for COR_S2, here the coronal mass is smaller reaching lower densities in the last images (t=1.49, 1.55,

1.86 Gyr). Also, we note that the gaseous outflow are more sporadic and reach smaller heights ($\sim$ 5 kpc). A similar trend is visible in Figure 4.12, in the case of COR_S3, where the mass of the corona is almost negligible and no large scale outflows are present. A more detailed outflow/inflow analysis is made below.

We computed also edge-on projections of the density-weighted gas velocity perpendicular to the disc plane. In COR_S1 (Figure 4.13) we see the complex kinematic structure of the outflows of gas: these can have a velocity excess of 150 km s^{-1}. Also, particularly noticeable is the accretion of coronal gas that is strongest in the central regions, where its density is higher. In COR_S2 (Figure 4.14) and COR_S3 (Figure 4.15) only a few outflows are visible, reaching very small distances above and below the disc plane.
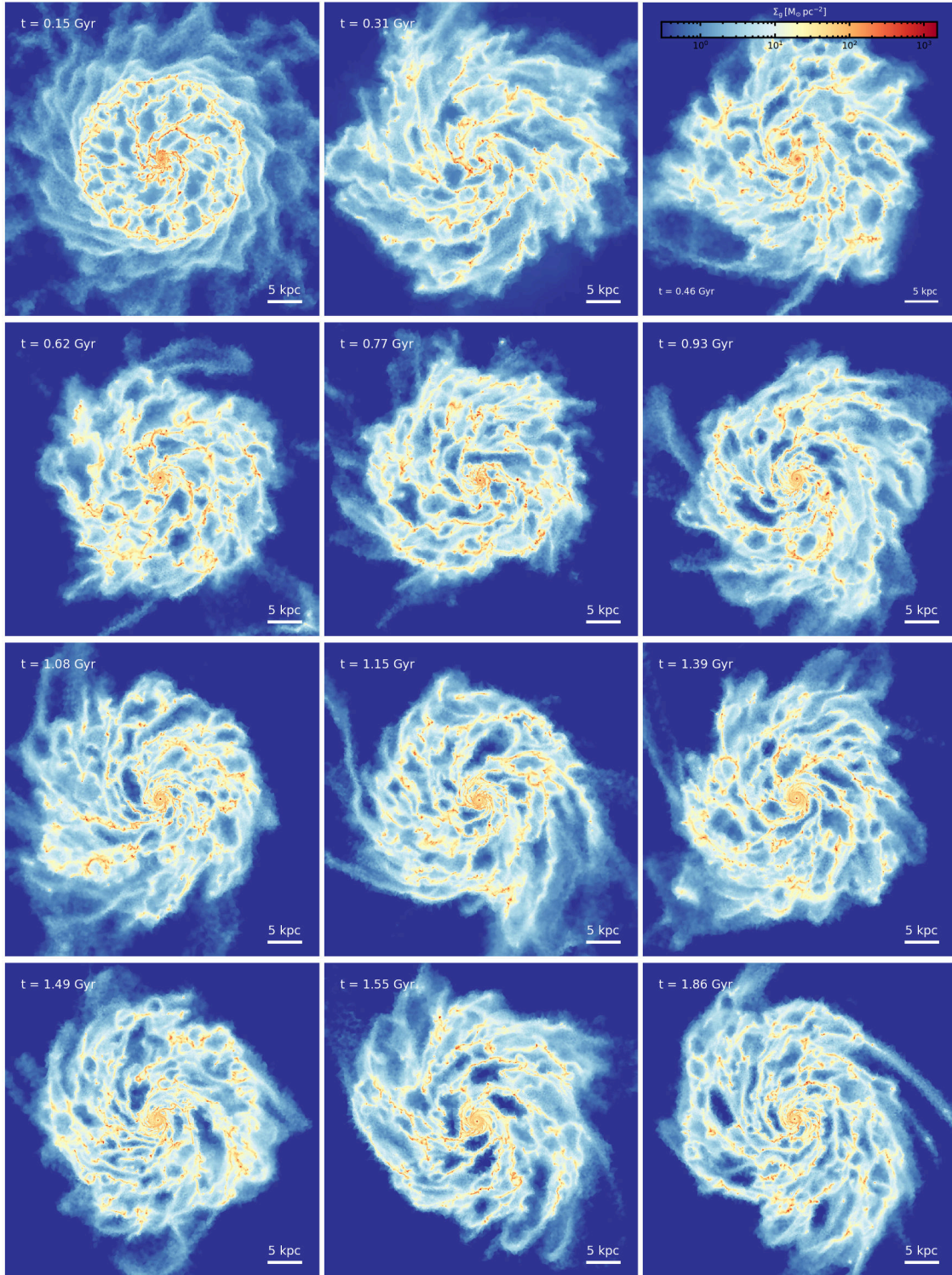
Figure 4.7: Gas column density in face-on projections of the COR_S1 simulation computed using the *SMUGGLE* model at the times indicated in each panel. Each panel is 50 kpc across and in projection depth with a total number of 1024 × 1024 pixels that give a resolution of ∼ 50 pc. Redder colors correspond to higher densities, as indicated in the colorbar. We can appreciate the presence of a complex ISM structure, with low density cavities produced by stellar feedback and high density filaments where the star formation takes place.

95
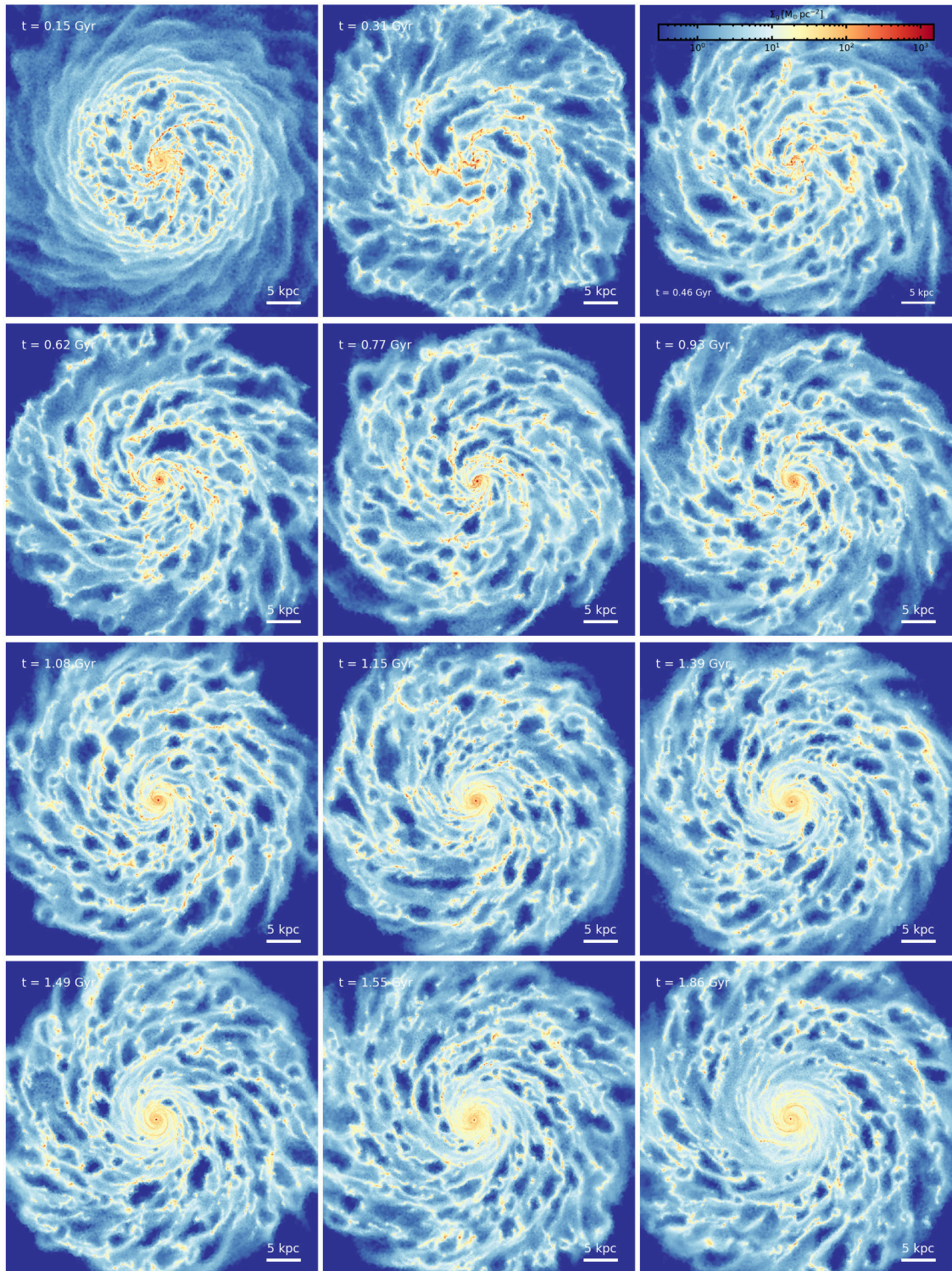
Figure 4.8: Same as Figure 4.7 but for the COR_S2 simulation.
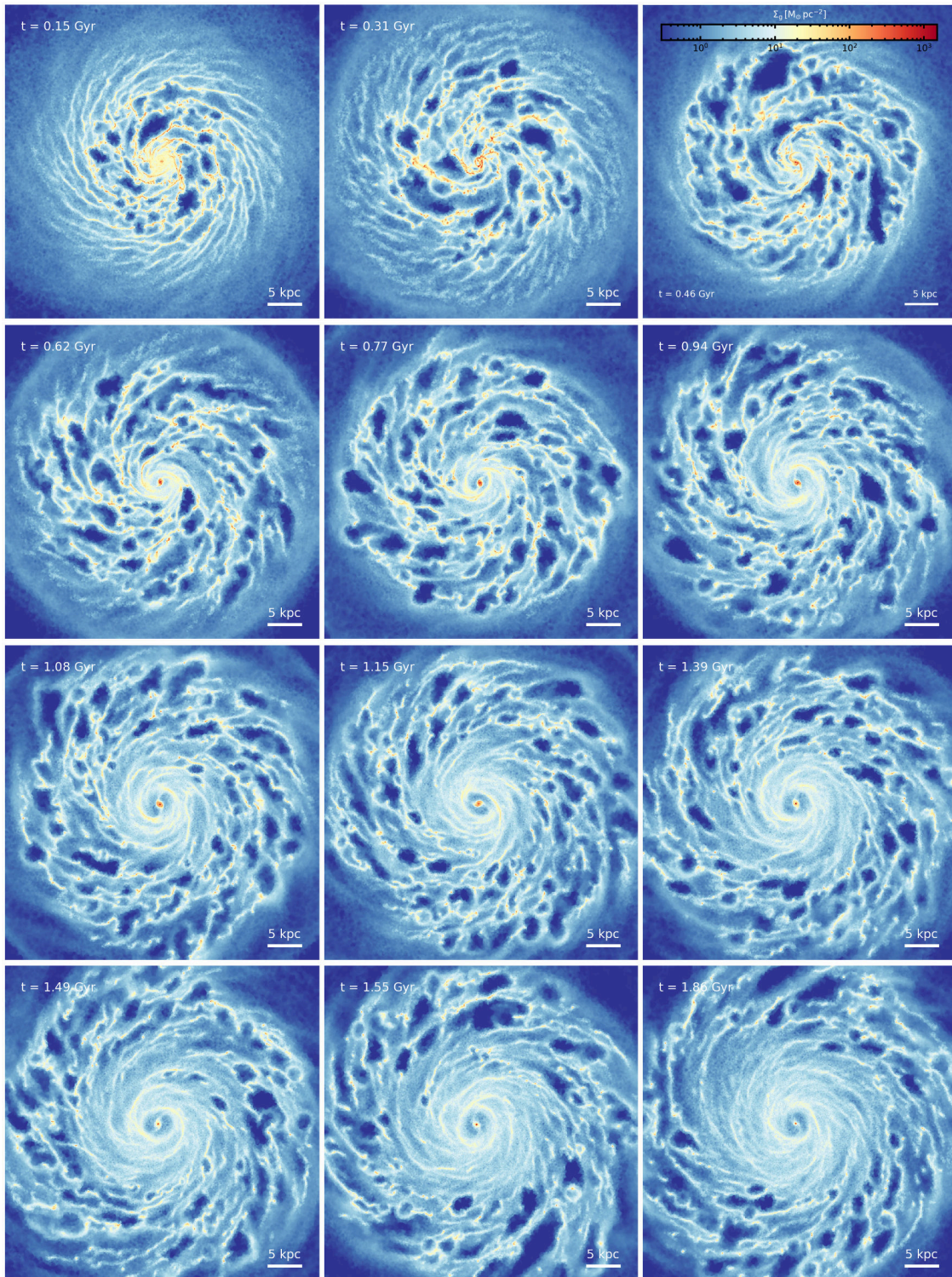
Figure 4.9: Same as Figure 4.7 but for the COR_S3 simulation.
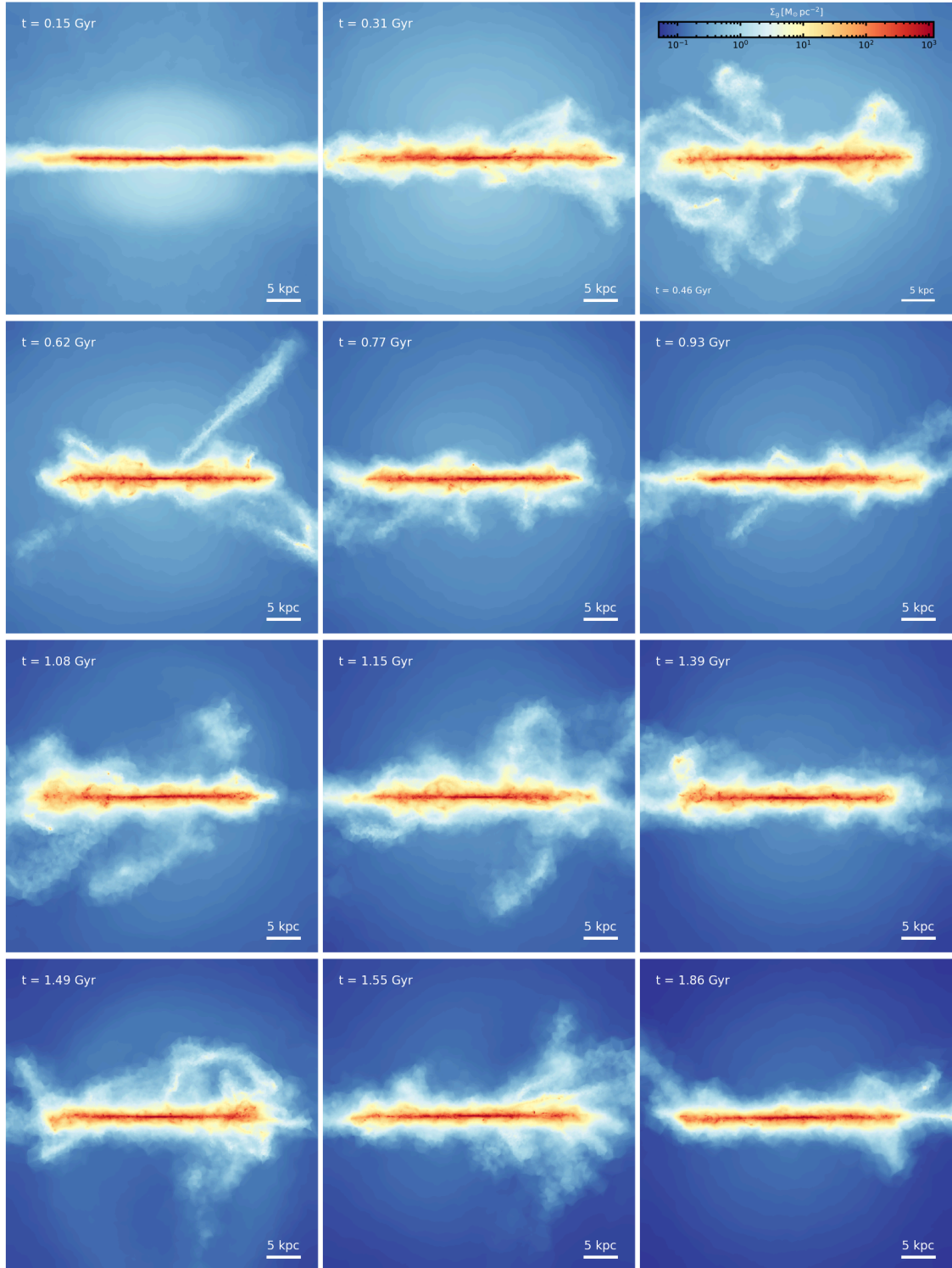
Figure 4.10: Gas column density in edge-on projections of the COR_S1 simulation computed using the *SMUGGLE* model at the times indicated in each panel. Each panel is 50 kpc across and in projection depth with the presence of a total number of 1024 × 1024 pixels that give a resolution of ∼ 50 pc. Redder colors correspond to higher densities, as indicated in the colorbar. We note the presence of galactic scale outflows caused by stellar feedback that travel through the hot corona.
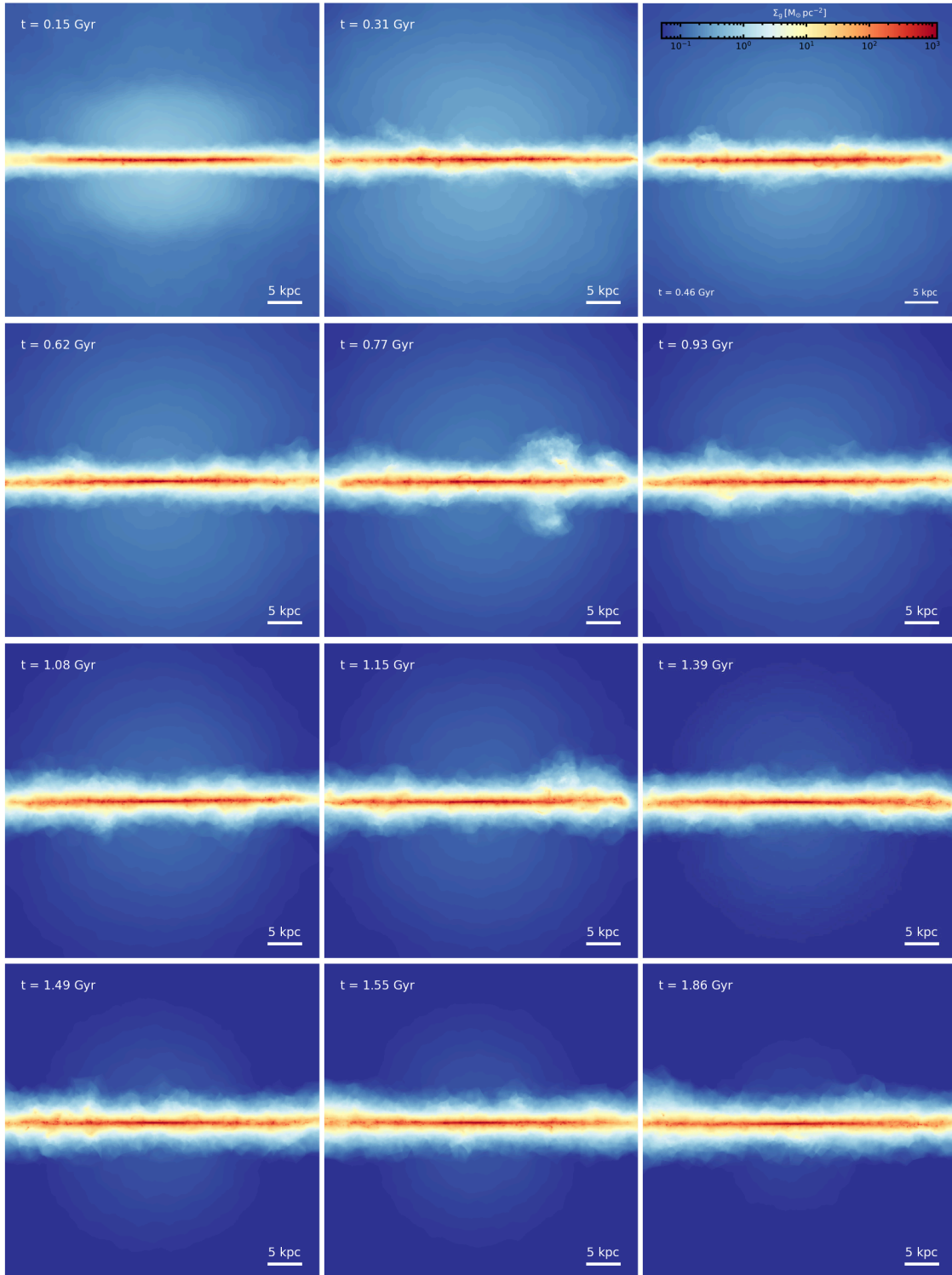
Figure 4.11: Same as Figure 4.10 but for the COR_S2 simulation.
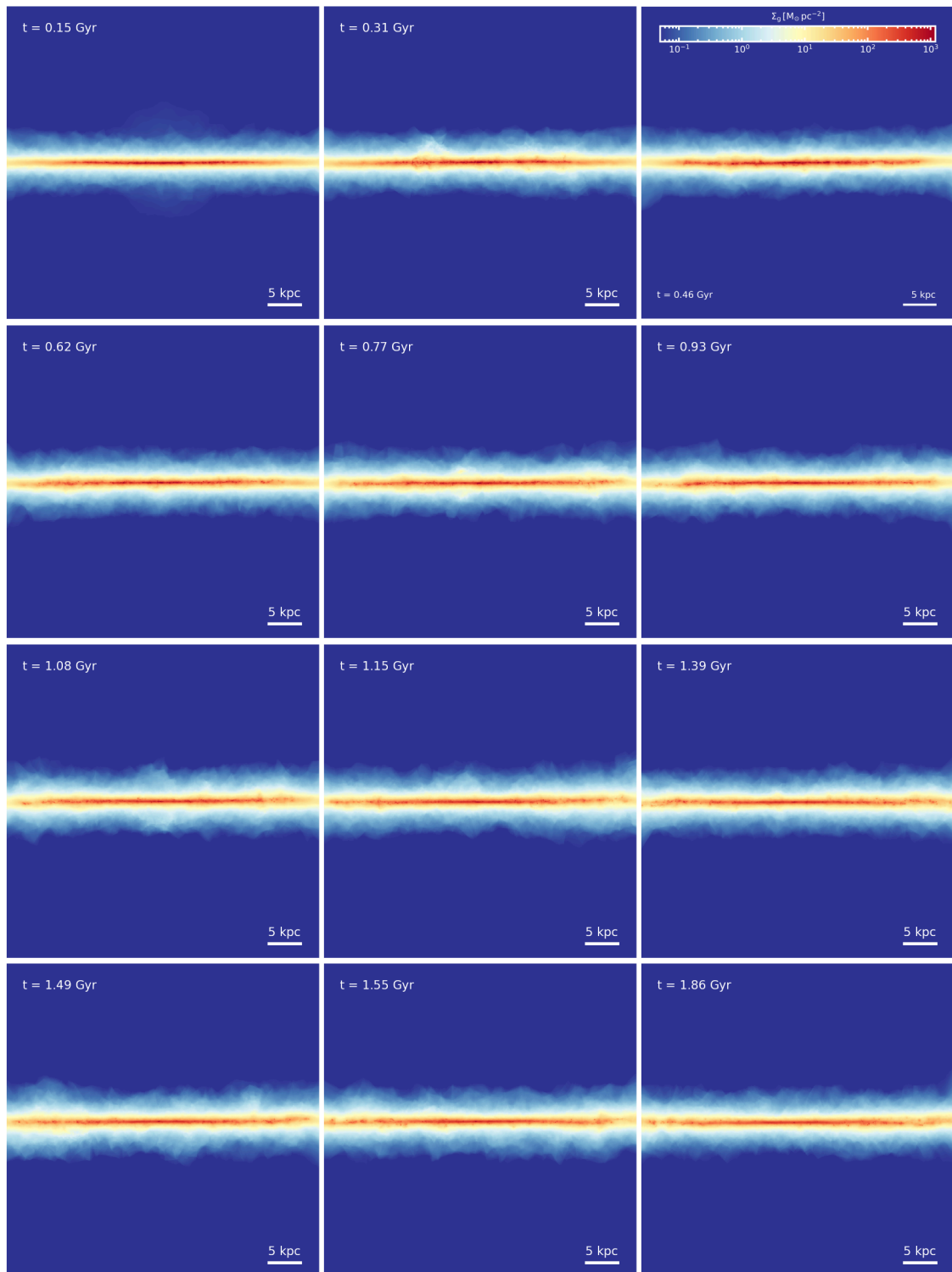
Figure 4.12: Same as Figure 4.10 but for the COR_S3 simulation.
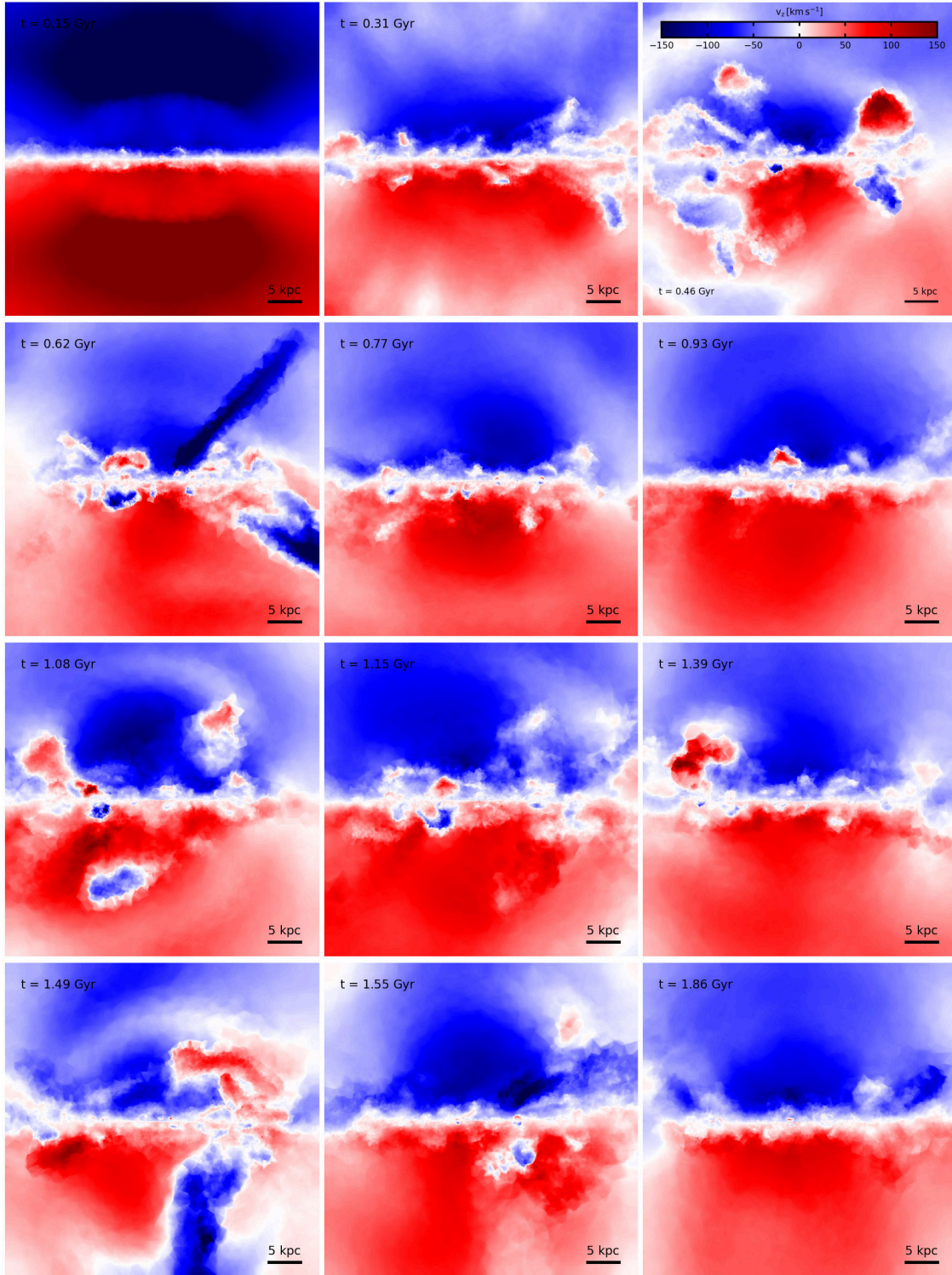
Figure 4.13: Density-weighted maps of the gas velocity perpendicular to the disc plane in edge-on projections of the COR_S1 simulation. Each panel is 50 kpc across and in projection depth with a total number of 1024 × 1024 pixels that give a resolution of ~ 50 pc. We can visually appreciate the kinematic structure of the outflows of gas ejected from the disc.

101
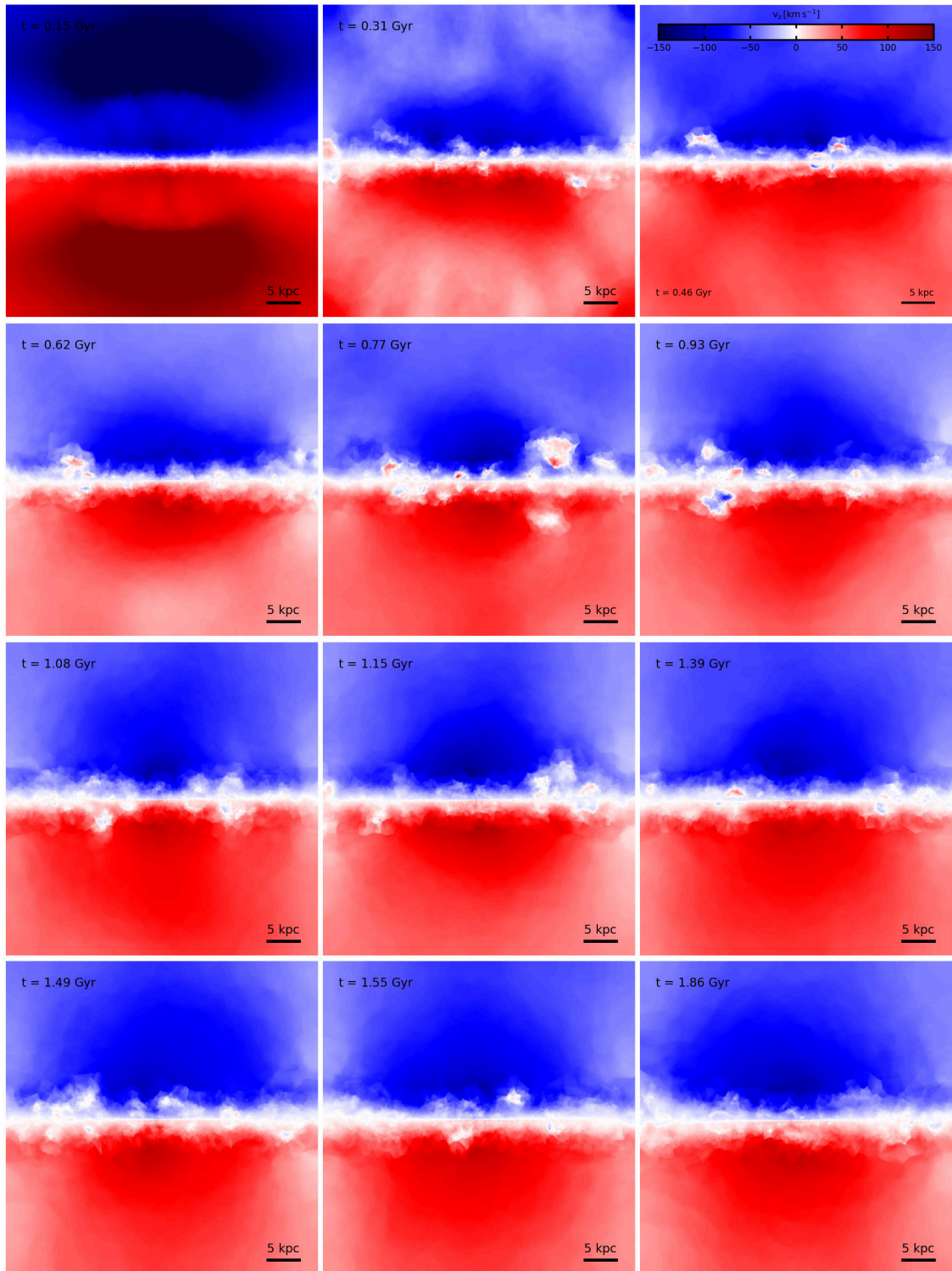
Figure 4.14: Same as Figure 4.13 but for the COR_S2 simulation.
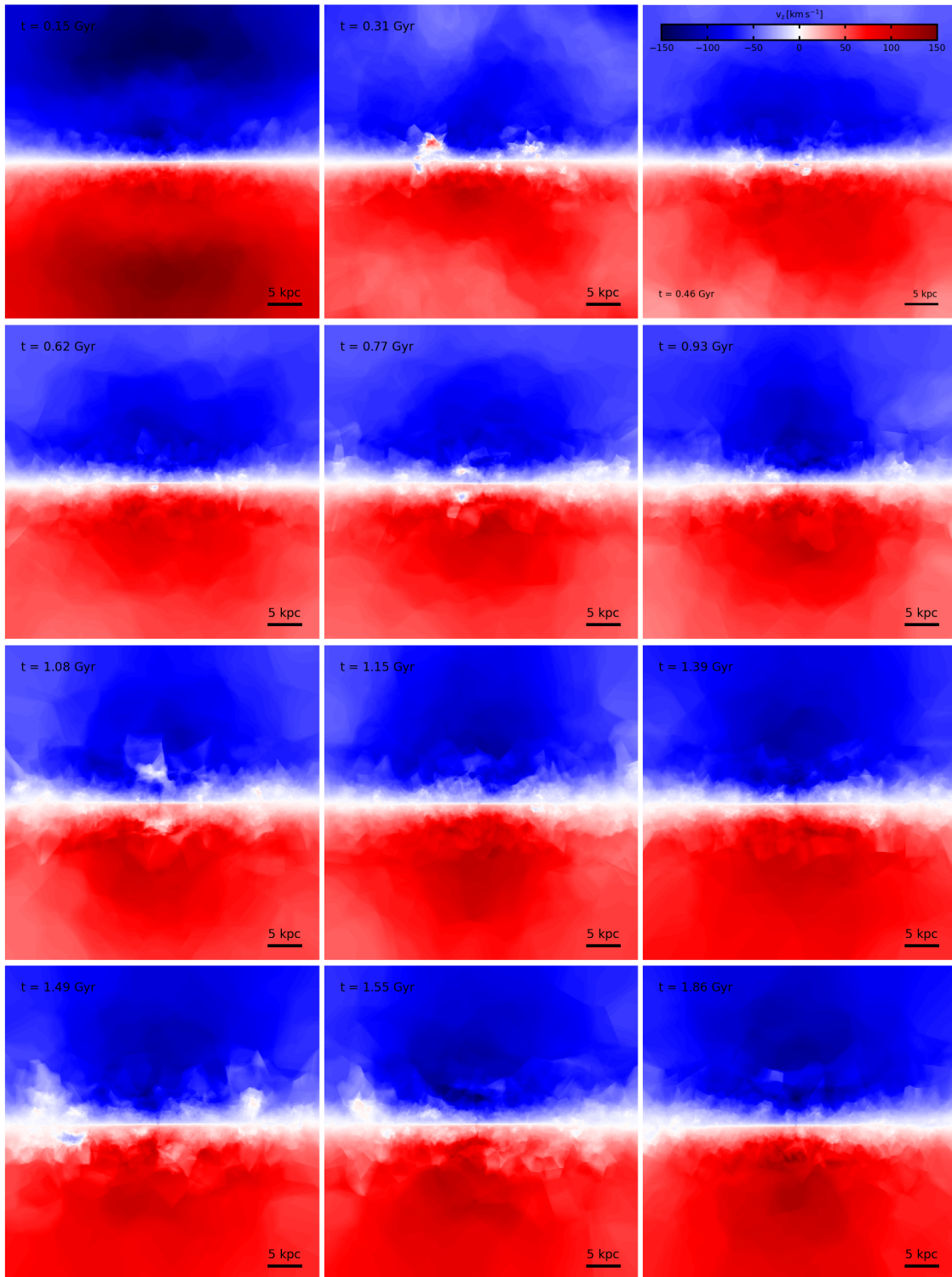
Figure 4.15: Same as Figure 4.13 but for the COR_S3 simulation.

Outflow and inflow rates

To analyze the relationship between star formation and the gas accreted/ejected onto/from the disc of the galaxy, we analyze the outflow and inflow rates of gas. We computed these rates as described in Marinacci et al. (2019). We took two slabs with a width $\Delta z = 0.3$ kpc starting at an height from the plane of the disc of ± 2 kpc and ± 5 kpc. Each gas particle i inside the slabs and with $R < 30$ kpc contributes to the outflow/inflow rate with

$$(\text{outflow/inflow})_i = \frac{v_{z,i} m_i}{\Delta z}, \qquad (4.2.1)$$

where $v_{z,i}$ is the vertical velocity and m_i is the gas particle mass. The outflow rate is computed summing the contributes of the particles that are moving away from the disc, i.e. particles with $v_z z > 0$; while the condition $v_z z < 0$ identifies the particles corresponding to an inflow. In Figures 4.16, 4.18 and 4.19 we show the outflow (red line) and the inflow (blue line) rate changing the distance of the slabs: 2 kpc and 5 kpc. The three dash-dotted lines represent the average values of the inflow rate (light blue), the SFR (grey) and the outflow rates (orange).

In Figure 4.16 the outflow and inflow rates for the COR_S1 simulation are shown. In the top panel we show the rates at a distance of 2 kpc: the inflow rate ($\sim 6\ M_\odot\ \text{yr}^{-1}$) is, on average, higher than the outflow rate ($\sim 2\ M_\odot\ \text{yr}^{-1}$). In the bottom panel we show the rates at a distance of 5 kpc: we have an inflow rate of $\sim 3\ M_\odot\ \text{yr}^{-1}$ and an outflow rate that is zero beside a few spikes that can reach $4\ M_\odot\ \text{yr}^{-1}$. The stellar feedback is able to launch gaseous outflows over 5 kpc, with a rate of $\sim 5\ M_\odot\ \text{yr}^{-1}$. However, since these large distances can be reached only by the strongest outflows, the transported mass of gas is very low ($\sim 1 - 2 \times 10^8\ M_\odot$) and only a few peaks in the outflow rate are present. It is worth to notice that most of the peaks in the inflow rate correspond to depressions in the outflow rate and vice versa. This indicates the presence of a gas circulation at the interface between the disc and the halo (occupied by the corona) of the galaxy: the stellar feedback produces galactic fountains (outflows) that pass through the corona and then fall back onto the disc (inflows). We expect this phenomenon to drag also some coronal gas (in addition to the one accreted onto the disc, powering the initial bump in the star formation) that could refill the disc and sustain the star formation.

In Figure 4.16 we also superimposed the SFR, with an offset of $6\ M_\odot\ \text{yr}^{-1}$ (grey dotted line) for clarity. The first noticeable thing is that the average SFR ($\sim 5\ M_\odot\ \text{yr}^{-1}$) is below the average inflow rate, implying that the supplying

of gas from the corona has a non negligible influence on the total gas budget of the galaxy, making it an important reservoir for the star formation. Taking these numbers at face value, we can infer that star formation can be sustained entirely by the accretion of the coronal gas. Indeed, the inflowing gas is for the major part caused by the accretion due to coronal gas. Computing the *net inflow rate* inflow rate $-$ outflow rate $= \sim 4\ M_\odot\ \mathrm{yr}^{-1}$, it follows that only a fraction of the inflows is accounted by the gas that is ejected from the disc and that return back to it, the rest of the gas must be accreted from the corona. Secondly, we note that the SFR peaks correspond, approximately, to the peaks in the inflow rate, but shifted by ~ 0.2 Gyr. To help the eye, we have highlighted this behaviour by inserting grey and blue arrows to indicate peaks in the SFR and in the inflow rate respectively. The presence of this correlation between the SFR and outflow rate trends means that the gas accreted from the corona can efficiently cool and form stars in the disc of the galaxy. This highlights a strict connection between these two phenomena, showing how the star formation is intimately linked to the accretion of gas from the external environment.

In Figure 4.18 we show the outflow and inflow rates for the COR_S2 simulation at 2 kpc (top left panel) and at 5 kpc (bottom left panel). The outflow and inflow rates are smaller with respect to COR_S1 at both the distances from the disc. The average inflow rate at 2 kpc is $\sim 2.5\ M_\odot\ \mathrm{yr}^{-1}$, again an initial bump is present, reaching $10\ M_\odot\ \mathrm{yr}^{-1}$ in the first 0.1 Gyr. At 5 kpc the same trend is present but with a lower rate ($\sim 1\ M_\odot\ \mathrm{yr}^{-1}$). The outflow rate has an average value of $\sim 0.3\ M_\odot\ \mathrm{yr}^{-1}$, with few peaks that reach $2\ M_\odot\ \mathrm{yr}^{-1}$ of maximum, whereas no outflows are launched to a scale of ~ 5 kpc. Also in this case we note that the average SFR (dash-dotted grey line), i.e. $\sim 1.9\ M_\odot\ \mathrm{yr}^{-1}$, is below the average inflow rate (dash-dotted light blue line) of $\sim 2.5\ M_\odot\ \mathrm{yr}^{-1}$, therefore the accreted gas is sufficient to sustain the formation of new stars in this case too. Again, the SFR (dash-dotted grey line) has the same trend of the inflow rate.

In Figure 4.19 we show the outflow and inflow rates for the COR_S3 simulation. The outflow and inflow rates are even lower, with an inflow rate average value of $\sim 1.8\ M_\odot\ \mathrm{yr}^{-1}$ and an outflow rate of $\sim 0.1\ M_\odot\ \mathrm{yr}^{-1}$. At 5 kpc the inflow rate is $\sim 0.2\ M_\odot\ \mathrm{yr}^{-1}$, while no outflows are launched to this scale.

From the comparison between the three simulations, in which the only difference is the mass of the corona, we understand how this parameter controls the circulation of gas in the galaxy. In COR_S1 the coronal gas is more efficiently accreted onto the disc leading to a higher SFR. The newly formed stars inject momentum and energy in

the ISM causing the ejection of a fraction of the gas. As explained in Chapter 1 this mechanism is responsible for the coronal accretion on the disc. Beside the first large bump, we noted that the inflow rate increases with the mass of the corona, but also with the outflow rate. Therefore, a higher outflow rate, caused by a more efficient star formation, increases the accretion efficiency of the corona, sustaining the star formation also at large distance from the center after 2 Gyr; this is corroborated by the results on gas mixing at the disc-corona interface that we describe in Subsection 4.2.2. In COR_S2 and COR_S3 the accretion is lower and the denser regions are concentrated in the center of the disc, causing a lower star formation rate.

We also computed the *wind mass loading factor* for both the 2 kpc and the 5 kpc slabs, comparing the outflow rate to the SFR: $\beta = $ (outflow rate)/SFR. This quantity estimates the efficiency of the stellar feedback in generating outflows of gas. In Figure 4.17 we show β for the COR_S1 simulation. The average value (dash-dotted green line), that is computed avoiding the initial peak in the first 0.1 Gyr, is $\beta \sim 0.6$ considering the rates computed at a distance of 2 kpc (top panel), and decreases to $\beta \sim 0.14$ in the other case (bottom panel), confirming a damping of these outflows at larger distances from the disc. We computed the same quantities for the COR_S2 and COR_S3 simulations. The mass loading factor for both the simulations shows the same trend of COR_S1 and also β is decreasing with the mass, it has a value of 0.2 for COR_S2 and 0.08 for COR_S3. These findings point out that the efficiency of the star formation in generating strong outflows is higher for higher masses of the corona: a lower mass of the corona implies a lower SFR but also a lower outflow rate, creating a net factor β that is smaller than the simulation with a higher coronal mass. These values are smaller then the ones found in chemical evolution modeling works, for instance Peeples and Shankar (2011) found values of $\beta \sim 1.4$ and Barrera-Ballesteros et al. (2018) found $\beta \sim 2$ for a Milky Way-type galaxy. On the other hand, Kim and Ostriker (2018) found $\beta \sim 0.1$ in numerical simulations of stellar feedback.
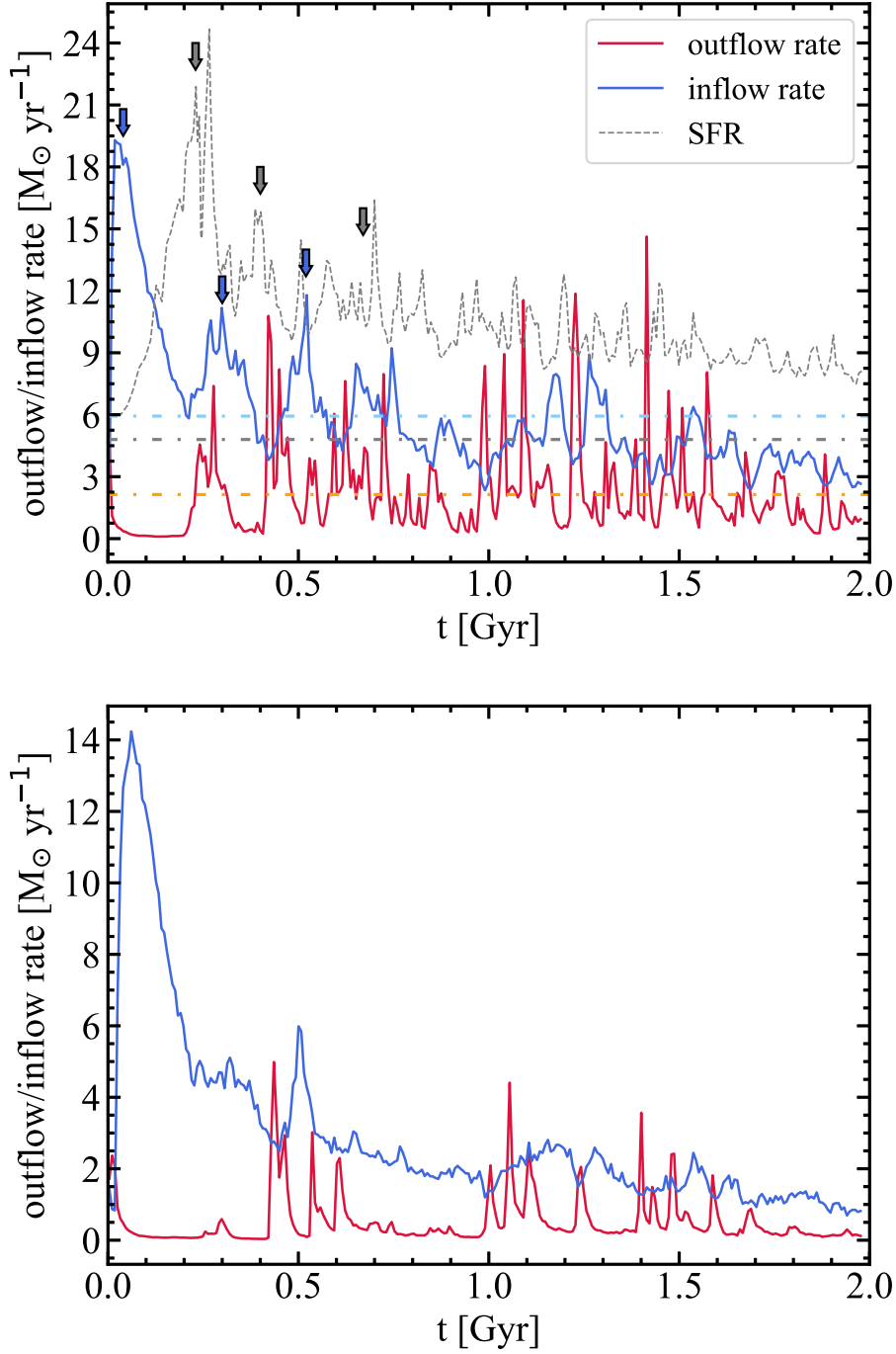
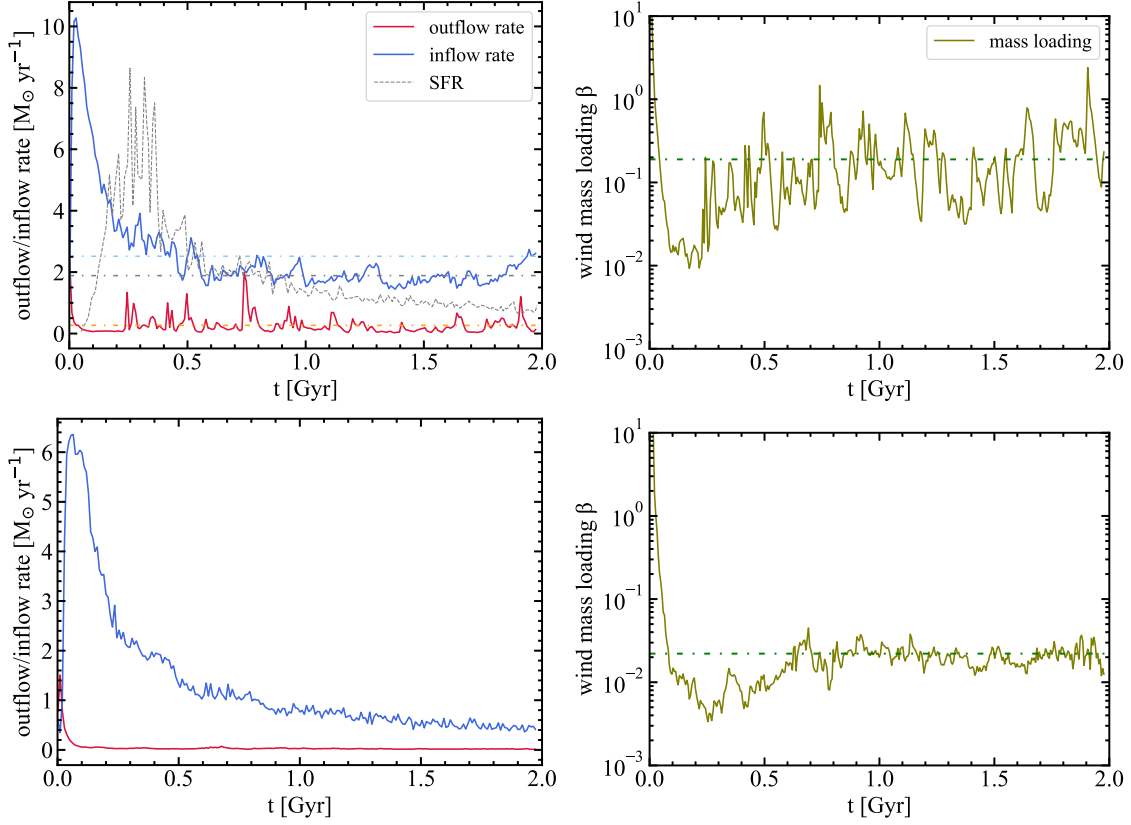**Figure 4.16:** Outflow (red line) and inflow (blue line) rates computed for the cor_s1 simulation, from the gas inside slabs with a 300 pc width located at ± 2 kpc (upper panel) and at ± 5 kpc from the plane of the disc (lower panel). The grey dashed line represents the SFR, shifted by 6 $M_\odot$ yr^{-1} for clarity. In the upper panel the three dash-dotted lines represent the average value of the outflow rate (orange), inflow rate (light blue) and SFR (grey), and the grey and blue arrows represent the peaks in the SFR and in the outflow rate, respectively, highlighting a strict connection between the formation of stars and the accretion of gas from the corona.
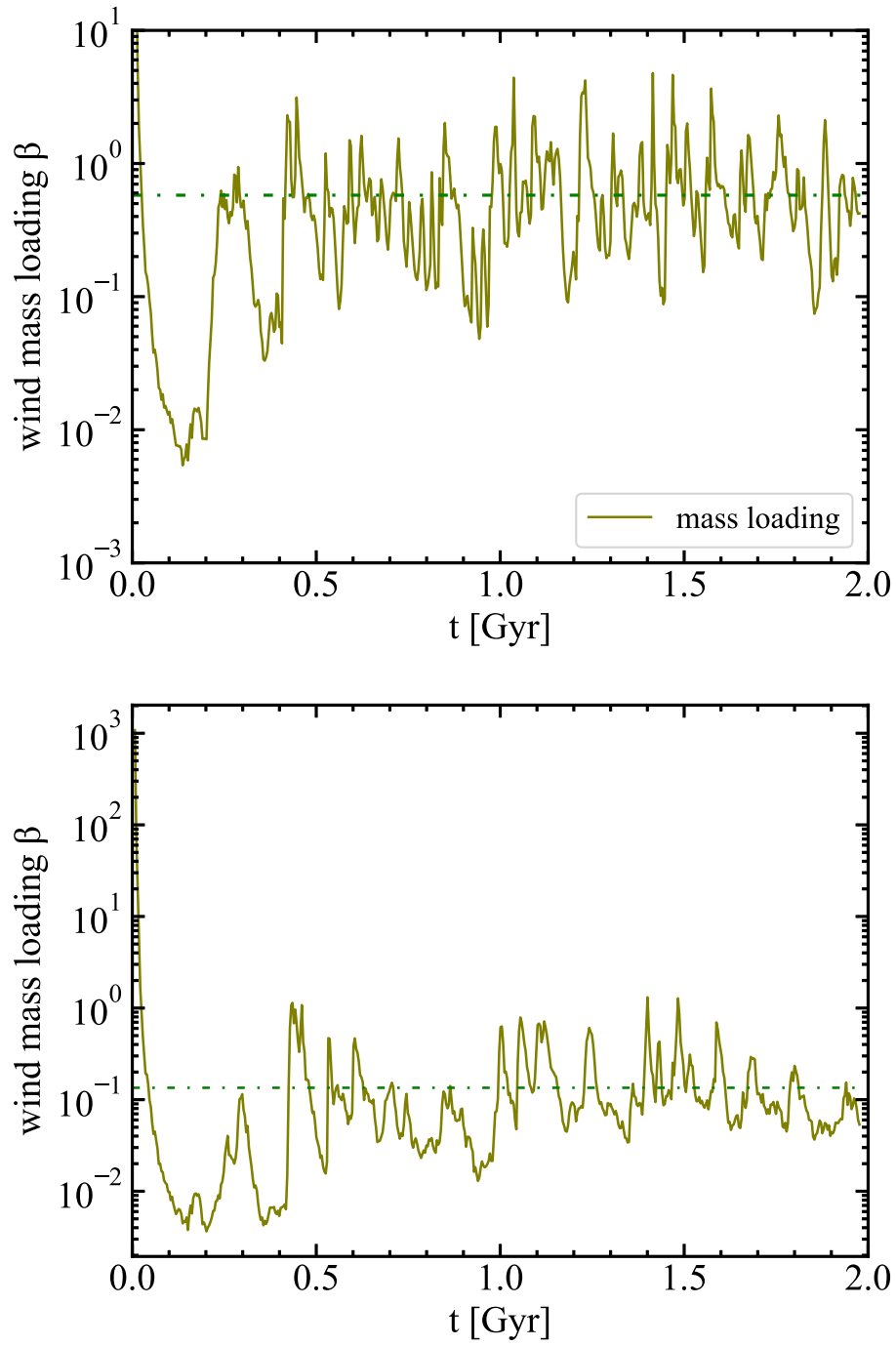
Figure 4.17: Wind mass loading factor β (light green line) in the same two cases of Figure 4.16, the dash-dotted green line represents its average value. This shows the dependence of the mass loading on the height of the outflows over the disc: only the strongest outflows can reach a height of 5 kpc.

Figure 4.18: *Left*: Outflow (red line) and inflow (blue line) rates computed for the COR_S2 simulation, from the gas inside slabs with a 300 pc width located at ± 2 kpc (upper panel) and at ± 5 kpc (lower panel) from the plane of the disc. The dashed grey line represents the SFR. In the upper panel the three dash-dotted lines represent the average value of the outflow rate (orange), inflow rate (light blue) and SFR (grey), in the lower panel the dashed line represents the SFR. *Right*: Wind mass loading factor β (light green line) in the same two cases, the dash-dotted green line represents its average value.
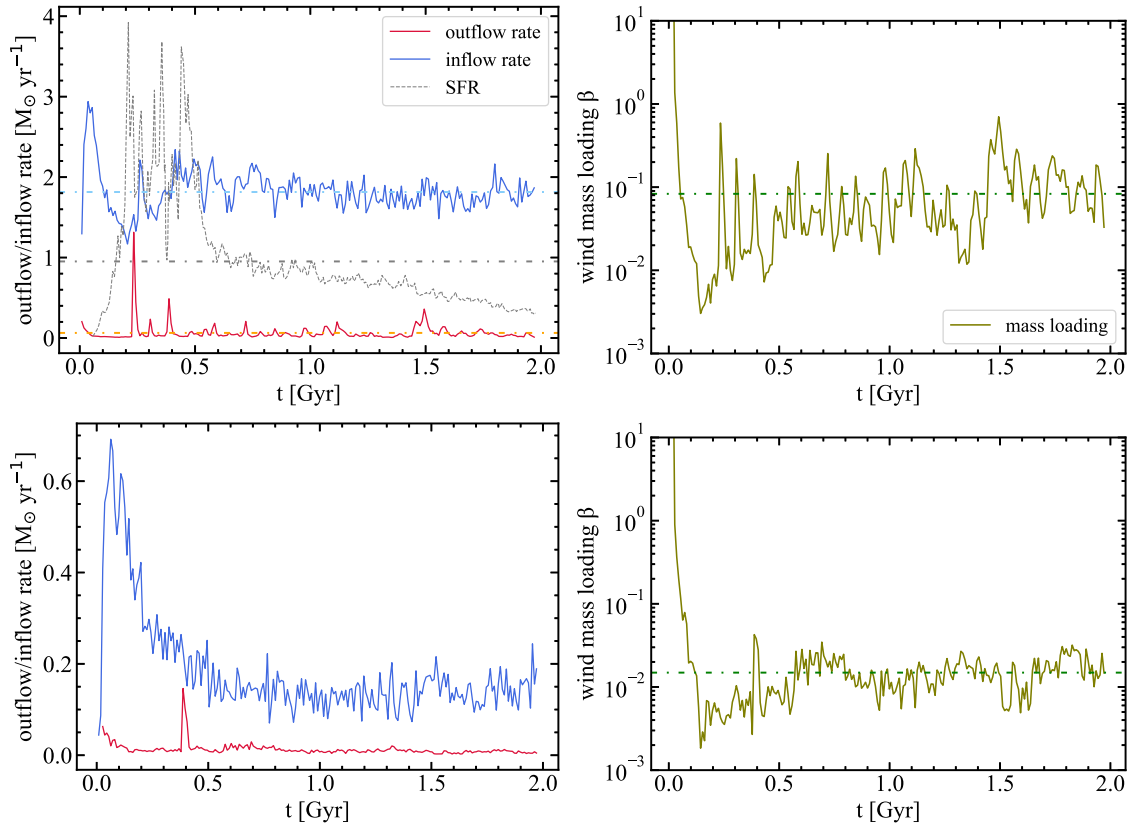
Figure 4.19: Same as Figure 4.18 for the COR_S3 simulation.

4.2.2 Gas mixing at the disc-corona interface

Another fundamental aspect that has to be considered is the gas mixing at the disc-corona interface. This phenomenon is particularly important for its effect on the cooling of the corona. In fact, the interaction of the cold gas ejected from the disc and the hot gas of the corona produces a mixture at intermediate temperature whose cooling is more efficient. Furthermore, the coronal gas has a low metallicity ($Z_{\rm cor} \sim 0.1\ Z_\odot$), unlike the gas in the disc ($Z_{\rm d} \sim 1\ Z_\odot$) and the combination between these two gas phases forms a gas with a metallicity higher than the original value of the corona, further promoting radiative cooling. We analyze these two aspects studying temperature and metallicity distributions in the zone of interaction between the disc and the corona.

Temperature analysis of the different gas phases

The galaxy is surrounded by a high temperature gas ($T > 10^6$ K) that composes the corona, on the other hand the gas in the plane of the disc is mostly cold ($T < 10^4$ K) and warm ($10^4 < T < 10^5$ K). The SNe generate superbubbles that can reach sizes larger than the width of the disc, ejecting material outside the disc. This material is composed by a mix of cold and hot gas (i.e. the gas inside the superbubble, heated by the shock wave generated by the SNe explosions). We expect this material to mix with the coronal gas in the regions near the disc.

In Figure 4.20 we show the density-weighted projected temperature of the gas for the COR_S1 simulation. First, we note the presence of a multiphase medium around the disc. Within it the temperature reaches $T < 10^3$ K thus allowing the gas to collapse and form stars. At 1 kpc above and below the disc the gas is hotter, reaching 10^4 K. Outside of the disc of the galaxy the temperature is dominated by the coronal gas ($T > 10^6$ K). The temperature of the aforementioned gaseous outflows is in general at an intermediate level ($10^4 < T < 10^5$ K) thanks to the mixing with the gas from the corona. The same characteristics can be seen in Figure 4.21, where we show the temperature projections for COR_S2; as already described for the density projections, the outflows in this case are very limited, as the cold and warm gas is confined very close to the plane of the disc ($|z| < 2$ kpc) and only a few large-scale outflows are visible; this is also confirmed by the low mass loading factor. In Figure 4.22 we show the temperature projection for the COR_S3 simulation, the warm gas is more extended with respect to COR_S1 and COR_S2, reaching ~ 5 kpc above and under the disc. The outflows are almost negligible. In this case the warm gas
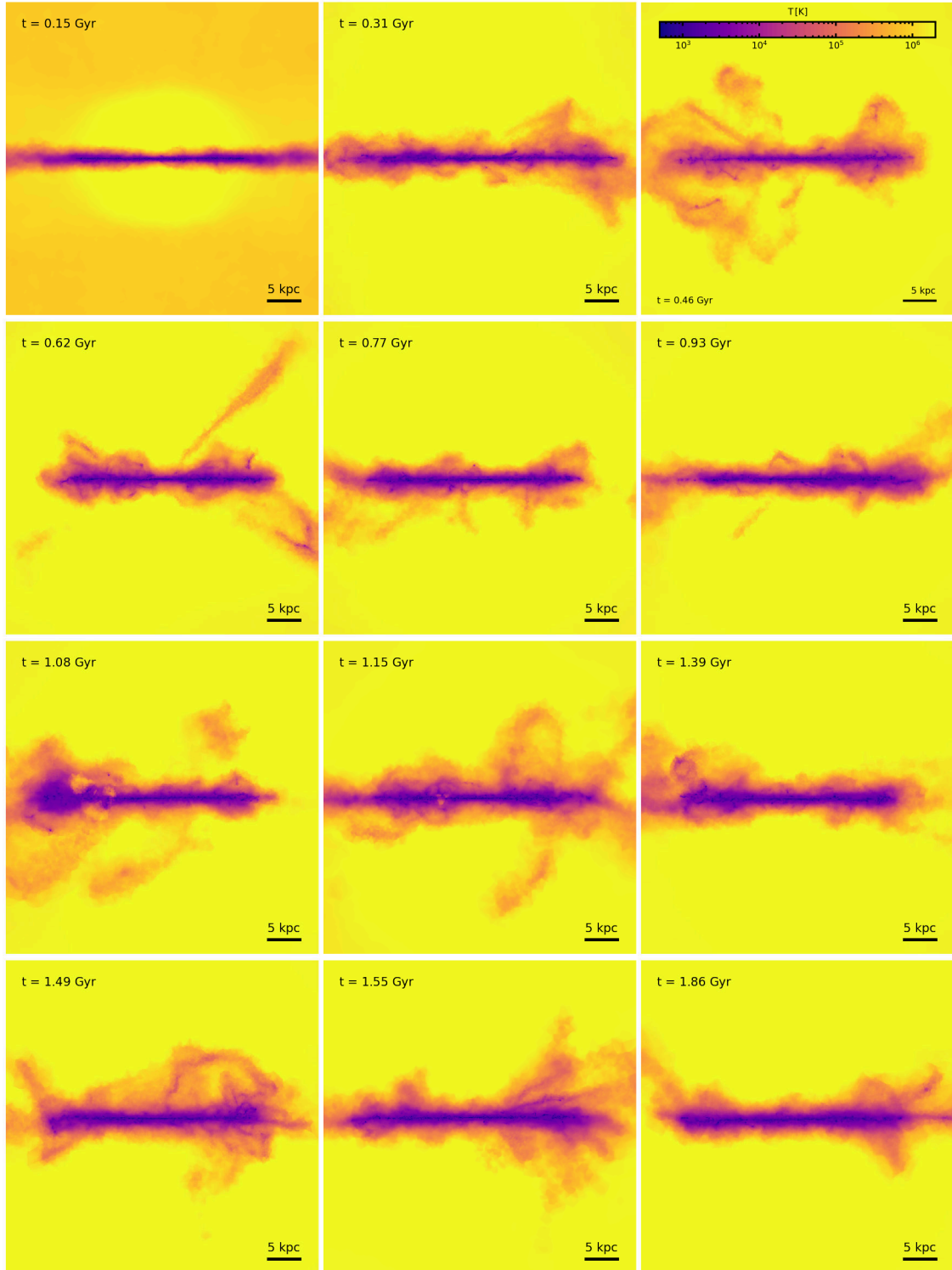
Figure 4.20: Density-weighted temperature in edge-on projections of the Milky-Way like galaxy computed with the *SMUGGLE* model at times indicated in each panel, for the COR_S1 simulation. Each panel is 50 kpc across and in projection depth with the presence of a total number of 1024 × 1024 pixels that give a resolution of ∼ 50 pc. We can visually appreciate the mixing between the material ejected from the disc and the hot corona, with the formation of an intermediate temperature gas phase at the disc-corona interface.
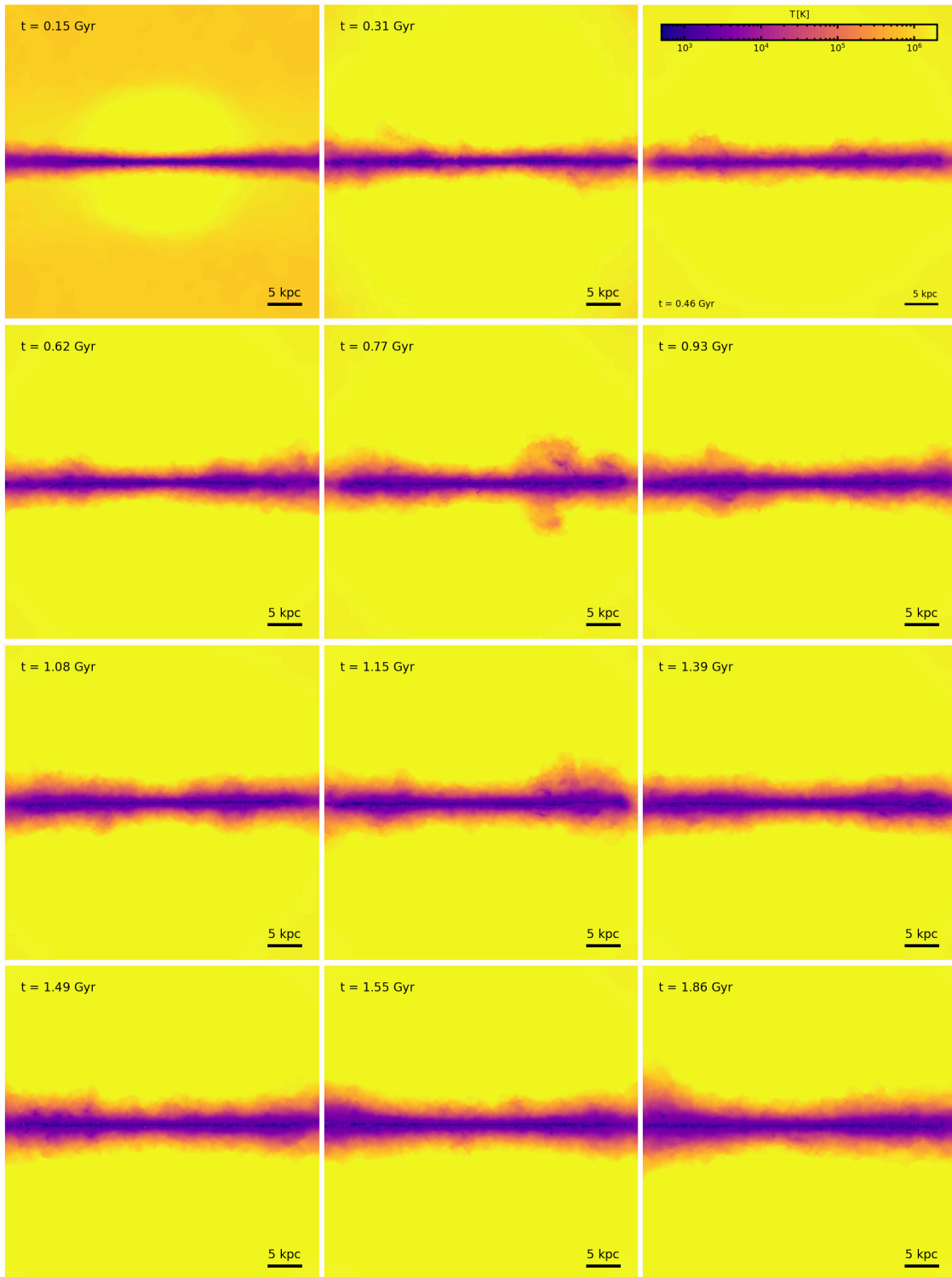
Figure 4.21: Same as Figure 4.7 but for the COR_S2 simulation.
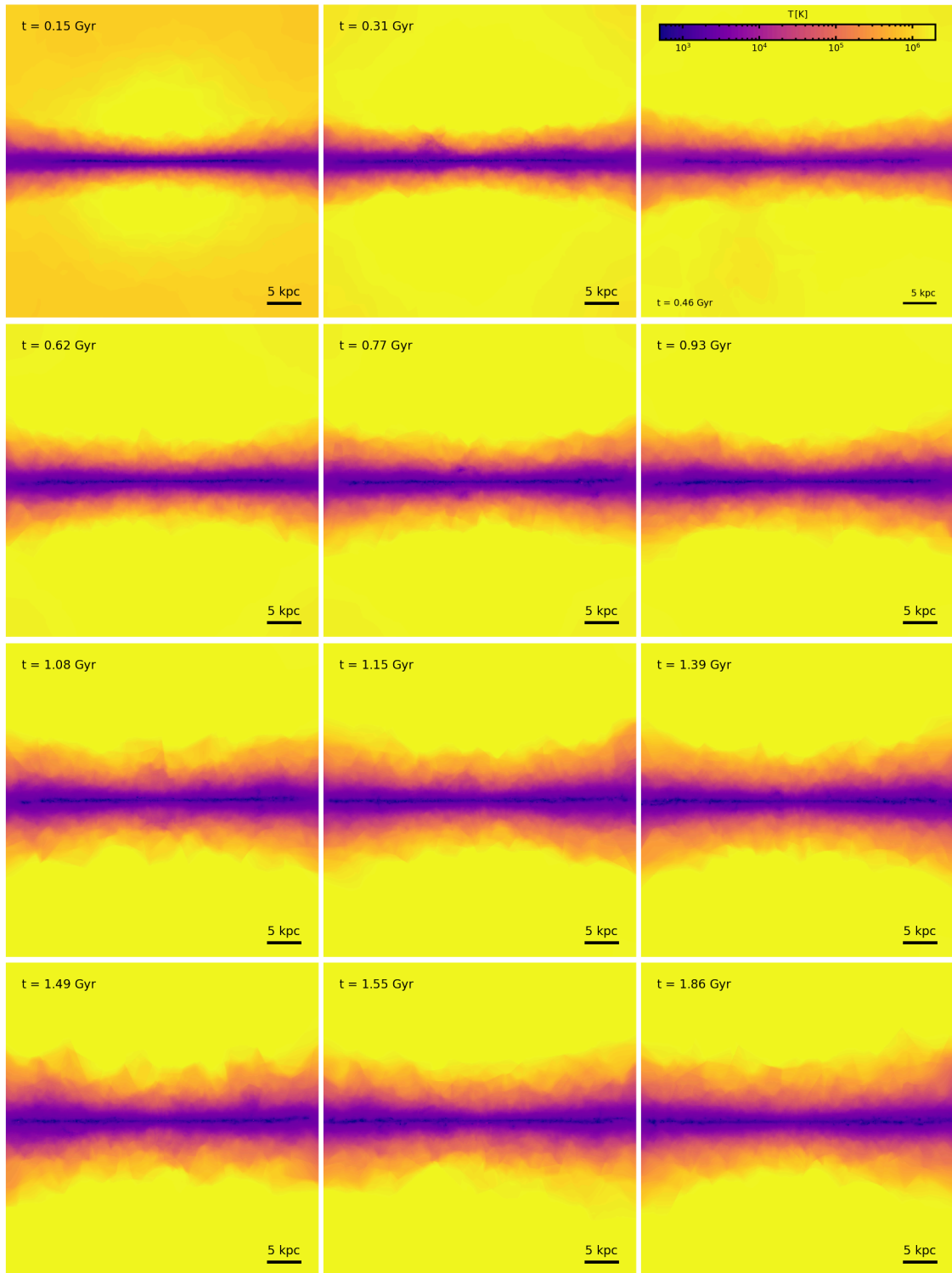
Figure 4.22: Same as Figure 4.21 but for the COR_S3 simulation.

is distributed also over 5 kpc above and below the disc. This can be explained with two considerations: the corona has a very small mass in this setup, and a small quantity of cold gas ejected from the disc is sufficient to rapidly decrease the corona temperature. Furthermore, since the mass of each gas cell in the ICs is fixed, a small mass results in a very low number of cells. This might cause an insufficient spatial resolution in the interface region.

To study the evolution of the different gas phases we computed the mass of the gas, divided in hot ($T > 10^6$ K), warm ($10^4 < T < 10^6$ K) and cold ($T < 10^4$ K) gas. This gas has been selected taking all gas particles with $R < 30$ kpc and $|z| > 2$ kpc (gas outside the disc) or $|z| < 2$ kpc (gas within the disc). In Figure 4.23 we show the evolution of the mass of these different phases as a function of time for the COR_S1 simulation. Considering the gas at $|z| > 2$ kpc (left-hand panel), we see that the mass of the hot gas (red line) decreases in time, this is consistent with a scenario in which the corona is accreted onto the disc, in fact the hot gas mass passes from $\sim 2 \times 10^8$ M$_\odot$ to $\sim 2 \times 10^6$ M$_\odot$ in 2 Gyr. The warm and cold phases have a coeval evolution, with the cold gas dominating in mass. We analyze in more detail these phases in Figure 4.25. The gas at $|z| < 2$ kpc (right-hand panel) is dominated by the cold gas of the disc, the mass of this phase remains almost constant for the entire lifespan of the simulation at a value $\sim 3 \times 10^9$ M$_\odot$, showing the efficiency of the coronal gas to cool down and replenishing the reservoir of gas eligible for star formation. With an average SFR of ~ 5 M$_\odot$ yr^{-1} we expect $\sim 10^{10}$ M$_\odot$ of gas to turn into stars, it would not be possible to maintain this high SFR without the presence of an efficient accretion of gas from outside the disc. Also warm and hot gas is present, with masses almost negligible with respect to the cold phase.

In Figure 4.24 we see the gas phases evolution for the COR_S2 simulation. At $|z| > 2$ kpc (left-hand panel) the hot gas passes from $\sim 7 \times 10^7$ M$_\odot$ to $\sim 2 \times 10^6$ M$_\odot$, showing a slightly less efficient accretion with respect to the higher coronal mass present in COR_S1. Again the warm and cold phases are mixed together presenting the peaks in their mass evolution at the same time. The gas at $|z| < 2$ kpc has properties similar to COR_S1 with the cold gas keeping a constant value of $\sim 2 \times 10^9$ M$_\odot$ over the entire simulation. Despite having a similar cold gas mass in the disc the two simulations COR_S1 and COR_S2 have a very different SFR. This difference resides in the different accretion from the corona, in fact, the accreted mass in the region $R < 30$ kpc in COR_S1 ($\sim 9.9 \times 10^7$ M$_\odot$) is greater then the one in COR_S2 ($\sim 6.8 \times 10^7$ M$_\odot$). This helps the galaxy in COR_S1 to keep high-density regions of star formation over the entire disc for 2 Gyr (Figure 4.7), while in COR_S2 after

~ 1 Gyr the presence of these regions has significantly decreased (Figure 4.8) and in COR_S3 only in the center of the galaxy the gas density is high enough to form stars after ~ 1 Gyr (Figure 4.9). Moreover, a higher initial SFR causes a higher SN

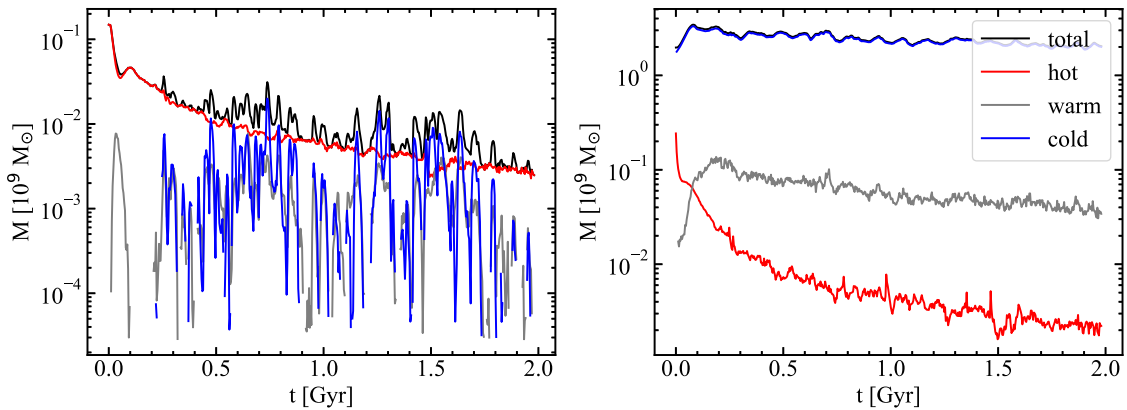$$M_{\mathrm{cor}}(r < r_{\mathrm{vir}}) = 1.38 \times 10^{10} \ M_{\odot}$$
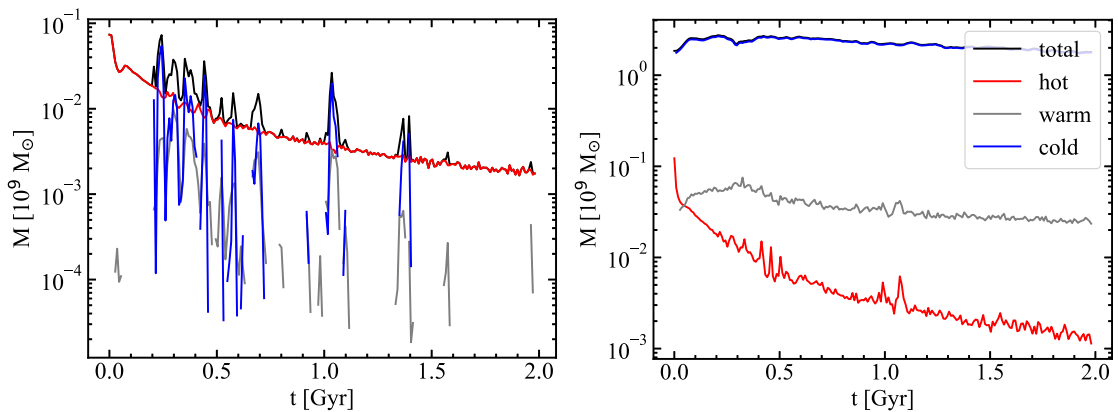

Figure 4.23: Mass of the gas with a cylindrical radius $R < 30$ kpc and $|z| > 2$ kpc (left-hand panel) or $|z| < 2$ kpc (right-hand panel) for the COR_S1 simulation as a function of time, divided in three ranges of temperature: hot ($T > 10^6$ K), warm ($10^4 < T < 10^6$ K) and cold ($T < 10^4$ K) gas.

$$M_{\mathrm{cor}}(r < r_{\mathrm{vir}}) = 6.8 \times 10^9 \ M_{\odot}$$

Figure 4.24: Mass of the gas with a cylindrical radius $R < 30$ kpc and $|z| > 2$ kpc (left-hand panel) or $|z| < 2$ kpc (right-hand panel) for the COR_S2 simulation as a function of time, divided in three ranges of temperature: hot ($T > 10^6$ K), warm ($10^4 < T < 10^6$ K) and cold ($T < 10^4$ K) gas.

rate. We speculate that the SNe can also act as a positive feedback, compressing the gas in the disc at the edges of the bubbles formed by their explosions, and helping

in maintaining high density gas filaments in the disc.

In Figure 4.25 the gas phases evolution for CoR_S3 is shown, only little cold mass is present in the gas at $|z| > 2$ kpc (left-hand panel), while looking at the gas at $|z| < 2$ kpc (right-hand panel) we note that the cold gas mass passes from $\sim 2 \times 10^9$ M$_\odot$ to $\sim 8 \times 10^8$ M$_\odot$, since the corona does not have enough mass to replenish the gas consumed by star formation in the disc.

$$M_{\mathrm{cor}}(r < r_{\mathrm{vir}}) = 6.8 \times 10^8 \ M_\odot$$
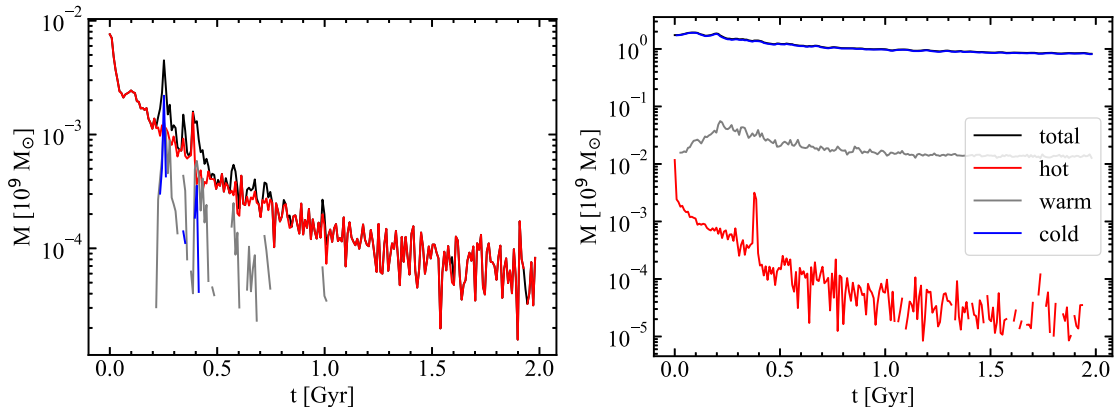

Figure 4.25: Mass of the gas with a cylindrical radius $R < 30$ kpc and $|z| > 2$ kpc (left-hand panel) or $|z| < 2$ kpc (right-hand panel) for the CoR_S3 simulation as a function of time, divided in three ranges of temperature: hot ($T > 10^6$ K), warm ($10^4 < T < 10^6$ K) and cold ($T < 10^4$ K) gas.

In Figure 4.26 we show the evolution of the gas phases at the disc-corona interface for the CoR_S1 simulation, in particular in the region at $2.5 < z < 6$ kpc over and under the disc. We also superimposed the outflow rate (whose values can be read in the right-hand y axis) in the Figures, showing how they are tightly linked to the trend of the cold and warm gas phases, highlighting the galactic fountains origin of the gas in this region. The mass of cold/warm gas has a periodic trend, first increasing and then decreasing over the time, we interpret this as the fountain cycle: first the gas is ejected over the plane of the disc (increase of the cold/warm mass), then after a certain time $\Delta t_{\mathrm{cycle}}$ it fall back onto the disc (decrease of the cold/warm mass) in a different position. In particular, from the width of the different peaks we can qualitatively determine the duration of a given fountain cycle. In CoR_S1 we obtain $\Delta t_{\mathrm{cycle}} \sim 100 - 150$ Myr, in CoR_S2 (shown in Figure 4.27) the fountain cycle has a similar duration. In both the simulations the outflows are composed by a mix of cold and warm gas, with a mass dominance of the cold phase. The cold

mass ejected outside the disc at $2.5 < z < 6$ kpc in each fountain cycle varies from $\sim 2 - 3 \times 10^7$ M$_\odot$ to peaks of $\sim 2 \times 10^8$ M$_\odot$ in COR_S1 and from $\sim 4 - 5 \times 10^6$ M$_\odot$ to $\sim 6 \times 10^7$ M$_\odot$ in COR_S2, this is consistent with the smaller outflow rates present in this simulation. COR_S3 (Figure 4.28) presents a different trend. There are only a few fountain clouds ejected from the disc, with an almost negligible transported mass. At this height from the disc the total mass is dominated by the warm gas, as it is visible in Figure 4.22, but its mass has a value of $\sim 2 \times 10^7$ M$_\odot$ only.
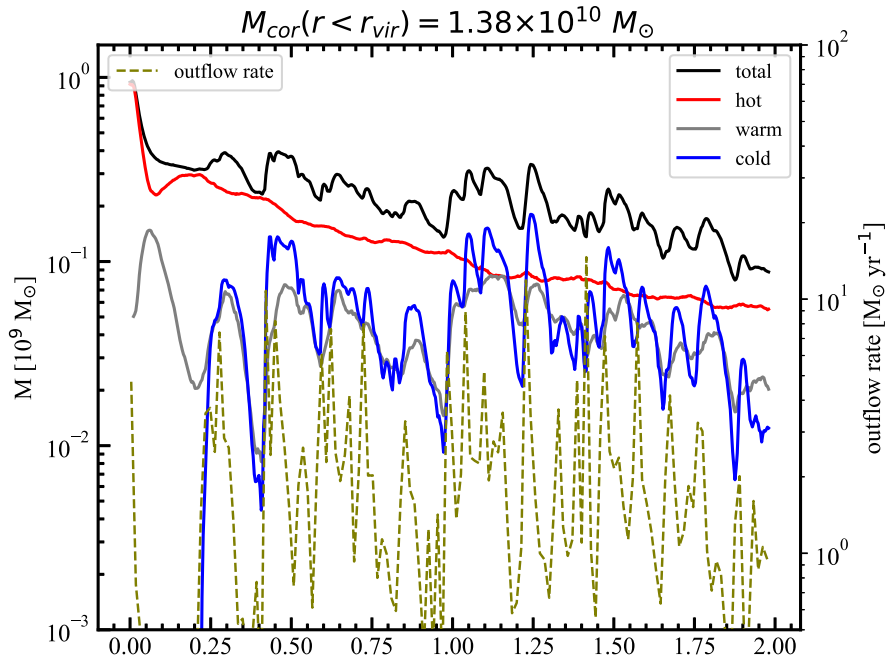

Figure 4.26: Mass of the gas with a cylindrical radius $R < 30$ kpc and $2.5 < z < 6$ kpc above and below the disc for the COR_S1 simulation as a function of time, divided in three ranges of temperature: hot ($T > 10^6$ K), warm ($10^4 < T < 10^6$ K) and cold ($T < 10^4$ K) gas. The cold gas mass is increasing and decreasing over time, showing the presence of a galactic fountain cycle at the disc-corona interface.
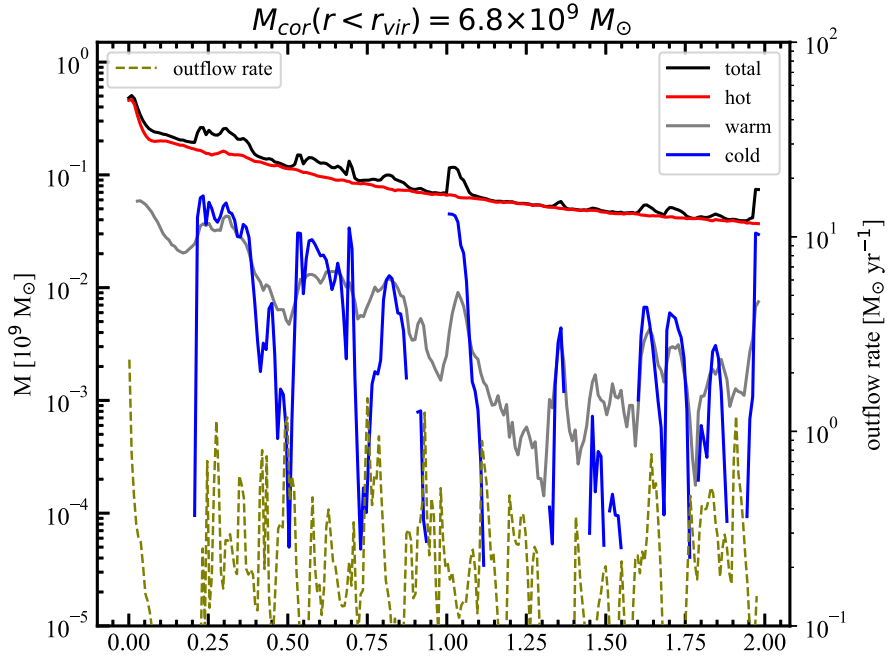
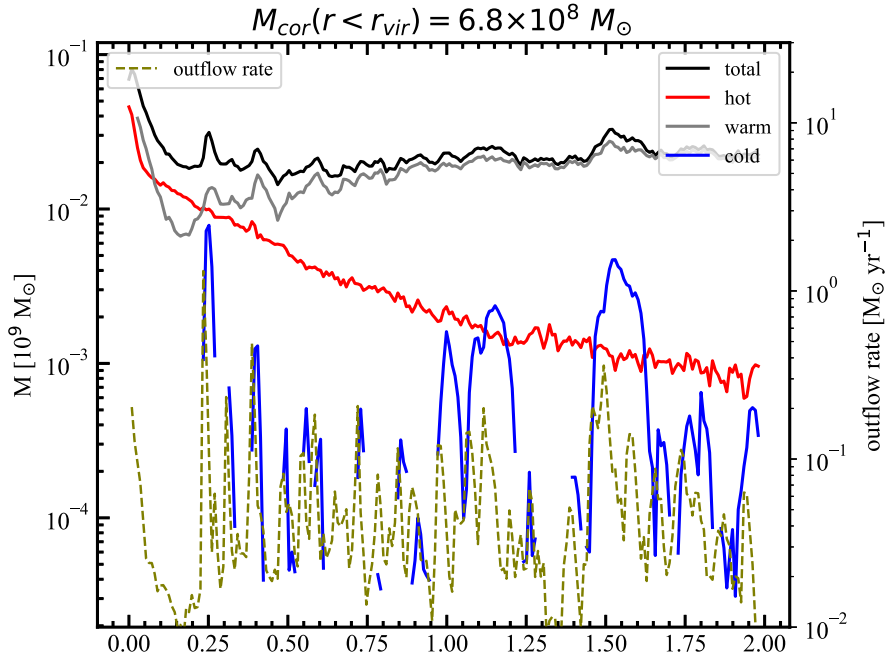**Figure 4.27:** Same as Figure 4.26 but for the COR_s2 simulation.

Figure 4.28: Same as Figure 4.26 but for the COR_s3 simulation.

Metallicity distribution

The accretion of low-metallicity gas from the corona is required from observations in order to solve a series of problem, such as the G-dwarf problem (see Chapter 1). In this subsection we analyze the metallicity distribution in the three simulations. In Figure 4.29 we show the mass-weighted metallicity for the COR_S1 simulation: initially, we have two very distinct metallicities between the disc and the corona. Then, the interaction between the disc and the corona caused by the galactic fountains produce a strong mixing of these two gas phases creating zones at different intermediate metallicities. The outflows of gas are metal-rich, since they are mostly composed of material from the disc. Moreover, a decrease of disc metallicity over the time due to the accretion of the coronal gas can be appreciated. In Figures 4.30 and 4.31 we show the mass-weighted metallicity for COR_S2 and COR_S3, respectively. The gas mixing is clearly smaller as a consequence of the smaller outflow rate, maintaining a high metallicity in the disc.

Also, we have computed histograms that show the metallicity distribution of the gas. We have divided the metallicities from 0 to 1 $Z_\odot$ in uniformly spaced bins of 0.033 $Z_\odot$, in each bin we have calculated the mass of the gas present at this metallicity. The histogram has been computed for different times: $t = 0$, 0.5, 1, 1.5, 2 Gyr. At $t = 0$ Gyr all the mass is located at 0 $Z_\odot$ and 1 $Z_\odot$, as set in the ICs (Chapter 3), then the evolution takes place and the mixing creates gas at different metallicities. In particular, the COR_S1 simulation is shown in Figure 4.32: at 2 Gyr the maximum metallicity reached is ~ 0.6 $Z_\odot$ ($\times 10^7$ $M_\odot$) and the majority of the gas ($\sim 8 \times 10^9$ $M_\odot$) is distributed around 0.5 $Z_\odot$. A non-negligible portion of gas is distributed between 0 $Z_\odot$ and 0.5 $Z_\odot$. The same features are present in COR_2 (Figure 4.33): here, at 2 Gyr most of the gas ($\sim 5 \times 10^9$ $M_\odot$) is distributed around 0.67 $Z_\odot$ (i.e. the maximum metallicity). Of course, a smaller coronal mass accreted brings to a reduction in the dilution of the gas metallicity. In Figure 4.34 we show the histogram for COR_S3, the mixing of the gas is visibly smaller, in fact at 2 Gyr the disc is mostly at 0.9 $Z_\odot$. As we expected, the mass of the corona largely affects the efficiency of the mixing at the interface, more massive coronae lead to higher accretion rates, diluting the disc metallicity more efficiently.

We conclude by noting that the synthesis of heavy elements from the stellar evolution is a feature present in the *SMUGGLE* model, but for simplicity has been disabled in our simulations. Therefore, in our case, chemical evolution is caused only by the mixing of the initial two gas phases at different metallicity. The synthesis and ejection of new metals from stars would tend to move the metallicity of the

ISM toward larger values. We will evaluate the effects of this physical process in a future analysis.
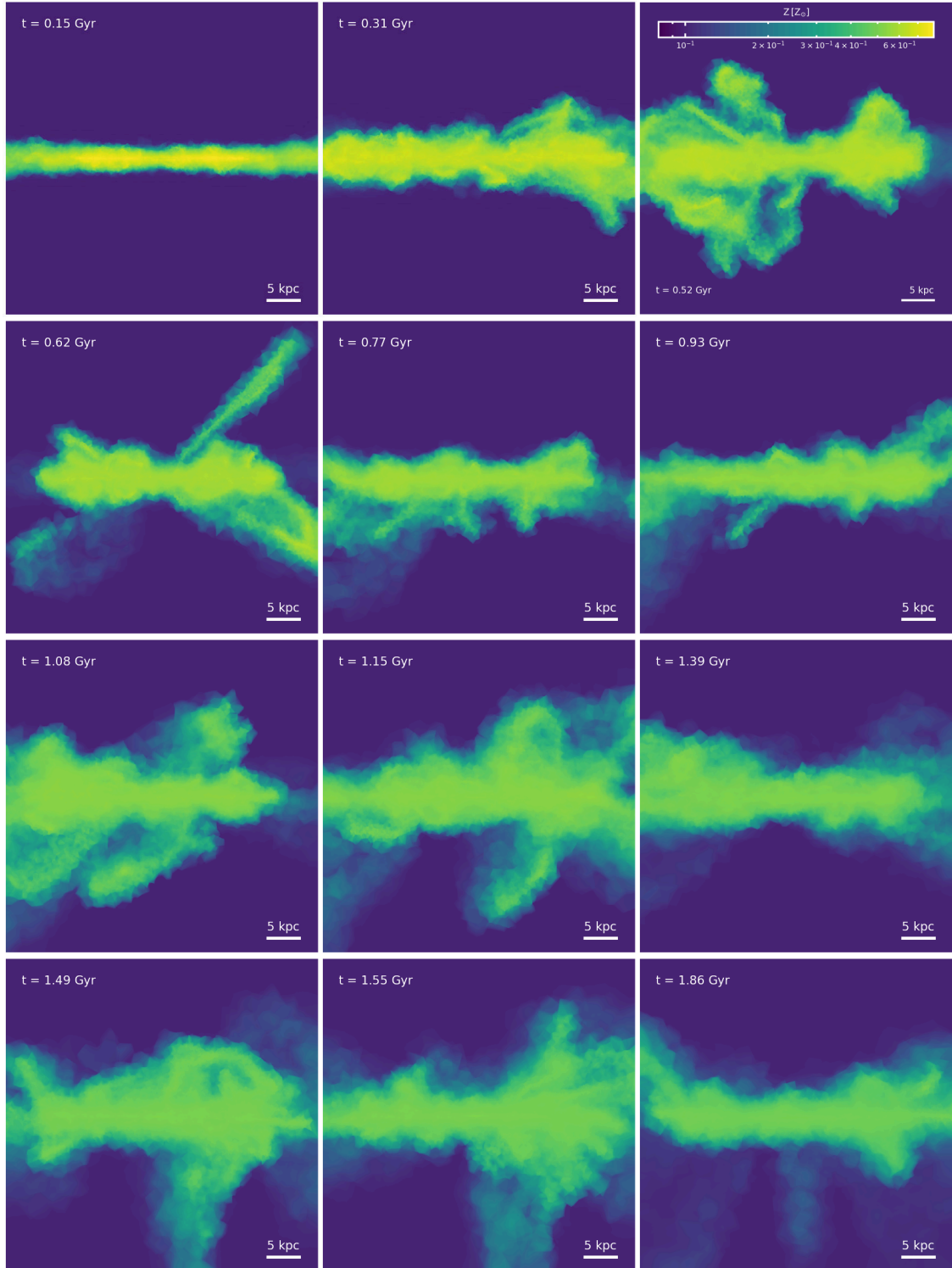
Figure 4.29: Mass-weighted metallicity in edge-on projections of the Milky-Way like galaxy computed with the *SMUGGLE* model at the times indicated in each panel for the COR_S1 simulation. Each panel is 50 kpc across and in projection depth with a total number of 1024 × 1024 pixels that give a resolution of ∼ 50 pc. We can visually appreciate the mixing between the material ejected from the disc and the hot corona, with the formation of an intermediate metallicity gas phase at the disc-corona interface.
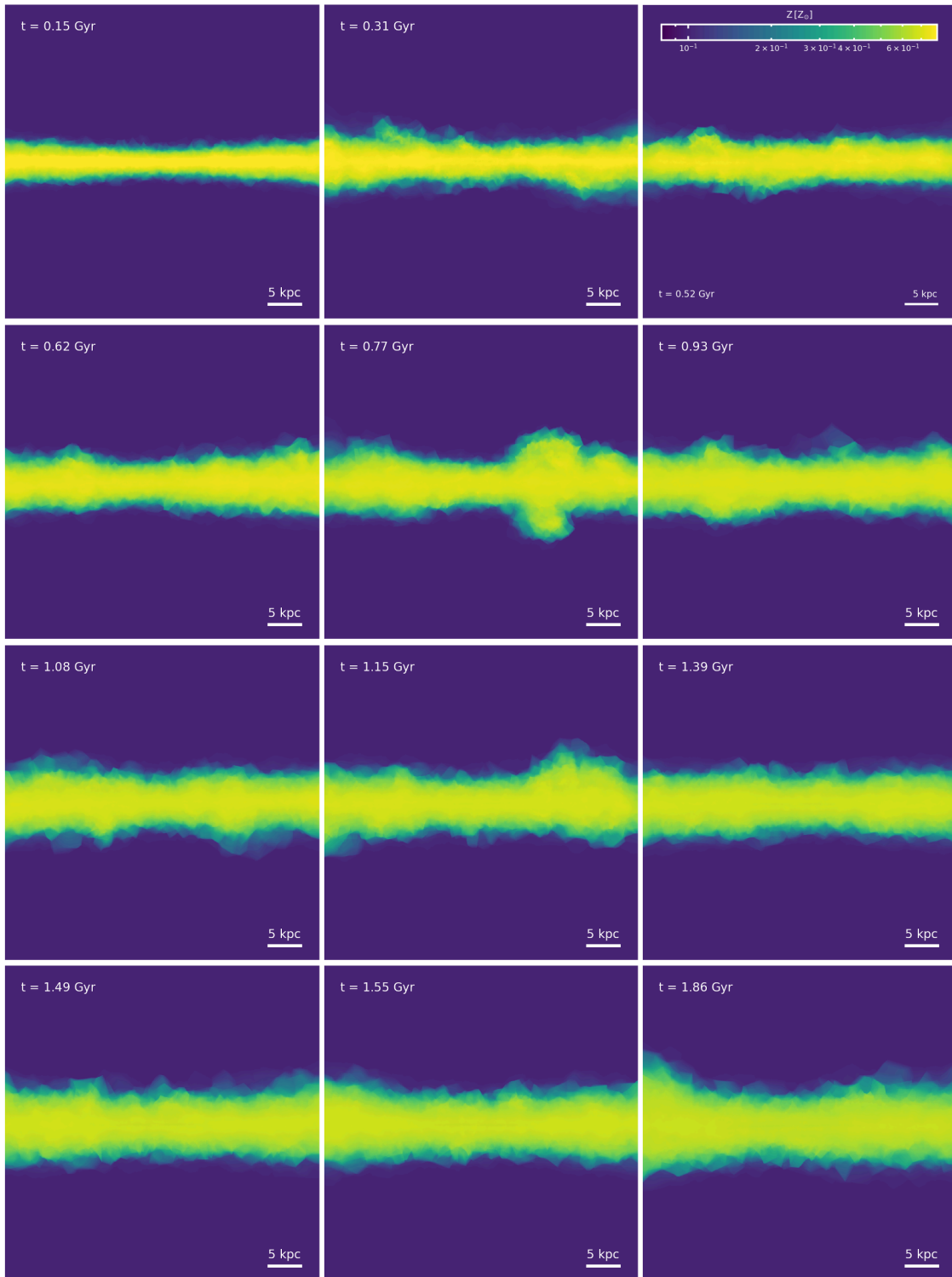
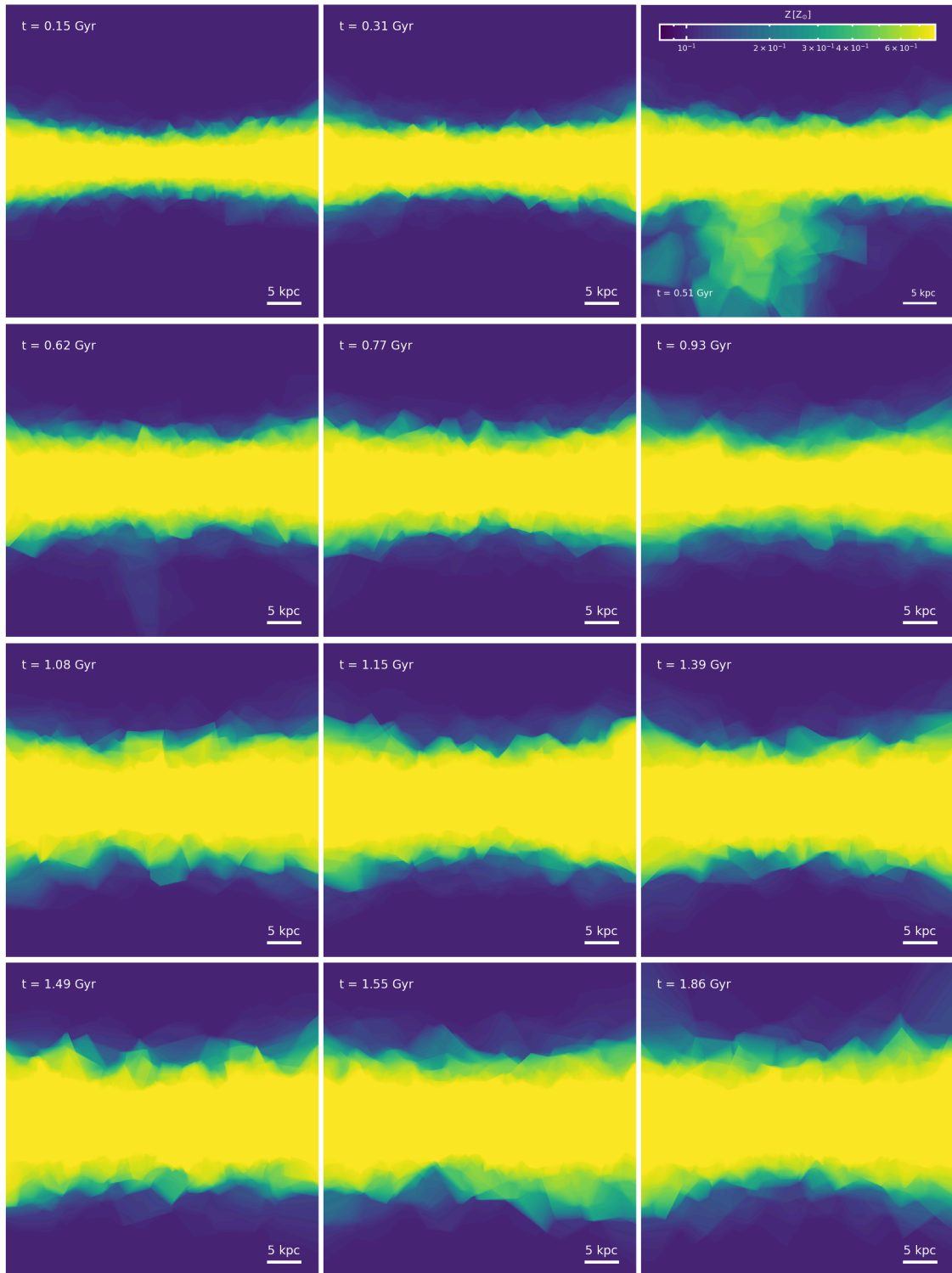**Figure 4.30:** Same as Figure 4.29 but for the COR_S2 simulation.

Figure 4.31: Same as Figure 4.29 but for the COR_S3 simulation.

Figure 4.32: Mass of the gas as a function of metallicity at t=0, 0.5, 1, 1.5, 2 Gyr for the COR_S1 simulation. The histograms are divided in bins of 0.033 $Z_\odot$. At 0 Gyr the gas is distributed in distinct peaks at 0.1 and 1 $Z_\odot$, at later times gas mixing takes place generating gas with a more extended range of metallicities.

Figure 4.33: Same as Figure 4.32 but for the COR_S2 simulation.

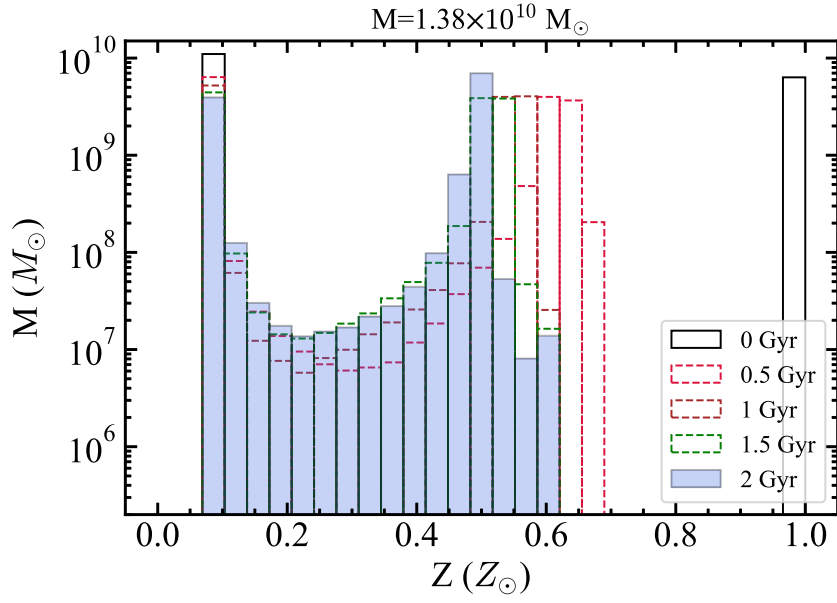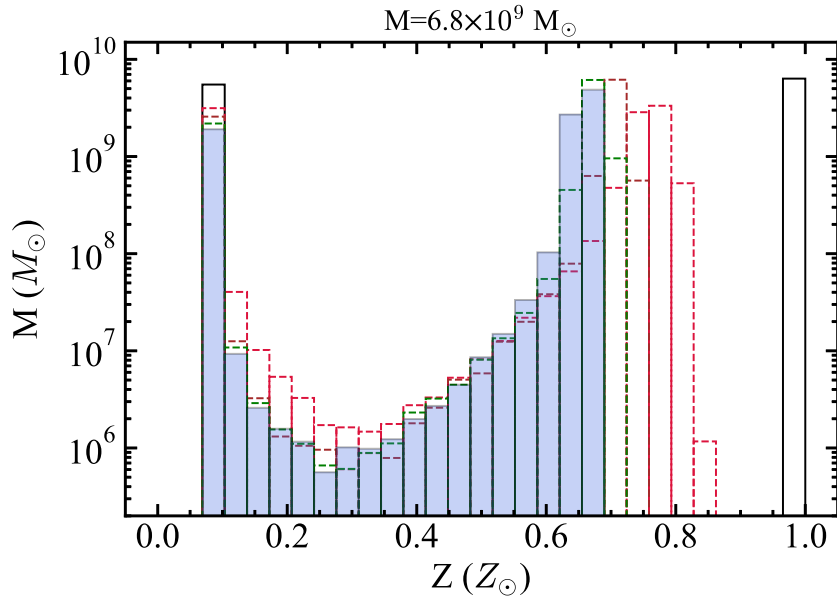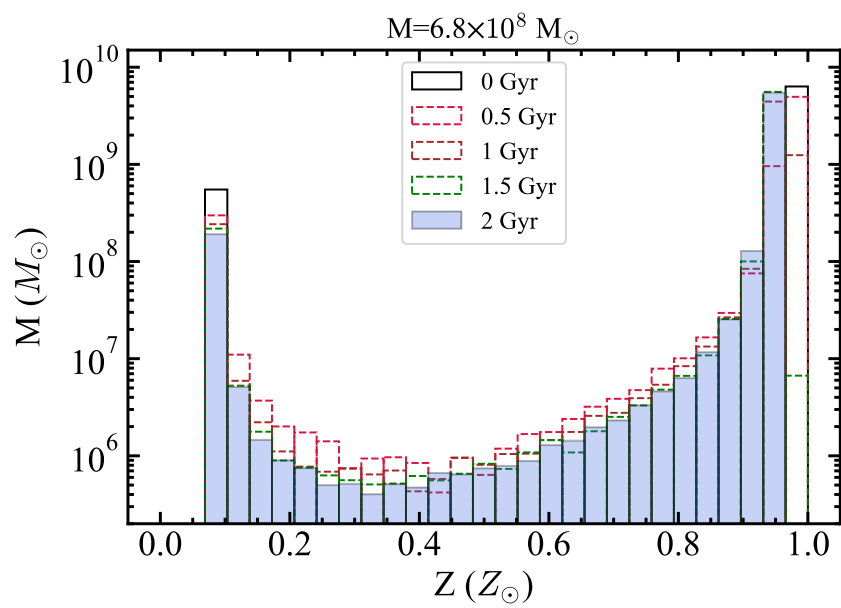**Figure 4.34:** Same as Figure 4.32 but for the COR_S3 simulation.

Summary and Conclusions

<div style="text-align: right;">

5

</div>

In this Thesis work we studied the evolution of a series of multicomponent N-body hydrodynamical models representative of a Milky Way-like galaxy embedded in a hot gaseous atmosphere, the so-called corona, with the help of numerical simulations. In particular, we focused on the interaction between the disc and the corona caused by the gas exchanges between these two components mediated by stellar feedback. We studied several aspects of such an interaction, such as the balancing between the star formation and the outflows/inflows of gas and the mixing between the disc and the corona. We analysed how these aspects are sensitive to the total mass of the coronal gas employing the moving-mesh code AREPO and the explicit stellar feedback and interstellar medium model *SMUGGLE* to carry out our simulations. After a short discussion of the algorithms implemented in the AREPO code and a presentation of the key aspects of the *SMUGGLE* model (Chapter 2), in Chapter 3 we have successfully built a set of initial conditions for the hydrodynamical N-body simulations analyzed in this work that picture an equilibrium configuration for our multicomponent galaxy containing a galactic corona. This configuration has then been used to perform both adiabatic simulations and "full-physics" simulations with the *SMUGGLE* model. The main results of these calculations can be summarized as follows:

- In Section 4.1 we have tested our initial configuration in adiabatic simulations, finding that the density profiles and the kinematics of the different components are maintained for 2 Gyr of evolution.

- In Section 4.2.1 we found that the corona is the main contributor to the material sustaining star formation in the galaxy: the star formation takes place from the gas accreted from this component, without which the galaxy would quench the star formation in a short time. Higher SFR levels have been found for the higher coronal mass simulation, highlighting a correlation between the mass of the coronal gas and the SFR: a higher corona mass helps the star formation thanks to the more efficient formation of high-density filaments across the entire disc of the galaxy. We have also analyzed the inflow and outflow

rates, finding a connection between the gas accreted onto the disc of the galaxy and star formation: an increase in the inflow rate is directly followed by a decrease of the SFR but, on average, with a delay of ~ 0.2 Gyr. We observe also the formation of gaseous outflows thanks to the combined effects of the different stellar feedback processes implemented in the *SMUGGLE* model. The alternation of the peaks in the outflow and inflow rates, for which each outflow-dominant phase is followed by an inflow-dominant phase, suggests the presence of a circulation of the gas between the galactic disc and the corona. Also, the accretion of gas might potentially be helped by the interaction between the galactic fountains and the coronal gas, favoring its cooling.

- In Section 4.2.2 we have analyzed the time evolution of the different gas phases present in the galaxy (cold, warm and hot gas). We found that the cold gas ejected from the disc is efficiently mixed with the gas from the corona forming, indeed, a mixture of intermediate temperature gas. The cold and warm extraplanar gas mass present in the interface region ($2.5 < z < 6$ kpc), increases and decreases over the time and this has been interpreted as gas ejected from the disc, in the form of a galactic fountain flow. This hypotesis corroborated by the fact that the peaks in the mass of cold gas temporally correspond to the peaks in the outflow rate, suggesting a galactic duty cycle, with a fountain cycle duration of $\Delta t_{\mathrm{cycle}} \sim 100 - 150$ Myr. The mass of gas ejected from the disc is lower with a lower corona mass, because stellar feedback injects less momentum and energy in the ISM as a consequence of the lower SFR levels in the disc. We have seen that the accretion of coronal gas helps the galaxy to maintain an almost constant cold gas mass in the disc, confirming the primary role of the corona in sustaining the star formation in the galaxy.

Furthermore, we have analyzed the metallicity distribution of the gas in the entire simulation box, a quantity particularly important for the cooling of the corona. The mixing of the gas caused by galactic fountains creates a gaseous mixture with a higher metallicity with respect to the initial one of the corona, this mixture will have a more efficient radiative cooling thanks to the presence of more heavy elements. Moreover, the gas accreted onto the disc causes a chemical evolution of this gas, diluting its metallicity. We found a correlation between the mass of the corona and the dilution of the metallicity in the disc. More massive coronae accrete more metal-poor mass and faster onto the disc,

pushing its metallicity lower.

Our analysis has shown the fundamental role of the galactic corona in the evolution of Milky Way-type galaxies, allowing the star formation to continue over time and modifying the chemical evolution in the disc itself.

The investigation performed in this Thesis work can be expanded in several ways. The first aspect that can be analyzed is to explore different configuration for the corona. In our simulations we have found that the corona has an initial rapid collapse due to the excessive cooling at the center that causes large gas inflows supporting a high level of star formation. A more centrally stable corona can help to obtain a more gradual evolution for this component, strengthening our results. This results can be achieved by modifying the initial conditions of the simulations along two main lines:

- Currently the corona is set up with a null velocity, adding a rotation component to the coronal gas can help in slowing, or at least delaying its accretion onto the disc.

- In the central regions the cooling time of the corona is extremely short ($\sim 10 -$ 100 Myr). This is caused by the chosen Hernquist (1990) density profile, which has a central cusp. The efficiency of the cooling strongly depends on the density of the gas and having a less centrally-concentrated corona would decrease the accretion rate of the coronal gas. This can be achieved by exploring different corona density profiles, in particular using cored profiles such as a β model (see e.g. Moster et al. 2011).

Another line of investigation that can be pursued is to explore a larger portion of the parameter space, in particular studying those parameters that regulate both structural and kinematic properties of the galaxy and parameters regulating the intensity of radiative and supernova feedback. Both aspects might have a potentially large impact on the circulation of gas between the disc and the halo of a star-forming galaxy that needs to be investigated. For instance, the intensity of the fountain flow could depend on the gas surface density in the disc, since a higher gas surface density implies a higher surface star formation rate because of the Kennicut-Schmidt relation (Schmidt, 1959; Kennicutt Jr, 1998). This directly affects the intensity of supernova-driven outflows and the gaseous exchanges with the corona. The (disc or corona) metallicity profiles can also be varied in order to have metallicity gradients compatible with the observational constraints and to analyze their impact on the

global evolution of the galaxy. Moreover, it could be very interesting to change the total galaxy mass, which in turn influences the temperature of the corona. Indeed, more massive galaxies have hotter coronae and this might make the condensation and accretion of the coronal gas more difficult.

The type of simulations analyzed in this Thesis work represent a bridge between idealized small-scale simulations and cosmological simulations, allowing to obtain a high/intermediate resolution while still considering a realistic galactic setup. Nevertheless, the model galaxy evolves in isolation and it is not inserted in a full cosmological context. For this reason, in the future the *SMUGGLE* model will be ported from idealized simulations studying the evolution of isolated galaxies to cosmological applications. In this way, it will be possible to follow the evolution of star-forming galaxies like the Milky Way with a higher degree of physical fidelity, drawing a coherent picture of the formation and evolution of such objects.

Bibliography

Abadi, M. G., Moore, B. and Bower, R. G. (1999), 'Ram pressure stripping of spiral galaxies in clusters', *Monthly Notices of the Royal Astronomical Society* **308**(4), 947–954.

Agertz, O., Kravtsov, A. V., Leitner, S. N. and Gnedin, N. Y. (2013), 'Toward a complete accounting of energy and momentum from stellar feedback in galaxy formation simulations', *The Astrophysical Journal* **770**(1), 25.

Agertz, O., Teyssier, R. and Moore, B. (2011), 'The formation of disc galaxies in a λcdm universe', *Monthly Notices of the Royal Astronomical Society* **410**(2), 1391–1408.

Aghanim, N., Akrami, Y., Ashdown, M., Aumont, J., Baccigalupi, C., Ballardini, M., Banday, A., Barreiro, R., Bartolo, N., Basak, S. et al. (2020), 'Planck 2018 results-vi. cosmological parameters', *Astronomy & Astrophysics* **641**, A6.

Almeida, J. S., Elmegreen, B. G., Munoz-Tunón, C. and Elmegreen, D. M. (2014), 'Star formation sustained by gas accretion', *The Astronomy and Astrophysics Review* **22**(1), 71.

Anderson, M. E. and Bregman, J. N. (2010), 'Do hot halos around galaxies contain the missing baryons?', *The Astrophysical Journal* **714**(1), 320.

Anderson, M. E. and Bregman, J. N. (2011), 'Detection of a hot gaseous halo around the giant spiral galaxy ngc 1961', *The Astrophysical Journal* **737**(1), 22.

Anglés-Alcázar, D., Faucher-Giguère, C.-A., Kereš, D., Hopkins, P. F., Quataert, E. and Murray, N. (2017), 'The cosmic baryon cycle and galaxy mass assembly in the fire simulations', *Monthly Notices of the Royal Astronomical Society* **470**(4), 4698–4719.

Armillotta, L., Fraternali, F. and Marinacci, F. (2016), 'Efficiency of gas cooling and accretion at the disc–corona interface', *Monthly Notices of the Royal Astronomical Society* **462**(4), 4157–4170.

Asplund, M., Grevesse, N., Sauval, A. J. and Scott, P. (2009), 'The chemical composition of the sun', *Annual review of astronomy and astrophysics* **47**.

Bahcall, J. N. and Soneira, R. M. (1980), 'The universe at faint magnitudes. i-models for the galaxy and the predicted star counts', *The Astrophysical Journal Supplement Series* **44**, 73–110.

Bakes, E. and Tielens, A. (1994), 'The photoelectric heating mechanism for very small graphitic grains and polycyclic aromatic hydrocarbons', *The Astrophysical Journal* **427**, 822–838.

Baldry, I. K., Balogh, M. L., Bower, R., Glazebrook, K., Nichol, R. C., Bamford, S. P. and Budavari, T. (2006), 'Galaxy bimodality versus stellar mass and environment', *Monthly Notices of the Royal Astronomical Society* **373**(2), 469–483.

Balsara, D. S. (2004), 'Second-order-accurate schemes for magnetohydrodynamics with divergence-free reconstruction', *The Astrophysical Journal Supplement Series* **151**(1), 149.

Barnes, J. and Hut, P. (1986), 'A hierarchical o (n log n) force-calculation algorithm', *nature* **324**(6096), 446–449.

Barrera-Ballesteros, J., Heckman, T., Sánchez, S., Zakamska, N., Cleary, J., Zhu, G., Brinkmann, J., Drory, N. et al. (2018), 'Sdss-iv manga: What shapes the distribution of metals in galaxies? exploring the roles of the local gas fraction and escape velocity', *The Astrophysical Journal* **852**(2), 74.

Bertelli, G., Nasi, E., Girardi, L. and Marigo, P. (2009), 'Scaled solar tracks and isochrones in a large region of the z–y plane-ii. from 2.5 to 20 m stars', *Astronomy & Astrophysics* **508**(1), 355–369.

Binney, J. and Tremaine, S. (2011), *Galactic dynamics*, Princeton university press.

Birnboim, Y. and Dekel, A. (2003), 'Virial shocks in galactic haloes?', *Monthly Notices of the Royal Astronomical Society* **345**(1), 349–364.

Bode, P. and Ostriker, J. P. (2003), 'Tree particle-mesh: an adaptive, efficient, and parallel code for collisionless cosmological simulation', *The Astrophysical Journal Supplement Series* **145**(1), 1.

Bogdán, Á., Bourdin, H., Forman, W. R., Kraft, R. P., Vogelsberger, M., Hernquist, L. and Springel, V. (2017), 'Probing the hot x-ray corona around the massive spiral galaxy, ngc 6753, using deep xmm-newton observations', *The Astrophysical Journal* **850**(1), 98.

Bogdán, Á., Forman, W. R., Kraft, R. P. and Jones, C. (2013), 'Detection of a luminous hot x-ray corona around the massive spiral galaxy ngc 266', *The Astrophysical Journal* **772**(2), 98.

Bogdán, Á., Vogelsberger, M., Kraft, R. P., Hernquist, L., Gilfanov, M., Torrey, P., Churazov, E., Genel, S., Forman, W. R., Murray, S. S. et al. (2015), 'Hot gaseous coronae around spiral galaxies: probing the illustris simulation', *The Astrophysical Journal* **804**(1), 72.

Box, G. E. P. and Muller, M. E. (1958), 'A Note on the Generation of Random Normal Deviates', *The Annals of Mathematical Statistics* **29**(2), 610 – 611.

Cen, R. (1992), 'A hydrodynamic approach to cosmology-methodology', *The Astrophysical Journal Supplement Series* **78**, 341–364.

Chabrier, G. (2003), 'Galactic stellar and substellar initial mass function', *Publications of the Astronomical Society of the Pacific* **115**(809), 763.

Chiappini, C., Matteucci, F. and Romano, D. (2001), 'Abundance gradients and the formation of the milky way', *The Astrophysical Journal* **554**(2), 1044.

Cignoni, M., Degl'Innocenti, S., Moroni, P. P. and Shore, S. N. (2006), 'Recovering the star formation rate in the solar neighborhood', *Astronomy & Astrophysics* **459**(3), 783–796.

Cimatti, A., Fraternali, F. and Nipoti, C. (2019), *Introduction to Galaxy Formation and Evolution: From Primordial Gas to Present-Day Galaxies*, Cambridge University Press.

Cioffi, D. F., McKee, C. F. and Bertschinger, E. (1988), 'Dynamics of radiative supernova remnants', *The Astrophysical Journal* **334**, 252–265.

Ciotti, L. and Ostriker, J. P. (1997), 'Cooling flows and quasars: different aspects of the same phenomenon? i. concepts', *The Astrophysical Journal Letters* **487**(2), L105.

Cohen, M. and Kuhi, L. V. (1979), 'Observational studies of pre-main-sequence evolution', *The Astrophysical Journal Supplement Series* **41**, 743–843.

Coles, P. and Lucchin, F. (2003), *Cosmology: The origin and evolution of cosmic structure*, John Wiley & Sons.

Conselice, C. J., Bershady, M. A., Dickinson, M. and Papovich, C. (2003), 'A direct measurement of major galaxy mergers at z< 3', *The Astronomical Journal* **126**(3), 1183.

Courant, R., Friedrichs, K. and Lewy, H. (1967), 'On the partial difference equations of mathematical physics', *IBM journal of Research and Development* **11**(2), 215–234.

Courteau, S., de Jong, R. S. and Broeils, A. H. (1996), 'Evidence for secular evolution in late-type spirals', *The Astrophysical Journal Letters* **457**(2), L73.

Dahlen, T., Strolger, L.-G., Riess, A. G., Mobasher, B., Chary, R.-R., Conselice, C. J., Ferguson, H. C., Fruchter, A. S., Giavalisco, M., Livio, M. et al. (2004), 'High-redshift supernova rates', *The Astrophysical Journal* **613**(1), 189.

Dai, W. and Woodward, P. R. (1994), 'Extension of the piecewise parabolic method to multidimensional ideal magnetohydrodynamics', *Journal of Computational Physics* **115**(2), 485–514.

Dai, X., Anderson, M. E., Bregman, J. N. and Miller, J. M. (2012), 'Xmm-newton detects a hot gaseous halo in the fastest rotating spiral galaxy ugc 12591', *The Astrophysical Journal* **755**(2), 107.

De Jong, R. S. and Davies, R. L. (1997), 'The shapes and ages of elliptical galaxies', *Monthly Notices of the Royal Astronomical Society* **285**(1), L1–L4.

Dekel, A., Zolotov, A., Tweed, D., Cacciato, M., Ceverino, D. and Primack, J. (2013), 'Toy models for galaxy formation versus simulations', *Monthly Notices of the Royal Astronomical Society* **435**(2), 999–1019.

Duffell, P. C. and MacFadyen, A. I. (2011), 'Tess: a relativistic hydrodynamics code on a moving voronoi mesh', *The Astrophysical Journal Supplement Series* **197**(2), 15.

Eastwood, J. and Hockney, R. (1981), 'Computer simulation using particles', *New York: Mc GrawHill* .

Efstathiou, G. (1992), 'Suppressing the formation of dwarf galaxies via photoionization', *Monthly Notices of the Royal Astronomical Society* **256**(1), 43P–47P.

Faucher-Giguere, C.-A., Lidz, A., Zaldarriaga, M. and Hernquist, L. (2009), 'A new calculation of the ionizing background spectrum and the effects of he ii reionization', *The Astrophysical Journal* **703**(2), 1416.

Ferland, G., Korista, K., Verner, D., Ferguson, J., Kingdon, J. and Verner, E. (1998), 'Cloudy 90: numerical simulation of plasmas and their spectra', *Publications of the Astronomical Society of the Pacific* **110**(749), 761.

Ferriere, K. M. (2001), 'The interstellar environment of our galaxy', *Reviews of Modern Physics* **73**(4), 1031.

Field, G., Goldsmith, D. and Habing, H. (1969), 'Cosmic-ray heating of the interstellar gas', *The Astrophysical Journal* **155**, L149.

Fraternali, F. (2013), 'How can star formation be sustained?', *Proceedings of the International Astronomical Union* **9**(S298), 228–239.

Fraternali, F. (2017), Gas accretion via condensation and fountains, *in* 'Gas Accretion onto Galaxies', Springer, pp. 323–353.

Fraternali, F., Marasco, A., Armillotta, L. and Marinacci, F. (2015), 'Galactic hail: the origin of the high-velocity cloud complex c', *Monthly Notices of the Royal Astronomical Society: Letters* **447**(1), L70–L74.

Fraternali, F., van Moorsel, G., Sancisi, R. and Oosterloo, T. (2002), 'Deep hi survey of the spiral galaxy ngc 2403', *The Astronomical Journal* **123**(6), 3124.

Freeman, K. C. (1970), 'On the disks of spiral and s0 galaxies', *The Astrophysical Journal* **160**, 811.

Fukugita, M., Hogan, C. and Peebles, P. (1998), 'The cosmic baryon budget', *The Astrophysical Journal* **503**(2), 518.

Fukugita, M. and Peebles, P. (2006), 'Massive coronae of galaxies', *The Astrophysical Journal* **639**(2), 590.

Gatto, A., Fraternali, F., Read, J., Marinacci, F., Lux, H. and Walch, S. (2013), 'Unveiling the corona of the milky way via ram-pressure stripping of dwarf satellites', *Monthly Notices of the Royal Astronomical Society* **433**(4), 2749–2763.

Genel, S., Vogelsberger, M., Springel, V., Sijacki, D., Nelson, D., Snyder, G., Rodriguez-Gomez, V., Torrey, P. and Hernquist, L. (2014), 'Introducing the illustris project: the evolution of galaxy populations across cosmic time', *Monthly Notices of the Royal Astronomical Society* **445**(1), 175–200.

Gingold, R. A. and Monaghan, J. J. (1977), 'Smoothed particle hydrodynamics: theory and application to non-spherical stars', *Monthly notices of the royal astronomical society* **181**(3), 375–389.

Gnedin, N. Y. and Hollon, N. (2012), 'Cooling and heating functions of photoionized gas', *The Astrophysical Journal Supplement Series* **202**(2), 13.

Godunov, S. K. (1959), 'A difference scheme for numerical solution of discontinuous solution of hydrodynamic equations', *Math. Sbornik* **47**, 271–306.

Gómez, F. A., White, S. D., Grand, R. J., Marinacci, F., Springel, V. and Pakmor, R. (2016), 'Warps and waves in the stellar discs of the auriga cosmological simulations', *Monthly Notices of the Royal Astronomical Society* **465**(3), 3446–3460.

Grand, R. J., Gómez, F. A., Marinacci, F., Pakmor, R., Springel, V., Campbell, D. J., Frenk, C. S., Jenkins, A. and White, S. D. (2017), 'The auriga project: the properties and formation mechanisms of disc galaxies across cosmic time', *Monthly Notices of the Royal Astronomical Society* **467**(1), 179–207.

Grand, R. J., van de Voort, F., Zjupa, J., Fragkoudi, F., Gómez, F. A., Kauffmann, G., Marinacci, F., Pakmor, R., Springel, V. and White, S. D. (2019), 'Gas accretion and galactic fountain flows in the auriga cosmological simulations: angular momentum and metal redistribution', *Monthly Notices of the Royal Astronomical Society* **490**(4), 4786–4803.

Grcevich, J. and Putman, M. E. (2009), 'H i in local group dwarf galaxies and stripping by the galactic halo', *The Astrophysical Journal* **696**(1), 385.

Greggio, L. (2005), 'The rates of type ia supernovae-i. analytical formulations', *Astronomy & Astrophysics* **441**(3), 1055–1078.

Guo, F. and Oh, S. P. (2008), 'Feedback heating by cosmic rays in clusters of galaxies', *Monthly Notices of the Royal Astronomical Society* **384**(1), 251–266.

Gupta, A., Mathur, S., Krongold, Y., Nicastro, F. and Galeazzi, M. (2012), 'A huge reservoir of ionized gas around the milky way: accounting for the missing mass?', *The Astrophysical Journal Letters* **756**(1), L8.

Habing, H. (1968), 'The interstellar radiation density between 912 a and 2400 a', *Bulletin of the Astronomical Institutes of the Netherlands* **19**, 421.

Hafen, Z., Faucher-Giguere, C.-A., Anglés-Alcázar, D., Stern, J., Kereš, D., Hummels, C., Esmerian, C., Garrison-Kimmel, S., El-Badry, K., Wetzel, A. et al. (2019), 'The origins of the circumgalactic medium in the fire simulations', *Monthly Notices of the Royal Astronomical Society* **488**(1), 1248–1272.

Hausman, M. and Ostriker, J. (1978), 'Galactic cannibalism. iii-the morphological evolution of galaxies and clusters', *The Astrophysical Journal* **224**, 320–336.

Herbig, G. H. (1962), The properties and problems of t tauri stars and related objects, *in* 'Advances in Astronomy and Astrophysics', Vol. 1, Elsevier, pp. 47–103.

Hernquist, L. (1990), 'An analytical model for spherical galaxies and bulges', *The Astrophysical Journal* **356**, 359–364.

Hernquist, L. (1993), 'N-body realizations of compound galaxies', *The Astrophysical Journal Supplement Series* **86**, 389–400.

Hopkins, P. F. (2015), 'A new class of accurate, mesh-free hydrodynamic simulation methods', *Monthly Notices of the Royal Astronomical Society* **450**(1), 53–110.

Hopkins, P. F., Wetzel, A., Kereš, D., Faucher-Giguère, C.-A., Quataert, E., Boylan-Kolchin, M., Murray, N., Hayward, C. C., Garrison-Kimmel, S., Hummels, C. et al. (2018), 'Fire-2 simulations: physics versus numerics in galaxy formation', *Monthly Notices of the Royal Astronomical Society* **480**(1), 800–863.

Hubble, E. P. (1926), 'Extragalactic nebulae.', *The Astrophysical Journal* **64**.

Ikeuchi, S. and Ostriker, J. (1986), 'Evolution of the intergalactic medium-what happened during the epoch z= 3-10?', *The Astrophysical Journal* **301**, 522–543.

Jacob, S., Pakmor, R., Simpson, C. M., Springel, V. and Pfrommer, C. (2018), 'The dependence of cosmic ray-driven galactic winds on halo mass', *Monthly Notices of the Royal Astronomical Society* **475**(1), 570–584.

Janhunen, P. (2000), 'A positive conservative method for magnetohydrodynamics based on hll and roe methods', *Journal of Computational Physics* **160**(2), 649–661.

Jenkins, E. B. and Tripp, T. M. (2001), 'The distribution of thermal pressures in the interstellar medium from a survey of ci fine-structure excitation', *The Astrophysical Journal Supplement Series* **137**(2), 297.

Ji, J., Irwin, J. A., Athey, A., Bregman, J. N. and Lloyd-Davies, E. J. (2009), 'Elemental abundances in the x-ray gas of early-type galaxies with xmm-newton and chandra observations', *The Astrophysical Journal* **696**(2), 2252.

Kaaret, P., Koutroumpa, D., Kuntz, K., Jahoda, K., Bluem, J., Gulick, H., Hodges-Kluck, E., LaRocca, D., Ringuette, R. and Zajczyk, A. (2020), 'A disk-dominated and clumpy circumgalactic medium of the milky way seen in x-ray emission', *Nature Astronomy* **4**(11), 1072–1077.

Karakas, A. I. (2010), 'Updated stellar yields from asymptotic giant branch models', *Monthly Notices of the Royal Astronomical Society* **403**(3), 1413–1425.

Katz, N., Weinberg, D. H. and Hernquist, L. (1996), 'Cosmological simulations with treesph', *The Astrophysical Journal Supplement Series* **105**, 19.

Kennicutt Jr, R. C. (1998), 'The global schmidt law in star-forming galaxies', *The Astrophysical Journal* **498**(2), 541.

Kereš, D., Katz, N., Fardal, M., Davé, R. and Weinberg, D. H. (2009), 'Galaxies in a simulated λcdm universe–i. cold mode and hot cores', *Monthly Notices of the Royal Astronomical Society* **395**(1), 160–179.

Kereš, D., Katz, N., Weinberg, D. H. and Davé, R. (2005), 'How do galaxies get their gas?', *Monthly Notices of the Royal Astronomical Society* **363**(1), 2–28.

Kim, C.-G. and Ostriker, E. C. (2018), 'Numerical simulations of multiphase winds and fountains from star-forming galactic disks. i. solar neighborhood tigress model', *The Astrophysical Journal* **853**(2), 173.

Kormendy, J. and Bender, R. (1996), 'A proposed revision of the hubble sequence for elliptical galaxies', *The Astrophysical Journal Letters* **464**(2), L119.

Krumholz, M. R. and Matzner, C. D. (2009), 'The dynamics of radiation-pressure-dominated h ii regions', *The Astrophysical Journal* **703**(2), 1352.

Krumholz, M. R. and Tan, J. C. (2007), 'Slow star formation in dense gas: evidence and implications', *The Astrophysical Journal* **654**(1), 304.

Lara-López, M., Cepa, J., Bongiovanni, A., García, A. P., Ederoclite, A., Castaneda, H., Lorenzo, M. F., Pović, M. and Sánchez-Portal, M. (2010), 'A fundamental plane for field star-forming galaxies', *Astronomy & Astrophysics* **521**, L53.

Lehner, N. and Howk, J. C. (2011), 'A reservoir of ionized gas in the galactic halo to sustain star formation in the milky way', *Science* **334**(6058), 955–958.

Li, J.-T., Li, Z., Wang, Q. D., Irwin, J. A. and Rossa, J. (2008), 'Chandra observation of the edge-on spiral ngc 5775: probing the hot galactic disc/halo connection', *Monthly Notices of the Royal Astronomical Society* **390**(1), 59–70.

Li, M., Bryan, G. L. and Ostriker, J. P. (2017), 'Quantifying supernovae-driven multiphase galactic outflows', *The Astrophysical Journal* **841**(2), 101.

Li, Z., Jones, C., Forman, W. R., Kraft, R. P., Lal, D. V., Di Stefano, R., Spitler, L. R., Tang, S., Wang, Q. D., Gilfanov, M. et al. (2011), 'X-ray emission from the sombrero galaxy: a galactic-scale outflow', *The Astrophysical Journal* **730**(2), 84.

Lockman, F. J. (2002), 'Discovery of a population of hi clouds in the galactic halo', *The Astrophysical Journal Letters* **580**(1), L47.

Lopez, L. A., Krumholz, M. R., Bolatto, A. D., Prochaska, J. X. and Ramirez-Ruiz, E. (2011), 'What drives the expansion of giant h ii regions?: A study of stellar feedback in 30 doradus', *The Astrophysical Journal* **731**(2), 91.

Lucy, L. B. (1977), 'A numerical approach to the testing of the fission hypothesis', *The astronomical journal* **82**, 1013–1024.

Mac Low, M.-M. and McCray, R. (1988), 'Superbubbles in disk galaxies', *The Astrophysical Journal* **324**, 776–785.

Mannucci, F., Cresci, G., Maiolino, R., Marconi, A. and Gnerucci, A. (2010), 'A fundamental relation between mass, star formation rate and metallicity in local and high-redshift galaxies', *Monthly Notices of the Royal Astronomical Society* **408**(4), 2115–2127.

Mannucci, F., Della Valle, M. and Panagia, N. (2006), 'Two populations of progenitors for type ia supernovae?', *Monthly Notices of the Royal Astronomical Society* **370**(2), 773–783.

Maoz, D., Mannucci, F. and Brandt, T. D. (2012), 'The delay-time distribution of type ia supernovae from sloan ii', *Monthly Notices of the Royal Astronomical Society* **426**(4), 3282–3294.

Marinacci, F., Binney, J., Fraternali, F., Nipoti, C., Ciotti, L. and Londrillo, P. (2010), 'The mode of gas accretion on to star-forming galaxies', *Monthly Notices of the Royal Astronomical Society* **404**(3), 1464–1474.

Marinacci, F., Fraternali, F., Nipoti, C., Binney, J., Ciotti, L. and Londrillo, P. (2011), 'Galactic fountains and the rotation of disc-galaxy coronae', *Monthly Notices of the Royal Astronomical Society* **415**(2), 1534–1542.

Marinacci, F., Grand, R. J., Pakmor, R., Springel, V., Gómez, F. A., Frenk, C. S. and White, S. D. (2017), 'Properties of h i discs in the auriga cosmological simulations', *Monthly Notices of the Royal Astronomical Society* **466**(4), 3859–3875.

Marinacci, F., Sales, L. V., Vogelsberger, M., Torrey, P. and Springel, V. (2019), 'Simulating the interstellar medium and stellar feedback on a moving mesh: implementation and isolated galaxies', *Monthly Notices of the Royal Astronomical Society* **489**(3), 4233–4260.

Marinacci, F., Vogelsberger, M., Pakmor, R., Torrey, P., Springel, V., Hernquist, L., Nelson, D., Weinberger, R., Pillepich, A., Naiman, J. et al. (2018), 'First results from the illustristng simulations: radio haloes and magnetic fields', *Monthly Notices of the Royal Astronomical Society* **480**(4), 5113–5139.

Martizzi, D., Faucher-Giguère, C.-A. and Quataert, E. (2015), 'Supernova feedback in an inhomogeneous interstellar medium', *Monthly Notices of the Royal Astronomical Society* **450**(1), 504–522.

Martizzi, D., Fielding, D., Faucher-Giguère, C.-A. and Quataert, E. (2016), 'Supernova feedback in a local vertically stratified medium: interstellar turbulence and galactic winds', *Monthly Notices of the Royal Astronomical Society* **459**(3), 2311–2326.

Martynenko, N. (2021), 'Constraining density and metallicity of the milky way's hot gas halo from o vii spectra and ram-pressure stripping', *arXiv preprint arXiv:2105.02557* .

Matthews, L. D. and Wood, K. (2003), 'High-latitude hi in the low surface brightness galaxy ugc 7321', *The Astrophysical Journal* **593**(2), 721.

Matzner, C. D. (2002), 'On the role of massive stars in the support and destruction of giant molecular clouds', *The Astrophysical Journal* **566**(1), 302.

Miller, M. J. and Bregman, J. N. (2013), 'The structure of the milky way's hot gas halo', *The Astrophysical Journal* **770**(2), 118.

Mo, H., Mao, S. and White, S. D. (1998), 'The formation of galactic discs', *Monthly Notices of the Royal Astronomical Society* **295**(2), 319–336.

Monachesi, A., Gómez, F. A., Grand, R. J., Kauffmann, G., Marinacci, F., Pakmor, R., Springel, V. and Frenk, C. S. (2016), 'On the stellar halo metallicity profile of milky way-like galaxies in the auriga simulations', *Monthly Notices of the Royal Astronomical Society: Letters* **459**(1), L46–L50.

Monaghan, J. J. and Lattanzio, J. C. (1985), 'A refined particle method for astrophysical problems', *Astronomy and astrophysics* **149**, 135–143.

Moore, B., Katz, N., Lake, G., Dressler, A. and Oemler, A. (1996), 'Galaxy harassment and the evolution of clusters of galaxies', *nature* **379**(6566), 613–616.

Morganti, R., De Zeeuw, P., Oosterloo, T., McDermid, R., Krajnović, D., Cappellari, M., Kenn, F., Weijmans, A. and Sarzi, M. (2006), 'Neutral hydrogen in nearby elliptical and lenticular galaxies: the continuing formation of early-type galaxies', *Monthly Notices of the Royal Astronomical Society* **371**(1), 157–169.

Moster, B. P., Macciò, A. V., Somerville, R. S., Naab, T. and Cox, T. J. (2011), 'The effects of a hot gaseous halo in galaxy major mergers', *Monthly Notices of the Royal Astronomical Society* **415**(4), 3750–3770.

Munoz, D. J., Kratter, K., Springel, V. and Hernquist, L. (2014), 'Planet–disc interaction on a freely moving mesh', *Monthly Notices of the Royal Astronomical Society* **445**(4), 3475–3495.

Murray, N., Quataert, E. and Thompson, T. A. (2009), 'The disruption of giant molecular clouds by radiation pressure & the efficiency of star formation in galaxies', *The Astrophysical Journal* **709**(1), 191.

Naiman, J. P., Pillepich, A., Springel, V., Ramirez-Ruiz, E., Torrey, P., Vogelsberger, M., Pakmor, R., Nelson, D., Marinacci, F., Hernquist, L. et al. (2018), 'First results from the illustristng simulations: A tale of two elements–chemical evolution

of magnesium and europium', *Monthly Notices of the Royal Astronomical Society* **477**(1), 1206–1224.

Navarro, J. F., Frenk, C. S. and White, S. D. (1997), 'A universal density profile from hierarchical clustering', *The Astrophysical Journal* **490**(2), 493.

Nelson, D., Pillepich, A., Springel, V., Weinberger, R., Hernquist, L., Pakmor, R., Genel, S., Torrey, P., Vogelsberger, M., Kauffmann, G. et al. (2018), 'First results from the illustristng simulations: the galaxy colour bimodality', *Monthly Notices of the Royal Astronomical Society* **475**(1), 624–647.

Nicastro, F., Elvis, M., Fiore, F. and Mathur, S. (2005), 'Measured cosmological mass density in the whim: The solution to the 'missing baryons' problem', *Advances in Space Research* **36**(4), 721–726.

Nicastro, F., Kaastra, J., Krongold, Y., Borgani, S., Branchini, E., Cen, R., Dadina, M., Danforth, C., Elvis, M., Fiore, F. et al. (2018), 'Observations of the missing baryons in the warm–hot intergalactic medium', *Nature* **558**(7710), 406–409.

Ocvirk, P., Pichon, C. and Teyssier, R. (2008), 'Bimodal gas accretion in the horizon–marenostrum galaxy formation simulation', *Monthly Notices of the Royal Astronomical Society* **390**(4), 1326–1338.

Oosterloo, T., Fraternali, F. and Sancisi, R. (2007), 'The cold gaseous halo of ngc 891', *The Astronomical Journal* **134**(3), 1019.

Oppenheimer, B. D., Davé, R., Kereš, D., Fardal, M., Katz, N., Kollmeier, J. A. and Weinberg, D. H. (2010), 'Feedback and recycled wind accretion: assembling the z= 0 galaxy mass function', *Monthly Notices of the Royal Astronomical Society* **406**(4), 2325–2338.

Pakmor, R., Kromer, M., Taubenberger, S. and Springel, V. (2013), 'Helium-ignited violent mergers as a unified model for normal and rapidly declining type ia supernovae', *The Astrophysical Journal Letters* **770**(1), L8.

Pakmor, R., Springel, V., Bauer, A., Mocz, P., Munoz, D. J., Ohlmann, S. T., Schaal, K. and Zhu, C. (2016), 'Improving the convergence properties of the moving-mesh code arepo', *Monthly Notices of the Royal Astronomical Society* **455**(1), 1134–1143.

Papastergis, E., Cattaneo, A., Huang, S., Giovanelli, R. and Haynes, M. P. (2012), 'A direct measurement of the baryonic mass function of galaxies and implications for the galactic baryon fraction', *The Astrophysical Journal* **759**(2), 138.

Pascale, R., Bellazzini, M., Tosi, M., Annibali, F., Marinacci, F. and Nipoti, C. (2021), 'An off-centred bulge or a satellite? hydrodynamical n-body simulations of the disc galaxy ngc 5474', *Monthly Notices of the Royal Astronomical Society* **501**(2), 2091–2111.

Pawlik, A. H. and Schaye, J. (2008), 'traphic–radiative transfer for smoothed particle hydrodynamics simulations', *Monthly Notices of the Royal Astronomical Society* **389**(2), 651–677.

Peeples, M. S. and Shankar, F. (2011), 'Constraints on star formation driven galaxy winds from the mass–metallicity relation at z= 0', *Monthly Notices of the Royal Astronomical Society* **417**(4), 2962–2981.

Peng, Y.-j., Lilly, S. J., Kovač, K., Bolzonella, M., Pozzetti, L., Renzini, A., Zamorani, G., Ilbert, O., Knobel, C., Iovino, A. et al. (2010), 'Mass and environment as drivers of galaxy evolution in sdss and zcosmos and the origin of the schechter function', *The Astrophysical Journal* **721**(1), 193.

Penton, S. V., Stocke, J. T. and Shull, J. M. (2004), 'The local lyα forest. iv. space telescope imaging spectrograph g140m spectra and results on the distribution and baryon content of hi absorbers', *The Astrophysical Journal Supplement Series* **152**(1), 29.

Pillepich, A., Nelson, D., Hernquist, L., Springel, V., Pakmor, R., Torrey, P., Weinberger, R., Genel, S., Naiman, J. P., Marinacci, F. et al. (2018), 'First results from the illustristng simulations: the stellar mass content of groups and clusters of galaxies', *Monthly Notices of the Royal Astronomical Society* **475**(1), 648–675.

Portinari, L., Chiosi, C. and Bressan, A. (1998), 'Galactic chemical enrichment with new metallicity dependent stellar yields', *Astronomy and Astrophysics* **334**, 505–539.

Power, C., Navarro, J., Jenkins, A., Frenk, C., White, S. D., Springel, V., Stadel, J. and Quinn, T. (2003), 'The inner structure of λcdm haloes—i. a numerical convergence study', *Monthly Notices of the Royal Astronomical Society* **338**(1), 14–34.

Putman, M., Peek, J. and Joung, M. (2012), 'Gaseous galaxy halos', *Annual Review of Astronomy and Astrophysics* **50**, 491–529.

Rahmati, A., Pawlik, A. H., Raičević, M. and Schaye, J. (2013), 'On the evolution of the h i column density distribution in cosmological simulations', *Monthly Notices of the Royal Astronomical Society* **430**(3), 2427–2445.

Rasmussen, J., Sommer-Larsen, J., Pedersen, K., Toft, S., Benson, A., Bower, R. G. and Grove, L. F. (2009), 'Hot gas halos around disk galaxies: Confronting cosmological simulations with observations', *The Astrophysical Journal* **697**(1), 79.

Rees, M. J. and Ostriker, J. (1977), 'Cooling, dynamics and fragmentation of massive gas clouds: clues to the masses and radii of galaxies and clusters', *Monthly Notices of the Royal Astronomical Society* **179**(4), 541–559.

Richter, P., Fox, A. J., Wakker, B. P., Lehner, N., Howk, J. C., Bland-Hawthorn, J., Bekhti, N. B. and Fechner, C. (2013), 'The cos/uves absorption survey of the magellanic stream. ii. evidence for a complex enrichment history of the stream from the fairall 9 sightline', *The Astrophysical Journal* **772**(2), 111.

Rubin, V. C., Ford Jr, W. K. and Thonnard, N. (1978), 'Extended rotation curves of high-luminosity spiral galaxies. iv-systematic dynamical properties, sa through sc', *The Astrophysical Journal* **225**, L107–L111.

Rybicki, G. B. and Lightman, A. P. (1991), *Radiative processes in astrophysics*, John Wiley & Sons.

Ryu, D. and Jones, T. (1995), 'Numerical magetohydrodynamics in astrophysics: Algorithm and tests for one-dimensional flow', *The Astrophysical Journal* **442**, 228–258.

Ryu, D., Jones, T. and Frank, A. (1995), 'Numerical magnetohydrodynamics in astrophysics: Algorithm and tests for multidimensional flow', *Astrophysical Journal* **452**(2), 785–796.

Salem, M., Besla, G., Bryan, G., Putman, M., Van Der Marel, R. P. and Tonnesen, S. (2015), 'Ram pressure stripping of the large magellanic cloud's disk as a probe of the milky way's circumgalactic medium', *The Astrophysical Journal* **815**(1), 77.

Salpeter, E. E. (1955), 'The luminosity function and stellar evolution.', *The Astrophysical Journal* **121**, 161.

Sancisi, R., Fraternali, F., Oosterloo, T. and Van Der Hulst, T. (2008), 'Cold gas accretion in galaxies', *The Astronomy and Astrophysics Review* **15**(3), 189–223.

Schawinski, K., Urry, C. M., Simmons, B. D., Fortson, L., Kaviraj, S., Keel, W. C., Lintott, C. J., Masters, K. L., Nichol, R. C., Sarzi, M. et al. (2014), 'The green valley is a red herring: Galaxy zoo reveals two evolutionary pathways towards quenching of star formation in early-and late-type galaxies', *Monthly Notices of the Royal Astronomical Society* **440**(1), 889–907.

Schmidt, M. (1959), 'The rate of star formation.', *The Astrophysical Journal* **129**, 243.

Sedov, L. I. (1946), 'Propagation of strong blast waves', *Prikl. Mat. Mekh* **10**(2), 241–250.

Semenov, V. A., Kravtsov, A. V. and Gnedin, N. Y. (2017), 'The physical origin of long gas depletion times in galaxies', *The Astrophysical Journal* **845**(2), 133.

Silk, J. (1977), 'On the fragmentation of cosmic gas clouds. i-the formation of galaxies and the first generation of stars', *The Astrophysical Journal* **211**, 638–648.

Skillman, E. D., Kennicutt, R. and Hodge, P. (1989), 'Oxygen abundances in nearby dwarf irregular galaxies', *The Astrophysical Journal* **347**, 875–882.

Smith, B., Sigurdsson, S. and Abel, T. (2008), 'Metal cooling in simulations of cosmic structure formation', *Monthly Notices of the Royal Astronomical Society* **385**(3), 1443–1454.

Smith, R. J., Glover, S. C., Clark, P. C., Klessen, R. S. and Springel, V. (2014), 'Co-dark gas and molecular filaments in milky way-type galaxies', *Monthly Notices of the Royal Astronomical Society* **441**(2), 1628–1645.

Spitzer Jr, L. (1942), 'The dynamics of the interstellar medium. iii. galactic distribution.', *The Astrophysical Journal* **95**, 329.

Spitzer Jr, L. and Baade, W. (1951), 'Stellar populations and collisions of galaxies.', *The Astrophysical Journal* **113**, 413.

Springel, V. (2000), 'Modelling star formation and feedback in simulations of interacting galaxies', *Monthly Notices of the Royal Astronomical Society* **312**(4), 859–879.

Springel, V. (2005), 'The cosmological simulation code gadget-2', *Monthly notices of the royal astronomical society* **364**(4), 1105–1134.

Springel, V. (2010*a*), 'E pur si muove: Galilean-invariant cosmological hydrodynamical simulations on a moving mesh', *Monthly Notices of the Royal Astronomical Society* **401**(2), 791–851.

Springel, V. (2010*b*), 'Smoothed particle hydrodynamics in astrophysics', *Annual Review of Astronomy and Astrophysics* **48**, 391–430.

Springel, V. (2016), High performance computing and numerical modelling, *in* 'Star Formation in Galaxy Evolution: Connecting Numerical Models to Reality', Springer, pp. 251–358.

Springel, V., Di Matteo, T. and Hernquist, L. (2005), 'Modelling feedback from stars and black holes in galaxy mergers', *Monthly Notices of the Royal Astronomical Society* **361**(3), 776–794.

Springel, V. and Hernquist, L. (2003), 'Cosmological smoothed particle hydrodynamics simulations: a hybrid multiphase model for star formation', *Monthly Notices of the Royal Astronomical Society* **339**(2), 289–311.

Springel, V., Pakmor, R., Pillepich, A., Weinberger, R., Nelson, D., Hernquist, L., Vogelsberger, M., Genel, S., Torrey, P., Marinacci, F. et al. (2018), 'First results from the illustristng simulations: matter and galaxy clustering', *Monthly Notices of the Royal Astronomical Society* **475**(1), 676–698.

Springel, V., Pakmor, R., Zier, O. and Reinecke, M. (2021), 'Simulating cosmic structure formation with the gadget-4 code', *Monthly Notices of the Royal Astronomical Society* **506**(2), 2871–2949.

Springel, V. and White, S. D. (1999), 'Tidal tails in cold dark matter cosmologies', *Monthly Notices of the Royal Astronomical Society* **307**(1), 162–178.

Steigman, G. (2007), 'Primordial nucleosynthesis in the precision cosmology era', *Annu. Rev. Nucl. Part. Sci.* **57**, 463–491.

Strolger, L.-G., Riess, A. G., Dahlen, T., Livio, M., Panagia, N., Challis, P., Tonry, J. L., Filippenko, A. V., Chornock, R., Ferguson, H. et al. (2004), 'The hubble higher z supernova search: supernovae to z≈ 1.6 and constraints on type ia progenitor models', *The Astrophysical Journal* **613**(1), 200.

Suresh, J., Bird, S., Vogelsberger, M., Genel, S., Torrey, P., Sijacki, D., Springel, V. and Hernquist, L. (2015), 'The impact of galactic feedback on the circumgalactic medium', *Monthly Notices of the Royal Astronomical Society* **448**(1), 895–909.

Taylor, G. I. (1950), 'The formation of a blast wave by a very intense explosion i. theoretical discussion', *Proceedings of the Royal Society of London. Series A. Mathematical and Physical Sciences* **201**(1065), 159–174.

Thielemann, F.-K., Argast, D., Brachwitz, F., Hix, W., Höflich, P., Liebendörfer, M., Martinez-Pinedo, G., Mezzacappa, A., Panov, I. and Rauscher, T. (2003), 'Nuclear cross sections, nuclear structure and stellar nucleosynthesis', *Nuclear Physics A* **718**, 139–146.

Tielens, A., Hony, S., Van Kerckhoven, C. and Peeters, E. (1999), Interstellar and circumstellar pahs, *in* 'The Universe as seen by ISO', Vol. 427, p. 579.

Toro, E. F. (2013), *Riemann solvers and numerical methods for fluid dynamics: a practical introduction*, Springer Science & Business Media.

Toro, E. F., Spruce, M. and Speares, W. (1994), 'Restoration of the contact surface in the hll-riemann solver', *Shock waves* **4**(1), 25–34.

Tosi, M. (1988), 'The effect of metal-rich infall on galactic chemical evolution', *Astronomy and Astrophysics* **197**, 47–51.

Travaglio, C., Hillebrandt, W., Reinecke, M. and Thielemann, F.-K. (2004), 'Nucleosynthesis in multi-dimensional sn ia explosions', *Astronomy & Astrophysics* **425**(3), 1029–1040.

Tremonti, C. A., Heckman, T. M., Kauffmann, G., Brinchmann, J., Charlot, S., White, S. D., Seibert, M., Peng, E. W., Schlegel, D. J., Uomoto, A. et al. (2004), 'The origin of the mass-metallicity relation: insights from 53,000 star-forming galaxies in the sloan digital sky survey', *The Astrophysical Journal* **613**(2), 898.

Troitsky, S. (2017), 'Density and metallicity of the milky way circumgalactic gas', *Monthly Notices of the Royal Astronomical Society: Letters* **468**(1), L36–L40.

Tumlinson, J., Peeples, M. S. and Werk, J. K. (2017), 'The circumgalactic medium', *Annual Review of Astronomy and Astrophysics* **55**, 389–432.

Twarog, B. A. (1980), 'The chemical evolution of the solar neighborhood. ii-the age-metallicity relation and the history of star formation in the galactic disk', *The Astrophysical Journal* **242**, 242–259.

Valenti, E., Zoccali, M., Mucciarelli, A., Gonzalez, O., Surot, F., Minniti, D., Rejkuba, M., Pasquini, L., Fiorentino, G., Bono, G. et al. (2018), 'The central velocity dispersion of the milky way bulge', *Astronomy & Astrophysics* **616**, A83.

Van de Hulst, H., Raimond, E. and Van Woerden, H. (1957), 'Rotation and density distribution of the andromeda nebula derived from observations of the 21-cm line', *Bulletin of the Astronomical Institutes of the Netherlands* **14**, 1.

Van den Bergh, S. (1962), 'The frequency of stars with different metal abundances.', *The Astronomical Journal* **67**, 486–490.

Van Der Kruit, P. (1988), 'The three-dimensional distribution of light and mass in disks of spiral galaxies', *Astronomy and Astrophysics* **192**, 117–127.

Van Der Kruit, P. and Searle, L. (1981), 'Surface photometry of edge-on spiral galaxies. i-a model for the three-dimensional distribution of light in galactic disks.', *Astronomy and Astrophysics* **95**, 105–115.

Vandenbroucke, B. and De Rijcke, S. (2016), 'The moving mesh code shadowfax', *Astronomy and Computing* **16**, 109–130.

Vogelsberger, M., Genel, S., Sijacki, D., Torrey, P., Springel, V. and Hernquist, L. (2013), 'A model for cosmological simulations of galaxy formation physics', *Monthly Notices of the Royal Astronomical Society* **436**(4), 3031–3067.

Vogelsberger, M., Genel, S., Springel, V., Torrey, P., Sijacki, D., Xu, D., Snyder, G., Nelson, D. and Hernquist, L. (2014), 'Introducing the illustris project: simulating the coevolution of dark and visible matter in the universe', *Monthly Notices of the Royal Astronomical Society* **444**(2), 1518–1547.

Vogelsberger, M., Marinacci, F., Torrey, P. and Puchwein, E. (2020), 'Cosmological simulations of galaxy formation', *Nature Reviews Physics* **2**(1), 42–66.

Vogelsberger, M., Sijacki, D., Kereš, D., Springel, V. and Hernquist, L. (2012), 'Moving mesh cosmology: numerical techniques and global statistics', *Monthly Notices of the Royal Astronomical Society* **425**(4), 3024–3057.

Walch, S., Whitworth, A., Bisbas, T., Wünsch, R. and Hubber, D. (2012), 'Dispersal of molecular clouds by ionizing radiation', *Monthly Notices of the Royal Astronomical Society* **427**(1), 625–636.

Ward Thompson, D., André, P. and Kirk, J. (2002), 'The initial conditions of isolated star formation–v. isophot imaging and the temperature and energy balance of pre stellar cores', *Monthly Notices of the Royal Astronomical Society* **329**(2), 257–276.

Weinberger, R., Springel, V. and Pakmor, R. (2020), 'The arepo public code release', *The Astrophysical Journal Supplement Series* **248**(2), 32.

Werk, J. K., Prochaska, J. X., Tumlinson, J., Peeples, M. S., Tripp, T. M., Fox, A. J., Lehner, N., Thom, C., O'Meara, J. M., Ford, A. B. et al. (2014), 'The cos-halos survey: physical conditions and baryonic mass in the low-redshift circumgalactic medium', *The Astrophysical Journal* **792**(1), 8.

White, S. D. and Rees, M. J. (1978), 'Core condensation in heavy halos: a two-stage theory for galaxy formation and clustering', *Monthly Notices of the Royal Astronomical Society* **183**(3), 341–358.

Wiersma, R. P., Schaye, J., Theuns, T., Dalla Vecchia, C. and Tornatore, L. (2009), 'Chemical enrichment in cosmological, smoothed particle hydrodynamics simulations', *Monthly Notices of the Royal Astronomical Society* **399**(2), 574–600.

Wolfire, M. G., Hollenbach, D., McKee, C. F., Tielens, A. and Bakes, E. (1995), 'The neutral atomic phases of the interstellar medium', *The Astrophysical Journal* **443**, 152–168.

Wolfire, M. G., McKee, C. F., Hollenbach, D. and Tielens, A. (2003), 'Neutral atomic phases of the interstellar medium in the galaxy', *The Astrophysical Journal* **587**(1), 278.

Woosley, S. E. and Weaver, T. A. (1986), 'The physics of supernova explosions', *Annual review of astronomy and astrophysics* **24**(1), 205–253.

Worthey, G., Dorman, B. and Jones, L. A. (1996), 'The g dwarf problem exists in other galaxies', *The Astronomical Journal* **112**, 948.

Yao, Y., Shull, J. M., Wang, Q. D. and Cash, W. (2012), 'Detecting the warm-hot intergalactic medium through x-ray absorption lines', *The Astrophysical Journal* **746**(2), 166.

York, D. G., Adelman, J., Anderson Jr, J. E., Anderson, S. F., Annis, J., Bahcall, N. A., Bakken, J., Barkhouser, R., Bastian, S., Berman, E. et al. (2000), 'The sloan digital sky survey: Technical summary', *The Astronomical Journal* **120**(3), 1579.

Zachary, A. L. and Colella, P. (1992), 'A higher-order godunov method for the equations of ideal magnetohydrodynamics', *Journal of Computational Physics* **99**(2), 341–347.

Ziegler, U. (2004), 'A central-constrained transport scheme for ideal magnetohydrodynamics', *Journal of Computational Physics* **196**(2), 393–416.

Zschaechner, L. K., Rand, R. J. and Walterbos, R. (2015), 'Investigating disk-halo flows and accretion: A kinematic and morphological analysis of extraplanar hi in ngc 3044 and ngc 4302', *The Astrophysical Journal* **799**(1), 61.